공학박사 학위논문

Design of bimetallic nanoparticles and its electrocatalysis for fuel oxidation

이원계 금속 나노입자의 설계
및 연료 산화에서의 전기촉매 작용

2014년 2월

서울대학교 대학원

공과대학 화학생물공학부

안 민 제

2cm
Design of bimetallic nanoparticles
and its electrocatalysis for fuel oxidation
2014
Minjeh
Ahn
2.5cm
4cm
3cm
2cm

Design of bimetallic nanoparticles and its electrocatalysis for fuel oxidation

지도 교수 성 영 은

이 논문을 공학박사 학위논문으로 제출함
2014년 1월

서울대학교 대학원
공과대학 화학생물공학부
안 민 제

안민제의 박사 학위논문을 인준함
2013년 12월

위 원 장 _____ (인)

부위원장 _____ (인)

위 원 _____ (인)

위 원 _____ (인)

위 원 _____ (인)

Abstract

Design of bimetallic nanoparticles and its electrocatalysis for fuel oxidation

Minjeh Ahn
School of Chemical and Biological Engineering
The Graduate School
Seoul National University

This study purposes the synthesis of nano-sized bimetallic electrocatalysts toward fuel oxidation reaction with the lower price and the enhanced activity compared to the existing catalysts. Moreover, a facile and rapid synthesis is introduced via a microwave-assisted synthesis instead of the conventional methods, and the complete oxidation reaction of fuel can be further achieved to improve the efficiency. The electrochemical and morphological properties of carbon supported platinum and tin oxide nanoparticles were evaluated in the first part, and the heterogeneous rhodium-tin alloyed nanoparticles deposited on the carbon as an electrocatalyst for the fuel oxidation were prepared to further reach to the complete oxidation reaction into the carbon dioxide as well as the better electrocatalytic activity and durability for fuel oxidation.

The electrocatalyst of carbon supported platinum and tin oxide nanoparticle was prepared through the microwave-assisted synthesis. It is clearly observed that the platinum nanoparticles and tin dioxide nanoparticles were uniformly dispersed onto the supporting material. The catalyst containing 16 wt% of tin oxide nanoparticles exhibited the highest activity and durability for the ethanol oxidation. The onset potentials of prepared electrocatalysts were negatively shifted compared to that of the commercial catalyst, result from the adsorbed CO species on platinum are more easily oxidized at lower potentials by hydroxyl groups adsorbed onto the surface of nearby tin oxide. In addition to the bifunctional effect, it is confirmed that the electronic effect was also acted in the platinum-tin oxide nanocomposites. As the amounts of tin oxide increased, the white line of Pt L_3-edge decreased. According to the cyclic voltammetry results and theoretical calculations, the excess amounts of tin oxide nanoparticles dispersed on the carbon surface play a role as an isolating barrier that hinders the electron transfer between platinum and carbon support, while too low amounts of tin oxide nanoparticles limit the transfer of adsorbed hydroxyl groups for the oxidation of carbon monoxide species.

Without platinum as one of the most valuable metal, the rhodium-tin alloy nanoparticle was formed for the efficient electrocatalyst toward fuel oxidation. The alloyed bimetallic nanoparticles were uniformly distributed onto the whole surface of carbon supporting material through the microwave-assisted method. Electrocatalytic activity and the ratios of peak current density at

forward scan and backward scan were significantly enhanced in the tin-abundant sample. Moreover, the rhodium-tin electrocatalysts produced much carbon dioxide compared to the platinum-based conventional catalyst, result from the accomplishment of additional total oxidation of ethanol including the C-C bond splitting. Not only the increased production of carbon dioxide but also the negative shift in onset potentials was observed. As the tin ratios were increased, the white lines of Rh K-edge were up-shifted that the interactions between rhodium and adsorbed species become stronger than the pure metallic rhodium. It indicates the electronic modifications can be powerful strategy to fulfill both the increased performance and the lower expense. Even in concentrated fuel solutions and at lower operating potentials, the superior activity and durability were maintained. These results correlated with the lower overpotentials and the increased reaction rates under various fuel concentrations, confirmed from the Tafel plots and Butler-Volmer equations.

Consequently, the bimetallic nanoparticles with improved electrocatalytic activity and durability toward fuel oxidation were successfully synthesized through the facile and swift method.

Keywords: fuel cell, electrocatalyst, ethanol oxidation reaction, bifunctional effect, electronic effect

Student Number: 2010-31326

Contents

List of Tables

List of Figures

Chapter 1. Introduction

1. 1. Renewable energy and fuel cells

Our world runs on energy. Energy plays a vital role in our life and economy from fueling our cars to heating our homes to power the appliances we depend on daily. However, expanding population, economic growth and changes in the scope of regulations are all transforming the energy landscape. A lot of researchers have estimated that the world's population will rise by more than 25 percent from 2010 to 2040, reaching nearly 9 billion [1]. An additional 2 billion people worldwide means rising electricity needs for homes and other buildings and increasing energy supplies to power industry and mobility. The global economy is expected to grow at an annual average rate of 2.8 percent for the same period [2]. Economic growth, and the improved living standards it enables, will require more energy. Climate change policies are a key factor in assessing the energy future, particularly in limiting the growth of greenhouse gas emissions. These policies are likely to have a direct and significant impact on the fuel choices made by individual countries, including a shift away from conventional fuels as carbon dioxide costs rise. These factors make us becoming more energy-efficient and moving to less carbon-intensive fuels.

In many parts of the world, concerns about security of energy supplies and

the environmental consequences have spurred government policies that support a projected increase in renewable energy sources. As a result, renewable energy sources are the fastest growing sources of electricity generation at 2.8% per year from 2010 to 2040 [1]. After renewable generation, natural gas and nuclear power are the next fastest growing sources of generation, each increasing by 2.5% per year. Almost 80% of the projected increase in renewable electricity generation is fueled by hydropower and wind power. The contribution of wind energy, in particular, has grown rapidly over the past decade, and a trend continues into the future. Most of the growth in hydroelectric generation (82%) occurs in the non-OECD countries, and more than half of the growth in wind generation (52%) occurs in the OECD countries. However, high construction costs can make the total cost of building and operating renewable generators higher than those for conventional plants. The intermittence of wind and solar energy from regional and climatic factors, in particular, can further hinder the economic competitiveness of those resources. Since concerns about energy security and greenhouse gas emissions, electricity generation from nuclear power is supported worldwide. But after the Fukushima disaster in March 2011, those projects were planned retirements of nuclear capacity in Germany and Switzerland under current policies.

Fuel cells, which convert diverse fuels directly into electricity without combustion, are key elements of a broad portfolio for building a competitive, secure, and sustainable clean energy economy [3]. Reducing greenhouse gas

emissions and eliminating dependence on imported fuel will require the use of diverse domestic energy sources and advanced fuels in all sectors of the economy (Figure 1.1, reprinted from ref. 3). Fuel cells offer a broad range of benefits for the environment, for our nation's energy security, and for our domestic economy, including: reduced greenhouse gas emissions; reduced oil consumption; expanded use of renewable power; highly efficient energy conversion; fuel flexibility (use of diverse, domestic fuels, including clean and renewable fuels); reduced air pollution; and highly reliable grid-support. These also have numerous advantages that make them appealing for end-users, including: quiet operation, low maintenance needs, less space requirement, and high reliability. In addition to using hydrogen, fuel cells can provide power from a variety of other fuels, including natural gas and renewable fuels such as alcohols or biogas.

Moreover, fuel cells can provide these benefits and address critical challenges in all energy sectors - commercial, residential, industrial, and transportation - through their use in diverse applications, including: distributed energy and combined-heat-and-power systems; backup power systems; systems for storing and transmitting renewable energy; portable power; auxiliary power for trucks, aircraft, rail, and ships; and passenger and freight vehicles. Widespread use of fuel cells would play a substantial role in overcoming our nation's key energy challenges, as demonstrated in figure 1.2 (reprinted from ref. 3), including significant reductions in greenhouse gas emissions and oil consumption as well as improvements in air quality.

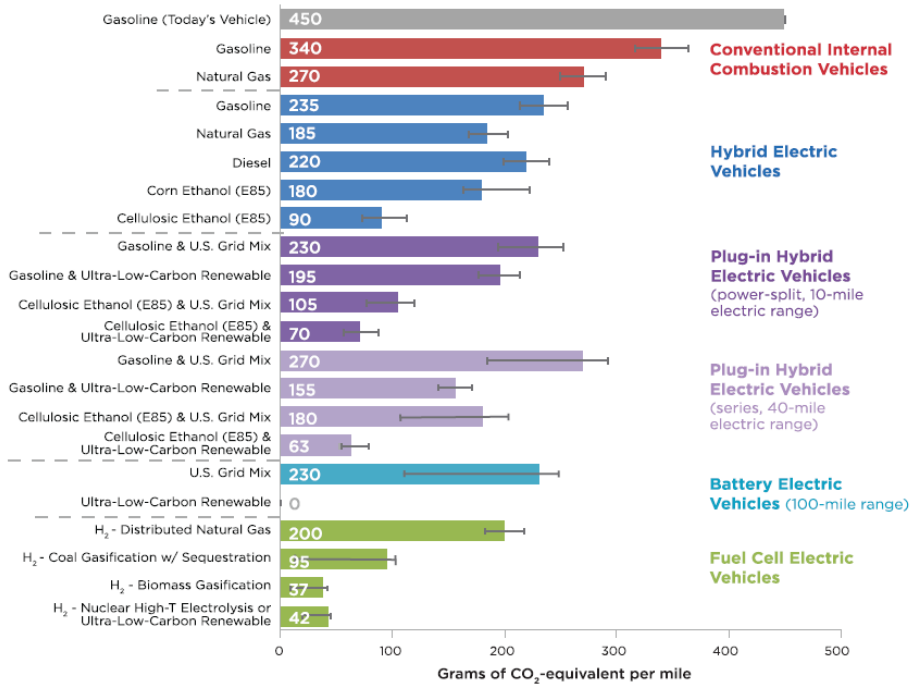

Figure 1.1. Well-to-wheels analysis of greenhouse gas emissions

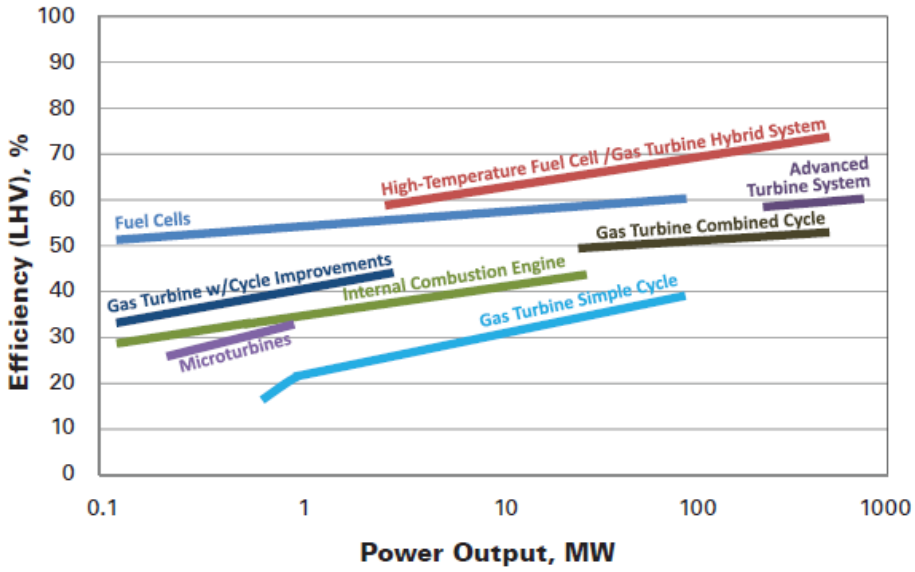

Figure 1.2. Power vs. efficiency for stationary power technologies

1. 2. Fuel cell fundamentals

Classification of fuel cells is summarized in Table 1.1, according to the types of electrolyte where the charge carriers move between the anode and the cathode. An electrolyte determines charge carriers and optimal temperature ranges for operating conditions. Various catalysts and fuels can be utilized under high temperature conditions due to the suppressed activation energy of reactants and increased stability towards carbon monoxide species as hinderers of active sites. However, the practical difficulty for applications in transportation or portable devices and expensive maintenance costs cause severe problems as well as the accelerated degradation and agglomeration of materials in technical views. In that regard, low temperature fuel cell has received much attention over the few decades for transportation, vehicles and portable devices.

As shown in figure 1.3, low temperature fuel cells, with either hydrogen (polymer electrolyte membrane fuel cell, PEMFC), methanol (direct methanol fuel cell, DMFC), ethanol (direct ethanol fuel cell, DEFC), formic acid (direct formic acid fuel cell) as the fuel, represent an environmentally friendly technology with a high efficiency as a means of producing electricity by direct electrochemical conversion of hydrogen/liquid fuel and oxygen into water and carbon dioxide. In case of hydrogen as a fuel, only pure water is produced at cathode from the electrochemical reactions, hydrogen oxidation at anode and oxygen reduction at cathode, respectively. Unfortunately, hydrogen

production, storage, and transportation are the major challenges in addition to cost, reliability and durability issues at current technological stage.

Compared to hydrogen, methanol, and formic acid, thus, ethanol becomes an attractive fuel, because it is easy to store and transport due to its relatively higher boiling point, and has less toxicity and higher energy density than other alcohols (7 kWh L^{-1} for ethanol, 4.69 kWh L^{-1} for methanol and 2.1 kWh L^{-1} for formic acid) [4]. Furthermore, ethanol has been qualified as an enormous energy source since it can be obtained in large quantities from sugar- and cellulose containing raw materials, such as sugar cane, potato, corn, wood, grasses, and the inedible parts of plants. Especially, cellulosic ethanol (from inedible plants) could allow as fuels to play an important role in the future than now expectations [5].

In terms of the use of ethanol as a fuel of fuel cell, typical cell potential vs. current density plots would be obtained as seen in figure 1.4 (reprinted from ref. 5). The open circuit potential (E_{oc}) should have the same value as the reversible cell potential theoretically, however, even when no current is drawn from a fuel cell, there is irreversible voltage loss, which means that the actual value of the open circuit potential is always lower than the theoretically expected values. It's difficult to interpret clearly, but widely understand that the mixed potentials caused by fuel crossover and internal short occurs lower open circuit potential. And during the operation of a fuel cell, the potential of single cell decays as current density increase by the overpotential (η) at the anode, cathode, and electrolyte. Thus the potential can be expressed by the

following equation:

$$E_{oc} = E_{theo} - \eta_{act} - \eta_{ohmic} - \eta_{mass} - \eta_{mix}$$

where E_{theo} is the theoretically thermodynamic reversible potential, η_{act} means the activation overpotentials at the anode and cathode, η_{ohmic} indicates the ohmic overpotentials in the electrolyte, η_{mass} caused from the mass-transport and concentration profiles at the anode and cathode, and η_{mix} is mixed potentials, respectively.

On closed circuit, the polarization can be sorted into three distinctive regions: activation overpotential region, ohmic overpotential region, and mass transport overpotential region. The causes of potential drop in the polarization curve for direct ethanol fuel cell can be understood as below.

(a) Activation overpotential: The activation overpotential is dictated by ethanol oxidation kinetics at the anode as well as oxygen reduction kinetics at the cathode. These are caused by the slowness of the reactions taking place on the surface of the catalyst. This loss is significantly considered at initial stage as shown by a suddenly drop of polarization curve.

(b) Ohmic loss: The slope where cell voltage decreases nearly linearly in the polarization curve is recognized as the ohmic overpotential region. This results from the resistance to the flow of electrons through the electrodes including ionomer, interconnections, and in the polymer electrolyte.

(c) Mass transport loss: The mass transport overpotential region, whereby

either ethanol transport on the anode side results in a mass transport limiting current, or the oxygen supply due to depletion and cathode flooding becomes a limiting step.

(d) Mixed potential: This results from the waste of fuel crossover through the electrolyte, and tiny amounts of electron are also conducted through the electrolyte. Electrolyte should only transport the ions, however, a certain amount of fuel and electron flow can be possible due to the electro-osmotic drag force or swelled electrolyte.

In the case of direct ethanol fuel cell, the value of ohmic overpotential is very low due to the electrolyte is usually well hydrated under operating conditions, and the concentration profiles can be easily enhanced through systematic control, such as increasing the flow rate and portions of reactants and improving cell designs. Although the overall performance can be diminished partially, the mixed potential can be minimized by use of thicker membrane. However, a major impediment to the commercialization of ethanol fuel cell is the difficulty in designing an effective electrocatalyst, because the kinetic rates of ethanol oxidation and oxygen reduction at the catalyst are very slow reactions, particularly, the more sluggish ethanol oxidation.

Table 1.1. Classification of various fuel cell types

	PEFC	**AFC**	**PAFC**	**MCFC**	**SOFC**
Electrolyte	Hydrated polymeric ion exchange membranes	Mobilized or immobilized potassium hydroxide	Immobilized liquid phosphoric acid	Immobilized liquid molten carbonate	Perovskites (Ceramics)
Charge carriers	H^+	OH^-	H^+	CO_3^{2-}	O^{2-}
Operating temperature	20–80℃	40-220℃	100-205℃	600-800℃	400-1000℃
Electrode	Platinum	Transition metals	Platinum	Nickel (nickel oxide)	Perovskite (perovskite-metal cermet)
External reformer for hydrocarbon fuels	Yes	Yes	Yes	No, for some fuels	No, for some fuels and cell designs
External shift conversion of CO to hydrogen	Yes, plus purification to remove trace CO	Yes, plus purification to remove trace CO	Yes	No	No
Prime cell components	Carbon-based	Carbon-based	Graphite-based	Stainless-based	Ceramic

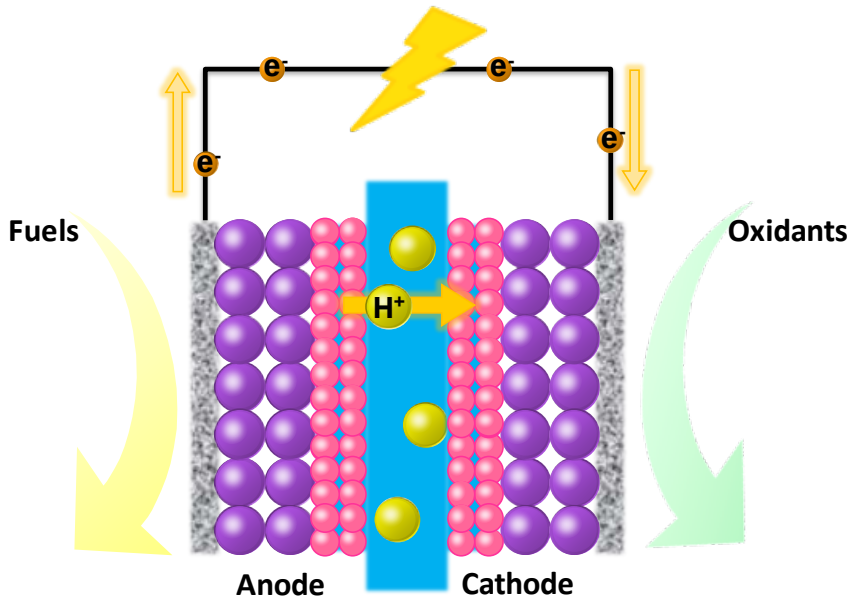

Figure 1.3. Scheme of a membrane-electrode assembly as a heart of polymer electrolyte fuel cell

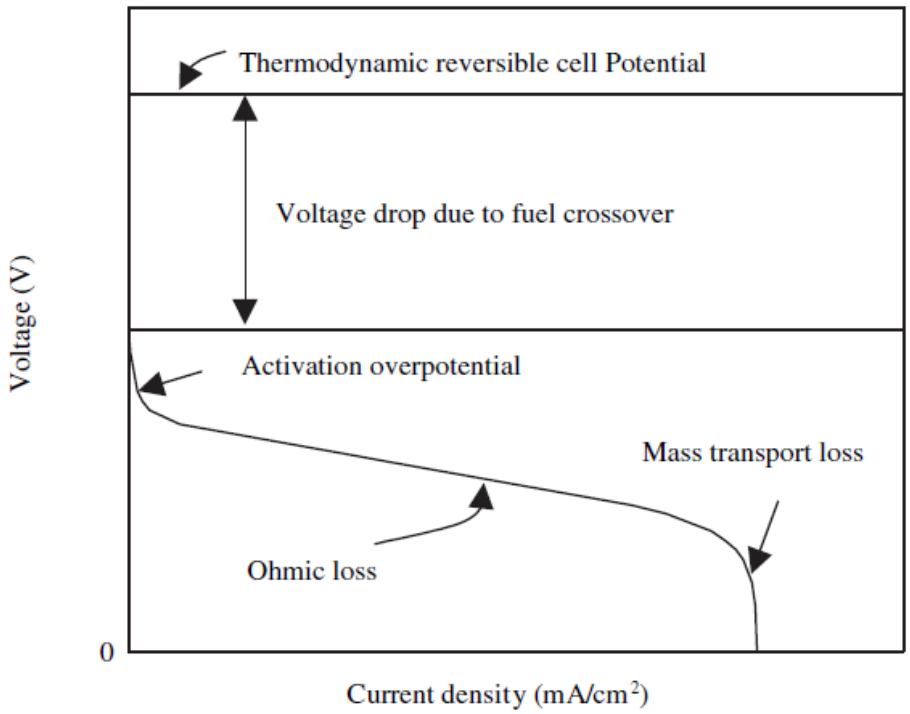

Figure 1.4. Polarization curve of direct alcohol fuel cell and four major overpotentials under fuel cell operating conditions

1. 3. Electrochemical reactions and nano-electrocatalysts

On the surface of electrocatalyst at the anode and cathode for a direct ethanol fuel cell, the half-reactions and overall reaction in acidic medium are shown as below:

Ethanol oxidation reaction (EOR) at the anode

$$C_2H_5OH + 3H_2O \rightarrow 2CO_2 + 12H^+ + 12e^- \qquad (E^0 = 0.084\ V)$$

Oxygen reduction reaction (ORR) at the cathode

$$3O_2 + 12H^+ + 12e^- \rightarrow 6H_2O \qquad (E^0 = 1.229\ V)$$

Complete overall reaction in direct ethanol fuel cell

$$C_2H_5OH + 3O_2 \rightarrow 3H_2O + 2CO_2 \qquad (E^0 = 1.145\ V)$$

The oxidation of ethanol at the anode occurs to form carbon dioxide. Water is consumed at the anode and is produced at the cathode. Protons are generated at anode, are transported across the proton exchange membrane from the anode to cathode where they react with oxygen to produce water. Electrons are transported through an external circuit from anode to cathode, providing power to connected devices as previously illustrated in figure 1.3.

A lot of researchers have been reported on the electrocatalyst for ethanol oxidation, but some problems still remain. Platinum is well-known as the most reactive catalyst which had the highest exchange current density among pure metallic compounds [7], however, its expensive cost causes a major

impediment to the commercialization of fuel cell. In addition to the economical issues, more severe problem of platinum for alcohol oxidation is the carbon monoxide (CO) poisoning.

Oxidation of ethanol involves several steps, including dehydrogenation of ethanol followed by rearrangement of the chemisorbed intermedidates, chemisorption of active oxygen species on the alloying element and the surface reaction between adsorbed CO and an adsorbed oxygen-containing species forming CO_2. During the ethanol oxidation reaction, various intermediates are formed that are adsorbed on the surface of catalyst. Some of these reaction intermediates have been found to block the active sites and inhibit further reaction. Especially, the strong adsorption of CO species produced by ethanol oxidation leads to the poisoning on the platinum surfaces. Such strong binding has been explained by electron donation from the 5σ CO orbital to the metal, and back-donation as the subsequent transfer of two electrons from the d metal atomic orbitals to the antibonding $2\pi^*$ CO orbital [8], as illustrated in figure 1.5.

To eliminate adsorbed CO from the surface it is necessary to form some oxygenated species that can react with adsorbed CO producing carbon dioxide (CO_2) and thereby to release some free sites on the Pt surface. The mechanism for the oxidative removal of adsorbed CO poison from platinum anodes has been a topic of intense investigation for the past decades. The overall reaction for removing adsorbed CO is as below.

$$CO(ads) + H_2O \rightarrow CO_2 + 2H^+ + 2e^-$$

but the mechanistic details have been elusive. The thermodynamic potential lies close to 0 V versus the reversible hydrogen electrode. Some other authors considered that adsorbed CO oxidation proceeds through reaction with adsorbed hydroxyl group (OH). The oxidation of adsorbed CO on a metal (M_1) by adsorbed OH on another metal (M_2) proceeds as follows.

$$M_1\text{-}CO(ads) + M_2\text{-}OH(ads) \rightarrow M_1 + M_2 + CO_2 + H^+ + e^-$$

The hydroxyl group is formed by the dissociative adsorption of a water molecule on the platinum.

$$H_2O \rightarrow OH(ads) + H(ads)$$

The evidence that adsorbed hydroxyl group is an active species in reaction comes from the coincidence of the potential for the onset of water oxidation with the potential of CO oxidation. On pure platinum surface, the dissociative adsorption of water is very slow at normal operating potentials, that is, this reaction step is as a rate-determining step. The formation of adsorbed hydroxyl groups on platinum lies between 0.5 to 0.8 V, which is the main reason why platinum oxidizes CO in that potential region.

To make the CO oxidation at lower overpotentials, it is essential to provide

OH at lower potentials. This can be done by means of some other metal, alloyed with platinum, which can generate adsorbed hydroxyl group at lower potentials on the surface for the oxidation of adsorbed CO on adjacent Pt sites. Such catalysts are known as bi-functional catalysts [9,10]. Ruthenium (Ru) is a well-known as a second metal for alloying with Pt. The bifunctional mechanism that dissociative adsorption of water molecules induces at nearly 0.2 V on Ru surfaces with the formation of Ru-OH.

An alternative interpretation based on an electronic ligand effect has been also suggested, although the bifunctional mechanism is the most approved. The electronic effect assumes that the alloy component changes the electronic properties of Pt atoms in its vicinity [11,12]. The presence of tin (Sn) in the surface allows for the continuous oxidation of adsorbed CO through electronic effect, whereby the Sn lowers the adsorption energy of adsorbed CO on neighboring active metal such as Pt.

Combining the electronic and bifunctional theories, it is postulated that the role of the second element is to increase OH adsorption on the catalyst surface at lower potentials, and to decrease the adsorption strength of the poisoning CO residues.

These theories can be well fitted and explained on alcohol oxidation reaction, however, more and more important factor still remained in ethanol oxidation that the bonding between two carbon molecules should be broken to complete the perfect reaction, as introduced above. Ethanol has a carbon-carbon (C-C) bond requires a higher energy to split relative to a carbon-

hydrogen bond. Thus, various intermediates are produced during ethanol oxidation reaction from partial oxidation reaction, not complete reaction, due to the difficulty in C-C bond splitting, as seen in figure 1.6 (reprinted from ref.13). And the main products from complete and partial oxidation of ethanol are listed as below [14,15].

Complete reaction

$$C_2H_5OH + 3H_2O \rightarrow 2CO_2 + 12H^+ + 12e^-$$

Partial reactions

$$C_2H_5OH + H_2O \rightarrow 2CH_3COOH + 4H^+ + 4e^-$$

$$C_2H_5OH \rightarrow CH_3CHO + 2H^+ + 2e^-$$

$$C_2H_5OH + H_2O \rightarrow CH_3CH(OH)_2 + 2H^+ + 2e^-$$

These partial reactions result in poor performance and generation of undesirable by-products due to the lower electron gains than desired theoretical values calculated from complete reaction. Therfore, notable experimental and theoretical efforts to develop effective electrocatalysts with superior activity and better CO tolerance have been concentrated for ethanol oxidation reaction, for example, alloy with Pt [16-18] and incorporating oxide materials [19-21], and DFT calculations [22-24].

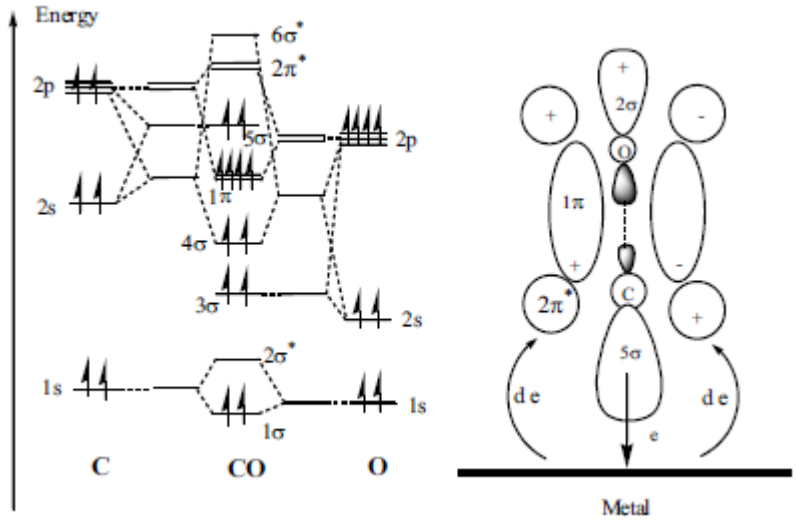

Figure 1.5. The energy levels of carbon monoxide molecules and the formation of metal – carbon monoxide bonding through electron donation and back-donation

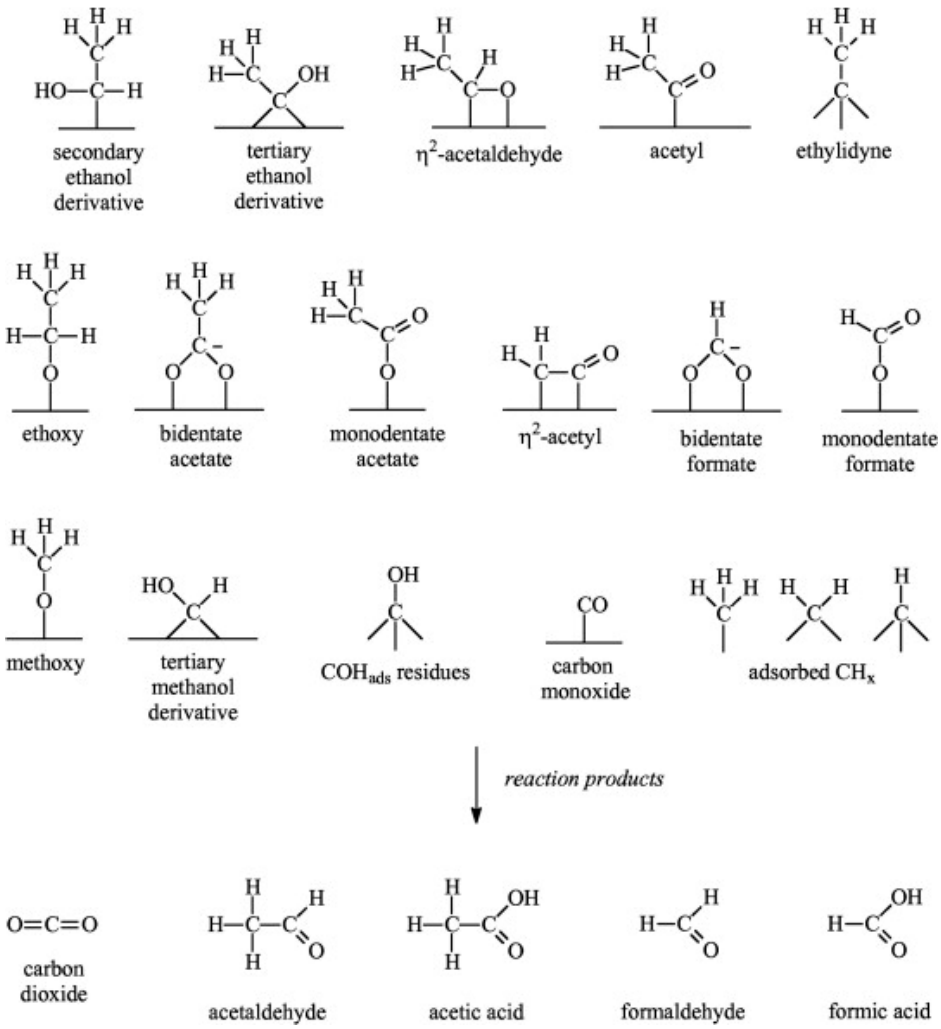

Figure 1.6. Reaction mechanism during the electro-oxidation of ethanol with various pathways to the formation of CO_2, acetaldehyde, acetic acid as end-products of the reaction

1. 4. Subject of research in the thesis

This study purposes the synthesis of nano-sized electrocatalysts toward fuel oxidation with economic advantages and improved the activity with lower overpotentials than the existing catalysts. In addition, facile and rapid synthesis is introduced via microwave-assisted synthesis compared to the conventional methods, and total oxidation reaction of fuel can be further achieved to improve the efficiency.

If the nanoparticles as an electrocatalyst are prepared by conventional method, for example, polyol reduction method, it will be taken at least 5 hours. Some other methods also need long time to synthesis from few hours to few days. However, microwave-assisted synthesis can prepare the materials within only few minutes. A microwave consists of an electric field and a magnetic field. Since only the electric field transfers energy to heat a substance, thus the energy in photon is too low to transform other molecules as shown in figure 1.7. But it provides the momentum to overcome reaction barrier and complete the reaction more quickly than conventional methods. In addition to the facile synthesis, the nanoparticles can be formed uniformly without surfactants. It is certain that the additional process should be undergone to get rid of strongly adsorbed organic molecules on the metal surface by acid treatment, irradiation under ozone, and heat treatment at higher temperature. In this studies, the electrocatalysts would be prepared uniformly and regularly without any surfactants. Some nanoparticles have been prepared by microwave synthesis

in other literatures, but few published papers were existed in case of carbon supported nanoparticles under surfactants-free conditions [25].

From a strategic point of view, the further achievement of complete ethanol oxidation reaction would be reached simultaneously. Ethanol has a carbon-carbon (C-C) bond requires a higher energy to split compared to other bonds. Thus, unwanted by-products are more produced than carbon dioxide at platinum surface during ethanol oxidation reaction. It causes lack of performance due to the lower electron gains than expected theoretical values calculated from complete reaction. Tin and rhodium is recognized to efficient for ethanol oxidation, but some different effects are revealed [26-29]. Some reports have prevailed that the tin offers the hydroxyl groups in the vicinity of active sites suffered from CO species at lower potentials, while the rhodium has the capability to split the C-C bond. From these properties of them, ternary electrocatalysts for the cooperative effect from tin and rhodium in the nearby platinum become popular for highly active toward fuel oxidation [30-32].

Thus tin oxide nanoparticles adjacent to the platinum nanoparticle will be prepared through microwave-assisted synthesis in surfactant-free environments, and discussed the correlation among the electrochemical activity, surface coverage, bifunctional effect and electronic effect. Furthermore, it will be discussed that rhodium-tin alloy have not only selectivity to carbon dioxide but also fairly good activity and durability toward ethanol oxidation.

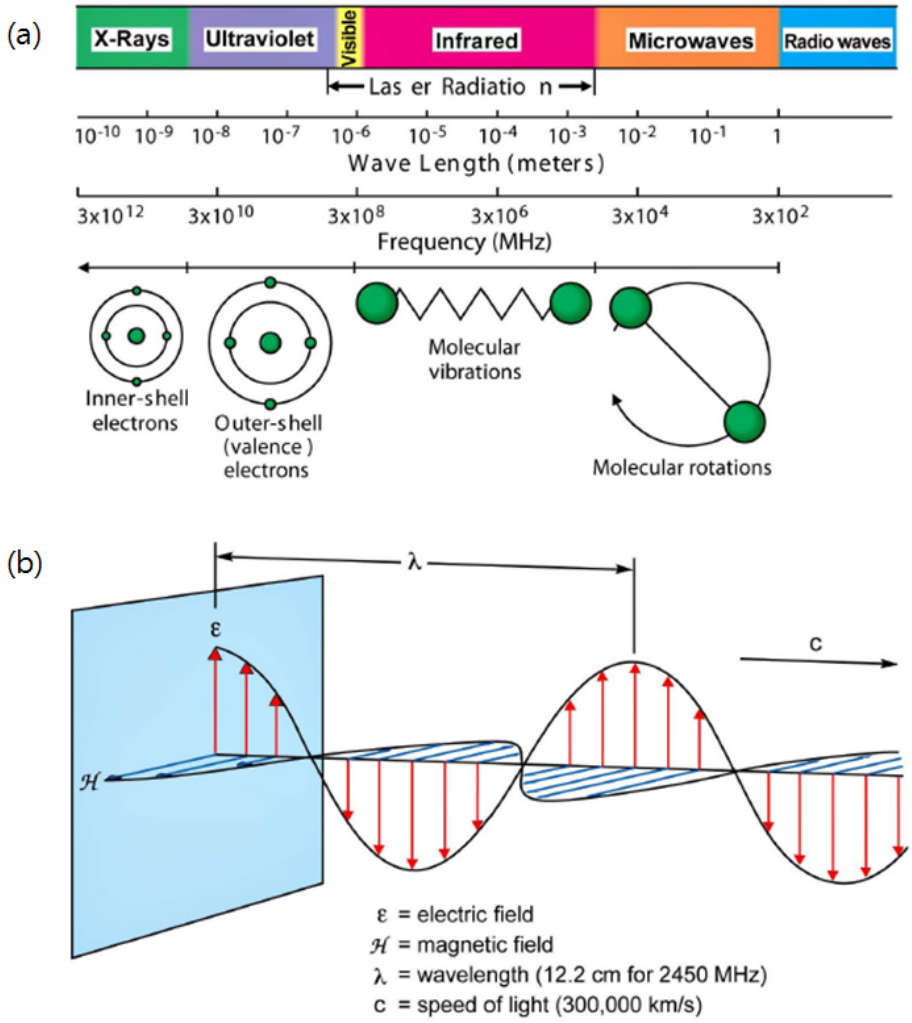

Figure 1.7. Schemes of microwave fundamental principles

1. 5. References

[1] U.S. Energy Information Administration, U.S. Department of Energy, “International energy outlook 2013 – with projections to 2040”, 1-300.

[2] ExxonMobil, “The outlook for energy 2013: A view to 2040”, 1-52.

[3] U.S Department of Energy, “An integrated strategic plan for the research, development, and demonstration of hydrogen and fuel cell technologies”, 1-73.

[4] Aicheng Chen and Peter Holt-Hindle, “Platinum-Based Nanostructured Materials: Synthesis, Properties, and Applications”, *Chem. Rev.*, **2010**, 110, 3767–3804.

[5] Oliver Inderwildi and David King, “Quo vadis biofuels?”, *Energy Environ. Sci.*, **2009**, 2, 343–346.

[6] G. Lu, and C.-Y. Wang, Two-phase micro fluidics, heat and mass transport in direct methanol fuel cells, In: B. Sunden and M. Faghri, Editor, Transport phenomena in fuel cells, WIT Press, UK, 2005.

[7] J. Larminie, and A. Dicks, Fuel cell systems explained, John Wiley & Sons, England, 2003.

[8] Branimir N. Grgur, Nenad M. Markovic, Chriss A. Lucas, and Philip N. Ross Jr., “Electrochemical oxidation of carbon monoxide: from platinum single crystals to low temperature fuel cells catalysts. Part I: Carbon monoxide oxidation onto low index platinum single crystals”, *J. Serb. Chem. Soc.*, **2001**. 66(11-12), 785-797.

[9] M. Watanabe and S. Motoo, “Electrocatalysis by ad-atoms: Part II. Enhancement of the oxidation of methanol on platinum by ruthenium ad-atoms”, *J. Electroanalytical Chem. and Interfacial Electrochem.*, **1975**, 60(3), 267-273.

[10] Kug-Seung Lee, Tae-Yeol Jeon, Sung Jong Yoo, In-Su Park, Yong-Hun Cho, Soon Hyung Kang, Kwang Hyun Choi, and Yung-Eun Sung, “Effect of PtRu alloying degree on electrocatalytic activities and stabilities”, Appl. Catal. B: Environmental, 2011, 102, 334–342.

[11] T.E. Shubina and M.T.M. Koper, “Quantum-chemical calculations of CO and OH interacting with bimetallic surfaces”, *Electrochim. Acta*, **2002**, 47, 3621-3628.

[12] P .Liu, A. Logadottir, and J.K. Norskov, “Modeling the electro-oxidation of CO and H_2/CO on Pt, Ru, PtRu and Pt_3Sn”, *Electrochim. Acta*, **2003**, 48, 3731–3742.

[13] Janaina F. Gomes, Kleber Bergamaski, Melissa F.S. Pinto, Paulo B. Miranda, "Reaction intermediates of ethanol electro-oxidation on platinum investigated by SFG spectroscopy", *J. Catal.*, **2013**, 302, 67–82.

[14] S.-C. Chang, L.-W.H. Leung, and M.J. Weaver, “Metal crystallinity effects in electrocatalysis as probed by real-time FTIR spectroscopy: Electrooxidation of formic acid, methanol, and ethanol on ordered low-index platinum surfaces”, *J. Phys. Chem.*, **1990**, 94, 6013-6021.

[15] Ermete Antolini, “Catalysts for direct ethanol fuel cells”, *J. Power Sources*, **2007**, 170, 1–12.

[16] Hyon Min Song, Dalaver H. Anjum, Rachid Sougrat, Mohamed Nejib Hedhili and Niveen M. Khashab, “Hollow Au@Pd and Au@Pt core–shell nanoparticles as electrocatalysts forethanol oxidation reactions”, *J. Mater. Chem.*, **2012**, 22, 25003-25010.

[17] Claudio Bianchini, and Pei Kang Shen, “Palladium-based electrocatalysts for alcohol oxidation in half cells and in direct alcohol fuel cells”, *Chem. Rev.*, **2009,** *109,* 4183-4206.

[18] Meng Li, David A. Cullen, Kotaro Sasaki, Nebojsa S. Marinkovic, Karren More, and Radoslav R. Adzic, “Ternary Electrocatalysts for Oxidizing Ethanol to Carbon Dioxide: Making Ir Capable of Splitting C−C Bond”, *J. Am. Chem. Soc*. **2013**, 135, 132−141.

[19] Sumanta Kumar Meher and G. Ranga Rao. “Morphology-controlled promoting activity of nanostructured MnO_2 for methanol and ethanol electrooxidation on Pt/C”, *J. Phys. Chem. C*, **2013**, 117, 4888−4900.

[20] Aidong Lan and Alexander S. Mukasyan, “Complex SrRuO3−Pt and LaRuO3−Pt catalysts for direct alcohol fuel cells”, *Ind. Eng. Chem. Res*., **2008**, 47 (23), 8989–8994.

[21] N. Acerbi, S. C. Edman Tsang, G. Jones, S. Golunski, and P. Collier, “Rationalization of interactions in precious metal/ceria catalysts using the d-band center model”, *Angew. Chem. Int. Ed*., **2013**, 52, 7737 −7741.

[22] M. Li, W.-P. Zhou, N.S. Marinkovic, K. Sasaki, and R.R. Adzic, “The role of rhodium and tin oxide in the platinum-based electrocatalysts for ethanol oxidation to CO_2”, *Electrochim. Acta*, **2013**, 104, 454-461.

[23] Y. Choi, and P. Liu, “Understanding of ethanol decomposition on Rh (111) from density functional theory and kinetic Monte Carlo simulations”, Catal. Today, 2011, 165, 64-OOO.

[24] Guofeng Cui, Shuqin Song, Pei Kang Shen, Andrzej Kowal, and Claudio Bianchini, “First-principles considerations on catalytic activity of Pd toward ethanol oxidation”, *J. Phys. Chem. C,* **2009,** *113,* 15639–15642.

[25] Elayaraja Muthuswamy, Andrew S. Iskandar, Marlene M. Amador, and Susan M. Kauzlarich, “Facile synthesis of germanium nanoparticles with size control: Microwave versus conventional heating”, *Chem. Mater.*, **2013**, 25(8), 1416–1422.

[26] Xiaodong Wang, Lena Altmann, Jörg Stöver, Volkmar Zielasek, Marcus Bäumer, Katharina Al-Shamery, Holger Borchert, Jürgen Parisi, and Joanna Kolny-Olesiak, “Pt/Sn intermetallic, core/shell and alloy nanoparticles: colloidal synthesis and structural control”, *Chem. Mater*. **2013**, 25, 1400−1407.

[27] J.C.M. Silva, R.F.B. De Souza, L.S. Parreira, E. Teixeira Neto, M.L. Calegaro, and M.C. Santos, “Ethanol oxidation reactions using SnO_2@Pt/C as an electrocatalyst”, *Appl. Catal. B: Environmental*, **2010**, 99, 265–271.

[28] Song-Hai Chai, Jane Y. Howe, Xiqing Wang, Michelle Kidder, Viviane Schwartz, Melissa L. Golden, Steven H. Overbury, Sheng Dai, and De-en Jiang, “Graphitic mesoporous carbon as a support of promoted Rh catalysts for hydrogenation of carbon monoxide to ethanol”, *Carbon*, **2012**, 50, 1574-1582.

[29] Yange Suo and I-Ming Hsing, “Highly active rhodium/carbon nanocatalysts for ethanol oxidation in alkaline medium”, *J. Power Sources*, **2011**, 196, 7945– 7950.

[30] A. Kowal, M. Li, M. Shao, K. Sasaki, M. B. Vukmirovic, J. Zhang, N. S. Marinkovic, P. Liu, A. I. Frenkel and R. R. Adzic, “Ternary Pt/Rh/SnO_2 electrocatalysts for oxidizing ethanol to CO_2”, *Nat. Mater*., **2009**, 8, 325-330.

[31] M. Li, A. Kowal, K. Sasaki, N. Marinkovic, D. Su, E. Korach, P. Liu, and R.R. Adzic, “Ethanol oxidation on the ternary Pt–Rh–SnO_2/C electrocatalysts with varied Pt:Rh:Sn ratios”, *Eletrochim. Acta*, **2010**, 55, 4331–4338.

[32] Wenxin Du, Qi Wang, Carlo A. LaScala, Lihua Zhang, Dong Su, Anatoly I. Frenkel, Virendra K. Mathura and Xiaowei Teng, “Ternary PtSnRh–SnO_2 nanoclusters: synthesis and electroactivity for ethanol oxidation fuel cell reaction”, *J. Mater. Chem*., **2011**, 21, 8887–8892.

Chapter 2. Experimental

2.1. Synthesis of nanoparticle as electrocatalysts

2.1.1. Selective deposition of platinum and tin oxide nanoparticles

Chloroplatinic acid hexahydrate ($H_2PtCl_6 \cdot 6H_2O$, > 99%), tin (IV) chloride ($SnCl_4$, 99%), benzyl alcohol (anhydrous, 99.8%), ethylene glycol (anhydrous, 99.8%), tetrahydrofuran (anhydrous, > 99%, inhibitor-free), perchloric acid (ACS regeant, 70%), 2-propanol (CHROMOSOLV Plus, for HPLC, 99.9%) and Nafion perfluorinated resin solution (5 wt% in mixture of lower aliphatic alcohols and water) were received from Sigma-Aldrich. Nitric acid (for trace analysis, 69.0%) was purchased from Fluka, and sodium hydroxide (bead, 98%) and ethanol (95.0%) were obtained from samchun chemicals. Carbon black (Vulcan XC-72) and carbon supported platinum (nominally 20% on carbon black) were purchased from Carbot corporation and Alfa Aesar (Johnson Matthey Co.), respectively. Deionized water was obtained through a Mili-Q system (millipore water, 18.2 MΩ·cm).

Carbon black was used as support of the tin oxide and platinum nanoparticles. In order to the densely functionalize the surface of carbon, the carbon nanopowder was previously oxidized by refluxing in 5.0 M nitric acid

at 80 °C for 4 h, washed with water and dried.

Deposition of the tin oxide and platinum nanoparticles was done by microwave-assisted synthesis methods as previously reported [1]. Carbon supported tin oxide composites with amounts of tin oxide ranging from 10 to 70 wt% were prepared by changing the quantities of carbon support and metal oxide precursor used in the synthesis.

First, suitable quantities of carbon and tin (IV) chloride were placed in a microwave vial containing 20 mL of benzyl alcohol, under argon. The mixture was sonicated to disperse the carbon material and then heated in a microwave (150 W) at 185 °C for 10 minutes. Then the solid was collected by centrifugation, washed with tetrahydrofuran and dried at 65 °C.

After deposition of tin oxide nanoparticles on carbon, platinum nanoparticles were then deposited onto the previously prepared materials by a microwave-assisted polyol reduction method. In all cases the amount of Pt deposited was 20 wt%. As-prepared tin oxide and carbon nanocomposite was added to a solution of chloroplatinic acid in 20 mL of ethylene glycol, under inert gas. A solution of sodium hydroxide in ethylene glycol was added to raise the pH to 11-12. The suspension was uniformly dispersed for 10 minutes and submitted to microwave irradiation for 5 minutes at 140 °C. The final solid was recovered by centrifugation, washed with ethanol and ultrapure water and dried at 65 °C.

Conventional polyol thermal reduction method was also introduced to compare with microwave-assisted synthesis. The carbon supported platinum

nanoparticles were synthesized as follows. First, the carbon black was uniformly dispersed in 250 ml of ethylene glycol under oxygen-free atmospheric conditions. Platinum precursor was added into the as-prepared solution, and then the solution was refluxed in a three-necked flask at 160 ^{o}C for 15 minutes. After stirring for several hours, the solutions were filtered with ethanol. Obtained particles were heated in a tube furnace at 140 ^{o}C for an hour in air ambient to eliminate residual organic materials.

2.1.2. Heterogeneous rhodium-tin alloy nanoparticles

Rhodium(III) chloride hydrate (> 99.9% trace metals basis), tin(II) chloride (> 99.99% trace metals basis), ethylene glycol (anhydrous, 99.8%), potassium hydroxide (45wt% solution in water), 2-propanol (CHROMOSOLV Plus, for HPLC, 99.9%) and Nafion perfluorinated resin solution (5 wt% in mixture of lower aliphatic alcohols and water) were received from Sigma-Aldrich. Ethanol (95.0%) was purchased from samchun chemicals. Carbon black (Vulcan XC-72) and carbon supported platinum (nominally 20% on carbon black) were obtained from Carbot corporation and Alfa Aesar (Johnson Matthey Co.), respectively.

Indeed, the synthesis of carbon supported rhodium-tin alloy nanoparticle was quite simple and quick via microwave-assisted methods. Furthermore, there has no surfactant that can incur the performance diminution results from inhibition of active sites by a lot of organic molecules. In addition to the

surfactant-free synthesis, no toxic materials are used during preparation of electrocatalysts.

All samples had the amounts of 20 wt% of metal with varied molar ratios of rhodium and tin. In brief, the carbon black was dispersed in 50 ml of ethylene glycol under agitation for 30 minutes, and the mixture was stirred for an hour. Adequate quantities of rhodium(III) chloride and tin(II) chloride were dissolved in 10 ml of ethylene glycol, and this mixture was added into the previously prepared ethylene glycol solution containing well dispersed carbon black under vigorous stirring. After stirring for few minutes, the suspension was submitted to microwave reactor (140 W) for 10 minutes at 170 °C in order to complete the reduction of metal precursors, followed by filtration by ethanol and drying in an oven at 75 °C. Then heat treatment of the as-prepared carbon supported rhodium-tin alloy nanoparticles was performed at 160 °C in reducing atmosphere for an hour to get rid of the unreacted metallic precursors.

2.2. Physicochemical characterization

High resolution transmission electron microscope (HR-TEM) and normal TEM were measured using JEM-2100F at an accelerating voltage of 200 kV, and JEM-2100 operated at an accelerating voltage of 120 kV, respectively. The energy of the electrons in the TEM determines the relative penetration degree of electrons, therefore, TEM with higher voltage not only offers better resolution but also allows thicker samples (less than approximately 200 nm). Cs-corrected scanning transmission electron microscope (STEM) was acquired by JEM-ARM200F (200 kV, JEOL) equipped with energy dispersive X-ray spectroscope (EDS) with a Bruker Quantax 400, and by JEM-2100F equipped with EDS made by Oxford instruments, respectively. The error associated with the determination of the platinum and tin atomic percentages by EDS was below 20 % for all the samples investigated.

Inductively coupled plasma-atomic emission spectra (ICP-AES) analysis using Shumdzu JP/ICPS-7500, elemental analysis (EA) of C, H, N through a TruSpec 630 elemental analyzer, and thermogravimetric analysis (TGA) via TA5000/SDT-Q600 (TA instruments) were carried out to confirm the quantitative information about samples, respectively. TGA measurements were conducted in the temperature range from 25 ^{o}C to 800 ^{o}C at a heating rate of 10 ^{o}C/min with 100 sccm of air flow using an alumina sample pan.

Nitrogen adsorption isotherms at -196 °C were measured on a Micromeritics Gemini. Prior to the measurements the samples were outgassed

at 150 °C overnight. The micropore volume and external surface area of the uncoated carbon were calculated by the α_s method using standard data for nitrogen adsorption on non porous carbon [2].

High-resolution X-ray diffraction (HR-XRD) spectra were obtained using Rigaku D/MAX 2500 with Cu Kα radiation (λ=0.1541 nm) at 50 kV and 200 mA. The scan range was $20° < 2\theta < 80°$ at a scan rate of 0.1° per minute.

X-ray photoelectron spectroscopy (XPS) was conducted in a surface analysis system (Thermo, Sigma Probe) by Al Kα (1486.6 eV) as an X-ray source. The constant analyzer energy mode was employed at 30 eV of pass energy with 0.1 eV steps. The obtained spectra were calibrated by C 1s peak as 284.6 eV of binding energy, and analyzed by deconvolution of the spectra using AVANTAGE software.

High-resolution X-ray photoelectron spectroscopy (HR-XPS) measurements were performed on the soft X-ray beam line connected to an undulator (U7) at the 8A1 beamline of Pohang Accelerator Laboratory. The end station was composed of a high performance electron analyzer (SCIENTA-200) with energy and angular resolution of 0.005 eV and 0.5^{o}, respectively. The experiment was carried out in an ultrahigh vacuum (UHV) chamber with a base pressure $\leq 5 \times 10^{-10}$ Torr. All spectra were measured using 630 eV of incident photon energy.

2.3. Electrochemical characterization

The electrochemical tests were performed in a standard three-electrode electrochemical cell using a glassy carbon electrode as a working electrode and platinum wire as a counter electrode. Saturated calomel electrode and Ag/AgCl electrode were used as a reference electrode in an acidic electrolyte and in an alkaline electrolyte, respectively. All measurements were performed using an AUTOLAB potentiostat manufactured by Eco Chemie. The catalyst ink slurries were prepared by mixing of catalyst powder with deionized water, 2-propanol, and 5 wt% Nafion solution as a binding material. Following mixing and ultrasonication, 5 μL of ink slurry was dropped onto the glassy carbon electrode (0.196 cm^2 geometric surface area) with a micropipette and dried in an oven at 60 °C for 15 minutes. Then dried electrode was transferred to the electrochemical cell, so the setting of working electrode was completed. All electrochemical data were recorded and reported versus reversible hydrogen electrode (RHE) to calibrate pH dependency.

Cyclic voltammograms were recorded in a liquid electrolyte at room temperature and at a scan rate of 20 mV s^{-1}. An oxygen-free 0.1 M perchloric acid solution was set as an electrolyte under acidic conditions, while an oxygen-free 0.1 M potassium hydroxide solution was used for the electrochemical test under alkaline conditions.

In terms of platinum-tin oxide composites, the catalytic activity of electrocatalyst for ethanol oxidation was evaluated by cyclic voltammetry in

argon-saturated 0.1 M perchloric acid solution containing 0.1 M ethanol. The chronoamperometric measurements were also conducted in the same solution as referred above at a constant potential of 0.5 V for 1000 seconds to estimate the long-term activity toward ethanol oxidation.

In order to assess the electrochemical stability, accelerated degradation tests (ADT) were performed in a harsh environment. The catalysts were submitted to 1000 potential cycles in argon-saturated 0.1 M perchloric acid, ranged from 0.5 V to 1.0 V at a scan rate of 100 mV s^{-1}. For comparison, the activity of commercial carbon supported platinum catalyst with 20 wt% metal contents (Johnson Matthey Co.) was also performed for the ethanol oxidation in the same conditions.

For rhodium-tin alloy nanoparticle, the ethanol oxidation reactivity of electrocatalyst was identified by cyclic voltammetry in argon-saturated 0.1 M potassium hydroxide solution containing various concentrations of ethanol. In order to check the long-term activity for ethanol oxidation, the chronoamperometric measurements were also conducted in identical solution at a constant potential of certain value for an hour. All scan rates were 20 mV s^{-1}, except Tafel plots were acquired. To clearly obtain values of ethanol oxidation on samples at lower overpotentials, the scan rate was fixed at 1 mV s^{-1} [3]. Current densities were normalized according to the loading amounts on the working electrode and active surface area of catalyst.

CO displacement was conducted in 0.1 M electrolyte with a scan rate of 20 mV s^{-1}. First, the adsorption of CO to surface of active materials via purging

high purity CO gas was achieved at a potential of 0.10 V for 10 minutes. Then the cyclic voltammograms of CO oxidation curves were acquired, after removal of residual CO gas in the electrolyte by bubbling with argon gas for 20 minutes.

2.4. *in-situ* fourier transform infrared spectroscopy

In-situ infrared spectroscopy combined with the electrochemical method is a powerful tool for understanding of the electrochemical reaction mechanisms. The electrochemical response of the ATR-FTIRS cell is usually much faster than that in the conventional cell. The ATR-FTIR measurements (Thermo Scientific) were controlled by a spectrometer with an MCT detector using unpolarized infrared radiation. The resolution of spectra, the angle of incidence, and number of scans were set as 4 cm^{-1}, 60°, and 6, respectively, and the results were collected under series collection mode to observe the spectra with applied potential for the duration. Since the submitted electrolytes were varied from acidic to alkaline environments, germanium crystal is used as an ATR prism, and the ATR-FTIR measurements were analogous to electrochemical environments. The obtained data were properly calculated through OMNIC software suite for FT-IR, NIR, and raman spectroscopy.

2.5. Synchrotron X-ray absorption spectroscopy

X-ray absorption fine structure (XAFS) experiments were performed at 7D beamline of Pohang Accelerator Laboratory (PAL, 3.0 GeV of storage ring energy, 230 mA with top-up mode) using from 4 keV to 30 keV photon energy range with bending magnet as a source. From XAFS measurements, the local structure of a specific element in materials can be examined. The main optics consists of collimating mirror, double crystal monochromator and focusing mirror. The incident beam was monochromatized using a Si(111) double crystal monochromator.

The spectra for Pt L_3-edge (E_0 = 11564 eV) and Sn K-edge (E_0 = 29200 eV) were attained in a transmission mode with separate He-filled IC Spec ionization chambers for incident and transmitted beams, respectively. In case of receiving the Pt spectra, the incident beam should be detuned by about 30% to minimize the contamination from higher harmonics, in particular, the third order reflection of the silicon crystals, while the detuning process of the incident beam for the obtaining Sn spectra was skipped. Because it is commonly known that the detuning process is not needed when the E_0 is larger than about 17000 eV. Then the energies were calibrated by Pt foil and Sn foil for obtaining Pt and Sn related spectra, respectively. The energy scan was performed in five regions for good energy resolution in a steep absorption and measurement of X-ray absorption near edge structure (XANES) and extended X-ray absorption fine structure (EXAFS) spectra at a time, for Pt, 5

eV step in region of -200 ~ -50 eV relative to E_0 with 1 seconds of integration time, 1 eV step in region of -50 ~ -20 eV with 1 seconds, 0.3 eV step in region of -20 ~ 40 eV with 1 seconds, 0.03 *k* step in region of 40 eV ~ 12.0 *k* with 2 seconds, and 0.05 *k* step in region of 12.0 *k* ~ 15.0 *k* with 2 seconds.

For the spectra of Sn, 5 eV step in region of -200 ~ -50 eV relative to E_0 with 2 seconds of integration time, 3 eV step in region of -50 ~ -20 eV with 2 seconds, 2 eV step in region of -20 ~ 40 eV with 2 seconds, 0.04 *k* step in region of 40 eV ~ 12.0 *k* with 5 seconds, and 0.06 *k* step in region of 12.0 *k* ~ 16.0 *k* with 5 seconds.

The spectra for Rh K-edge (E_0 = 23220 eV) were also obtained in a transmission mode with separate He-filled IC Spec ionization chambers for incident and transmitted beams, respectively. First, E_0 was moved to 23220 eV, and the incident beam was set to reach at the maximum values without detuning process. Energy calibration process was conducted using of Pd foil (E_0 of Pd K-edge = 24350 eV) which has the closest E_0 value to that of Rh K-edge, because the Rh foil was not existed. The E_0 was shifted to 24350 eV where the Pd K-edge appeared without controlling incident beam. After calibration was completed, the E_0 was moved back to 23220 eV again. The energy scan was performed in five regions for fine energy resolution in a steep absorption and measurement of XANES and EXAFS spectra at once, 5 eV step in region of -200 ~ -50 eV relative to E_0 with 2 seconds of integration time, 2 eV step in region of -50 ~ -20 eV with 2 seconds, 1 eV step in region of -20 ~ 40 eV with 2 seconds, 0.03 *k* step in region of 40 eV ~ 12.0 *k* with 3

seconds, and 0.05 *k* step in region of 12.0 *k* ~ 16.0 *k* with 3 seconds.

The gained results were analyzed with ATHENA and ARTEMIS in the suite of IFEFFIT software programs. Pre-edge absorption due to the background and detector were subtracted using a linear fit to the data in the range of -180 to -50 eV relative to E_0. E_0 was defined as the first inflection point on the rising absorption edge. Each spectrum was then normalized by a constant, extrapolated value to E_0 of third-order polynomial fit over absorption at 150-800 eV relative to E_0. To isolate EXAFS signal, the post-edge background function was approximated with a piecewise spline that could be adjusted so that the low-*R* component of pre-Fourier transformed data were minimized. After calculation of EXAFS function χ(k), k^3-weighted EXAFS function in momentum (*k*) space was Fourier transformed to reveal the neighboring atoms arranged according to distance from a central As atom in *R*-space. The *k* range of the transform varied between a k_{min} of 1.0 ~ 3.0 $Å^{-1}$ and a k_{max} of 12.0 ~ 12.5 $Å^{-1}$. Kaiser-Bessel function was adopted as a window function and the windowsill of *dk*=1 was also used in the transform. A shell of interest in *R*-space was back-transformed into the momentum space with Kaiser-Bessel window function and windowsill of *dR*=0.1. Fourier-filtered spectra derived from the experiments were fitted by using of the theoretical standards generated with the *ab-initio* FEFF 8.2 code [4].

2.6. References

[1] Patricia A. Russo, Minjeh Ahn, Yung-Eun Sung, and Nicola Pinna, “Improved electrocatalytic stability in ethanol oxidation by microwave-assisted selective deposition of SnO_2 and Pt onto carbon”, *RSC Adv.*, **2013**, 3, 7001-7008.

[2] P.J.M. Carrott, R.A. Roberts, and K.S.W. Sing, “Standard nitrogen adsorption data for nonporous carbons”, *Carbon*, **1987**, 25, 769-770.

[3] Wenxin Du, Kayla E. Mackenzie, Daniel F. Milano, N. Aaron Deskins, Dong Su, and Xiaowei Teng, “Palladium-tin alloyes catalysts for the ethanol oxidation reaction in an alkaline medium”, *ACS Catal*., **2012**, 2, 287-297.

[4] A. L. Ankudinov, B. Ravel, J. J. Rehr, and S. D. Conradson, "Real-space multiple-scattering calculation and interpretation of x-ray-absorption near-edge structure", *Phys. Rev. B*, **1998**, 58, 7565-7576.

Chapter 3. Results and Discussion

3.1. Selective deposition of platinum and tin oxide nanoparticles

3.1.1. Physicochemical characterization

First of all, in order to ascertain the merits of surfactant-free microwave-assisted synthesis for nanoparticle preparation, the carbon supported platinum electrocatalysts as the most interesting material for low temperature fuel cell fields were prepared through the polyol thermal reduction method and microwave method, respectively. Ethylene glycol is widely used as a solvent in polyol reduction method that enhanced controllability for particle size and dispersion of the supported metallic nanoparticles due to its homogeneous and rapid reduction of precursor, as mentioned in introduction part.

The TEM images and size distributions of carbon supported platinum catalysts prepared by ethylene glycol thermal reduction and by microwave-assisted method are shown in figure 3.1 and in figure 3.2, respectively. From counting each size of tens of platinum nanoparticle, the average particle size of platinum synthesized via thermal reduction method was about 3.29 nm and its standard deviation was 0.917. On the other hand, average particle size and standard deviation of platinum nanoparticle prepared by microwave-assisted

method are 3.26 nm and 0.472, respectively. Both samples exhibited similar particle size, but significantly smaller value was appeared in case of the microwave-assisted synthesis. It indicates that the microwave-assisted synthesis leads more uniform nanoparticle formation rather than thermal reduction method due to quick nucleation process and minimization of growth and agglomeration [1].

To prepare the carbon supported platinum-tin dioxide (Pt-SnO_2/C) nanocomposites, several amounts of tin dioxide were first deposited on the surface of the carbon black particles, by reaction of tin (IV) chloride in benzyl alcohol in the presence of the carbon and under microwave irradiation. This approach was recently reported to prepare tin dioxide/reduced graphene oxide nanocomposites in short times and with high yields [2]. It has been extended here for the coating of a common carbon support (Carbon black Vulcan XC72) used in electrocatalysis in order to synthesize catalysts for ethanol electrooxidation. Identical amounts of platinum (20 wt%) were then deposited on all the tin oxide-carbon composites.

The quantity of metal oxide and carbon black used in the synthesis, and the chemical composition and textural characteristics of the obtained materials are registered in Table 3.1. The carbon content and molar ratio of tin oxide and platinum in the composites were determined by carbon elemental analysis and EDS, respectively, and the results obtained are in close agreement with the nominal values. Since the platinum wt% is the same in all samples, the increase of the metal oxide content of the materials reflects the increase of the

SnO_2/Pt ratio. The proximity between the nominal and experimental chemical composition of the fabricated materials, reflects another advantage of the microwave heating: owing to the higher microwave absorption ability of the carbon particles compared to the solvent, the nanoparticles selectively grow on the carbon surface, in a process promoted by the surface functional groups. Therefore, the formation of free or weakly attached particles is minimized, which leads to a more precise control over the composition of the materials and higher reproducibility.

Table 3.1 also shows the apparent Brunauer–Emmett–Teller (BET) surface areas and pore volumes of the samples. BET theory purposes to explain the physical adsorption of gas molecules such as nitrogen molecules on a rough and porous solid surface and serves as the basis for an important analysis technique for the measurement of the specific surface area of a material [3]. The uncoated carbon support, i.e., the oxidized carbon black, has BET surface area of 253 m^2 g^{-1}, micropore volume of 0.045 cm^3 g^{-1} and surface area external to the micropores of 146 m^2 g^{-1}. The deposition of tin oxide and platinum nanoparticles on the carbon surface leads to a considerable decrease of the surface area and pore volume, probably caused by partial or complete blockage of the microporosity of the support. As expected, in general the surface area and pore volume decreases as the amount of tin oxide deposited on the carbon surface increases, with the samples containing the lowest amounts of metal oxide nanoparticles having similar textural characteristics.

The resolution attainable for TEM images is orders of magnitude better

than that of optic microscope since the wavelength of electrons in very smaller than that of the light. Thus the TEM can reveal the finest details of internal structure as tiny as atomic scale. In figure 3.3(a) and (b), and 3.4(a), the TEM images of the as-prepared nanocomposites clearly show an increase in the density of the particles deposited on the surface of the carbon support with the increase of the amounts of tin oxide. Moreover, the nanoparticles homogenously coat the entire surface of the carbon particles in sample Pt-SnO_2(40)/C. However, there seems to be a tendency towards the formation of nanoparticles agglomerates as the SnO_2/Pt ratio decreases, which consequently results in portions of the carbon surface being left uncoated.

A representative HRTEM image is also presented. It shows an edge of a carbon particle containing an agglomerate of metal oxide and metal nanoparticles. Figure 3.3(c) and 3.4(b) displays the power spectrum of the whole image in figure 3.3(b) and 3.4(a), respectively, showing reflections associated to the (111) and (200) lattice planes of platinum and (110) of the tin oxide cassiterite structure. Figures 3.4(c) and (d) are the power spectrums of the delimited regions in figure 3.4(a) and are due to SnO_2 and Pt nanoparticles, respectively. The particles are not oriented along a particular zone axis, but the 3.35 Å and 2.27 Å reflections of the (110) and (111) lattice planes of the cassiterite and fcc Pt structures, respectively, are clearly visible. The size of the SnO_2 and Pt nanoparticles estimated from the TEM images is approximately 4 nm in both cases.

From the study of many HRTEM images, it was found that the Pt

nanoparticles preferentially nucleate, and are therefore deposited, at the SnO_2 sites. This is attributed to the fact that the platinum-metal oxide interactions are stronger than platinum-carbon interactions [4,5]. In the case of the materials with lower SnO2/Pt ratios (Pt-SnO_2(8)/C, Pt-SnO_2(16)/C, and Pt-SnO_2(24)/C), in which the quantity of tin dioxide is not enough to cover most of the carbon surface, as it happens with Pt-SnO_2(40)/C, the higher affinity of the platinum for the metal oxide leads to the formation of small Pt-SnO2 clusters, as shown in figure 3.3. As it will be shown below, this particular type of morphology is especially favorable for the ethanol oxidation reaction.

XRD is a non-destructive and relatively swift analyzing tool in observing the structural properties of materials. X-ray application is to verify the structural quality of crystals and stems of nanoparticle from the short wavelength of X-ray compared to the interatomic spacing. Diffractions are produced from the existence of certain phase relations between two or more waves. In the case of crystalline phase material, an interaction between the incident X-ray beam and the atoms of a particular crystal plane results in constructive interference when the Bragg condition is satisfied.

$$n \lambda = 2 d \sin \theta$$

where n is the order of the diffraction, λ means the wavelength of the X-ray beam, d indicates the interatomic spacing of crystal plane, and θ is the incident angle of X-ray source. θ-2θ offers information on the crystallographic

structure such as metallic/oxide phases and lattice structures. The average crystalline size (L) of the nanoparticles can be calculated by using the Scherrer equation from the full width at half maximum (FWHM).

$$L = 0.9 \lambda_{K\alpha} / B(2\theta) \cos \theta_{max}$$

where $\lambda_{K\alpha}$ is Cu Kα beamline as the X-ray source from a X-ray generator, B(2θ) refers the FWHM in radians, and θ_{max} is the angle value of the specific crystal plane at maximum intensity.

As exhibited in figure 3.5, it shows the X-ray diffraction patterns of the composites with different tin oxide amounts. All diffractograms exhibit peaks of the cassiterite structure of SnO_2 (JCPDS file no. 41-1445) and of the face-centered cubic platinum lattice (JCPDS file no. 87-0640). Specifically, diffraction by the (111), (200) and (220) lattice planes of platinum are observed at approximately 39, 46 and 67° (2θ), while the diffraction peaks associated with the (110), (101) and (211) planes of the tin oxide structure are seen at approximately 26, 34 and 52° (2θ). The change in the SnO_2/Pt ratio of the samples is noticeable on the variation of the intensity of the corresponding reflections. As the amount of tin oxide nanoparticles increases, the corresponding diffraction peaks become progressively much intense. The average size of the tin oxide nanoparticles, estimated with the Scherrer equation from the XRD data of the Pt-SnO_2/C composites and SnO_2/C samples prior to Pt deposition, is about 5, 4, 4 and 4 nm for tin oxide amounts

of 8, 16, 24, and 40 wt%, respectively, which is in close agreement with those calculated from the TEM data. The slight decrease of the average particle size with the decrease of the SnO_2/Pt ratio can be attributed to the decrease of the amount of metal oxide precursor added to the synthesis in order to produce composites with low tin oxide weight %. On the other hand, the average size of the Pt nanoparticles estimated from the (200) reflection is ca. 3, 4, 4 and 4 nm for tin oxide amounts of 8, 16, 24, and 40 wt%, respectively. The calculated average size of the Pt nanoparticles is slightly lower for the highest SnO_2/Pt ratio, which can be explained by differences in the dispersion of the platinum nanoparticles on surfaces with distinct metal oxide coverage (the dispersion is better on the carbon with the highest amount of SnO2).

The Pt 4f and Sn 3d XPS spectra of the Pt-SnO_2(40)/C sample in figure 3.6. XPS is a surface-sensitive method because the emitted photoelectrons originate from the upper 0.5 - 5 nanometers of the sample. Thus main purpose of using XPS is to identify components using binding energy shifts due to the changes in the chemical structure and oxidation states. The binding energy of Pt $4f_{7/2}$ is 70.9 eV (Figure 3.6(a)), corresponding to platinum in the zero-valent state. The binding energy of the Sn $3d_{5/2}$ peak (487.6 eV) indicates the presence of tin oxide on the material (Figure 3.6(b)). The value is shifted to higher binding energies with respect to the binding energy corresponding to the Sn^{4+} oxidation state (486.4 eV) [6]. Shifts in the binding energies can be also attributed to interactions between the various components of the sample such as tin oxide and platinum. Even though the electrocatalysts were

submitted to the electrochemical conditions including tens of potential cycling, dipping in an acidic solution, and oxidizing atmosphere, there were no discernible peak shifts on the Pt 4f and Sn3d XPS spectra compared to that of the pristine. It means that the prepared catalysts had fairly stable oxidation state and structural properties, results in relatively regular performances will be observed in electrochemical results.

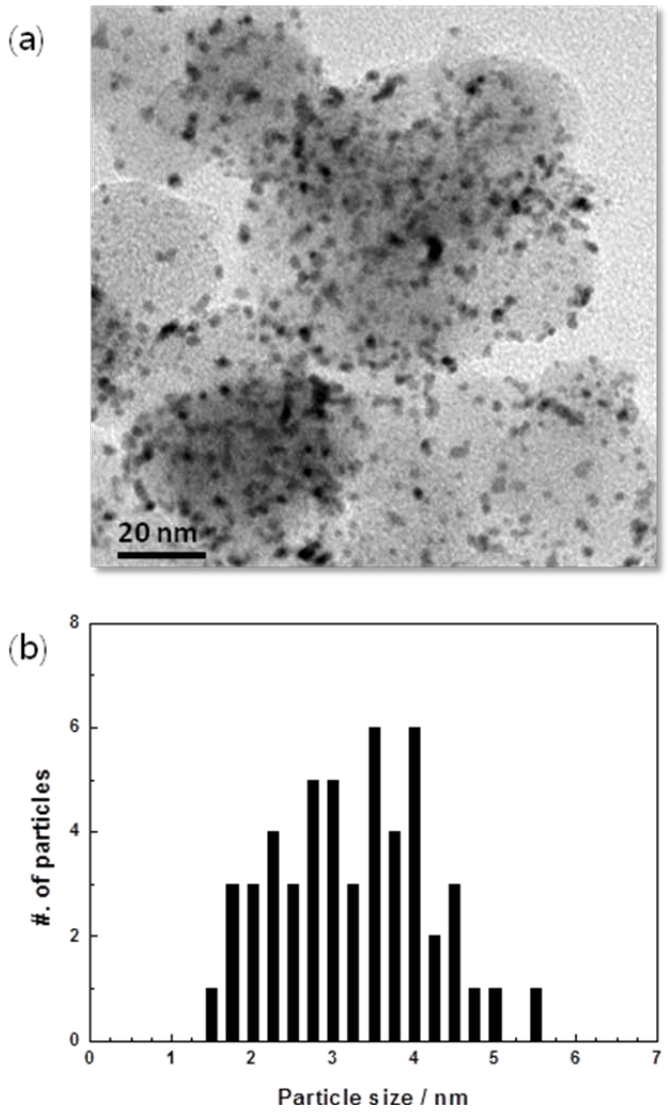

Figure 3.1. (a) TEM image and (b) platinum particle size distribution of 20wt% carbon supported platinum electrocatalyst synthesized through the polyol thermal reduction method

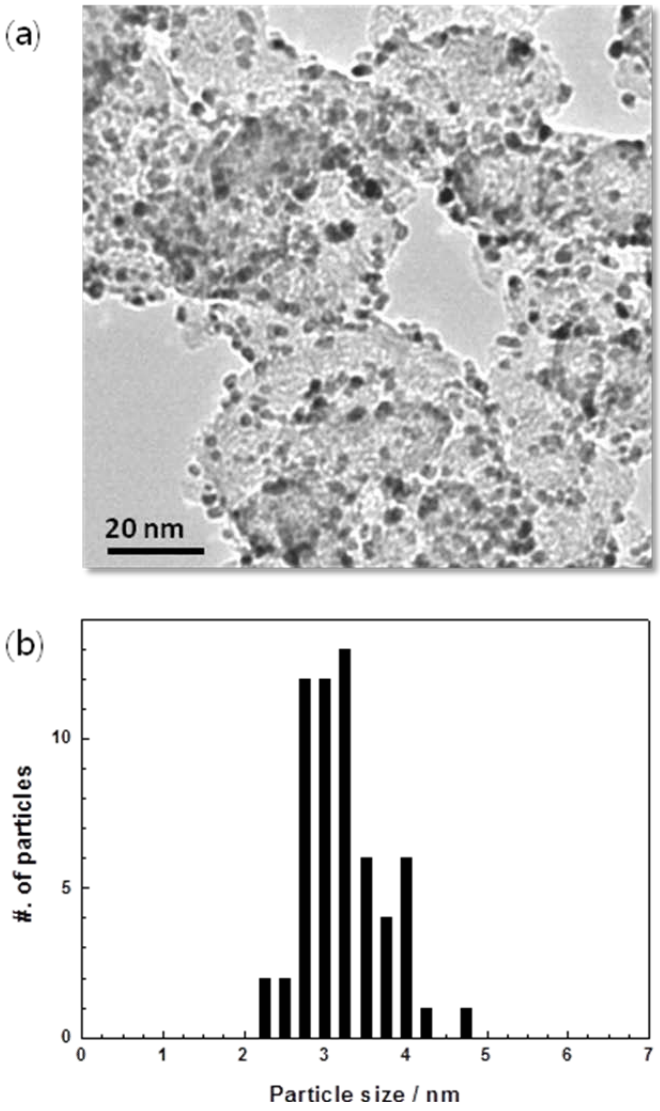

Figure 3.2. (a) TEM image and (b) platinum particle size distribution of 20wt% carbon supported platinum electrocatalyst synthesized through the microwave-assisted synthesis

Table 3.1. Quantities of metal oxide and carbon used in the synthesis, and composition and textural characteristics of the various prepared Pt-SnO_2/C catalysts

Sample	C wt % [a]	SnO_2 wt% [b]	S_{BET} / $m^2\ g^{-1}$	$V_{p(0.95)}$ / $cm^3\ g^{-1}$ [c]
Oxidized carbon	100	0	253	0.05
Pt-SnO_2(8)/C	69	8	142	0.24
Pt-SnO_2(16)/C	66	16	154	0.24
Pt-SnO_2(24)/C	56	24	134	0.18
Pt-SnO_2(40)/C	42	40	108	0.16

[a] carbon weight percentage determined by CHNS elemental analysis

[b] molar SnO_2/Pt ratio estimated by EDS

[c] pore volume obtained at p/p°=0.95

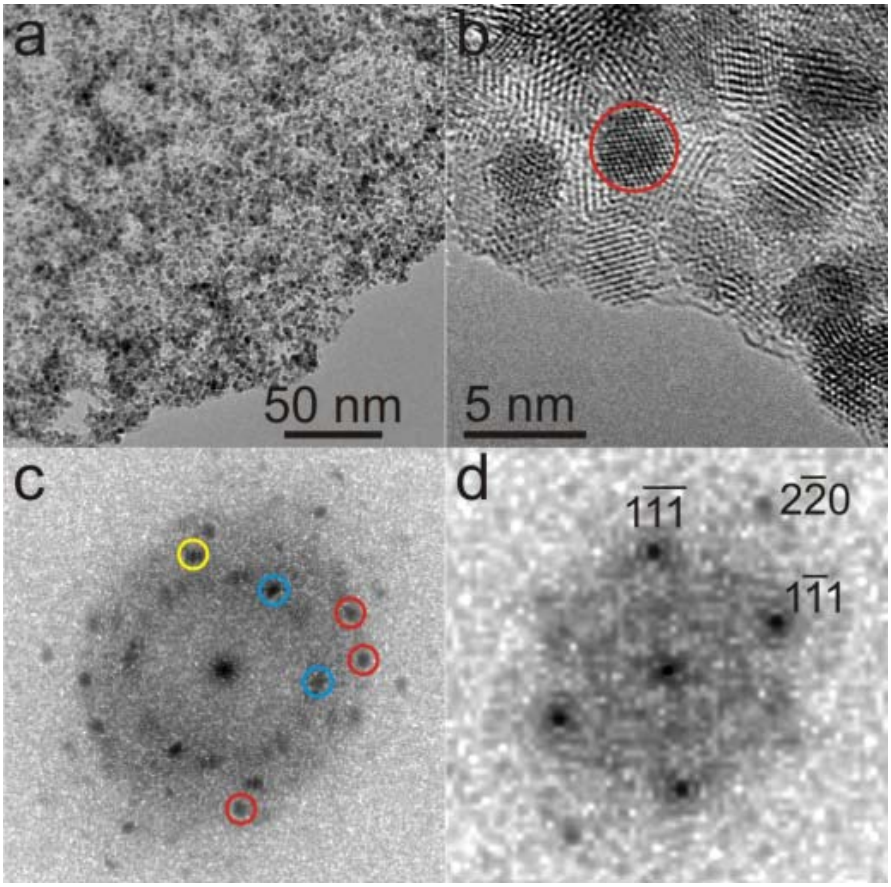

Figure 3.3. (a) TEM image and (b) high resolution TEM image of Pt-SnO_2(40)/C. Power spectra (c) of the whole image and (d) of the delimited regions.

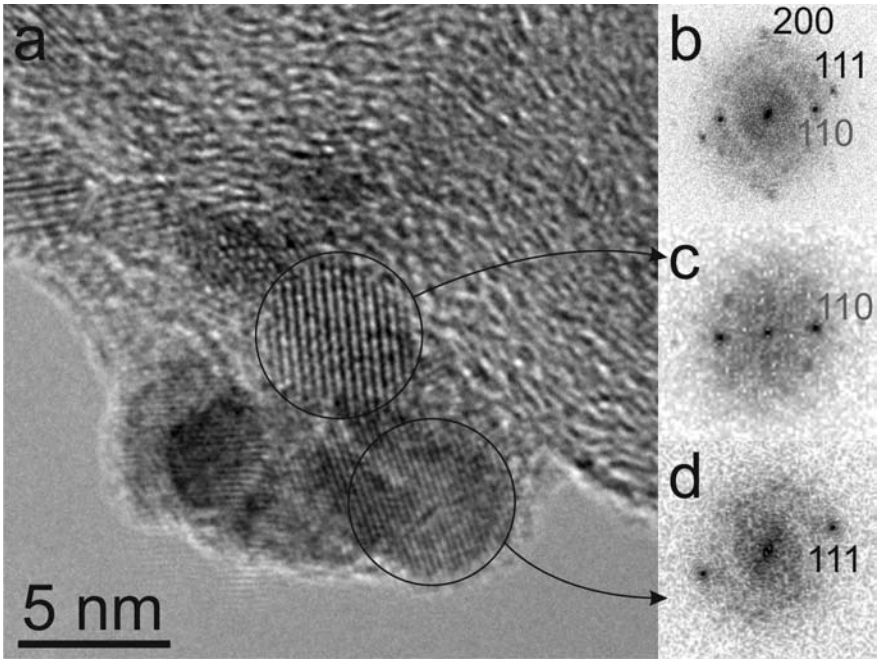

Figure 3.4. (a) High resolution TEM image of Pt-SnO_2(16)/C. Power spectra (b) of the whole image and (c, d) of the delimited regions. Indices in grey for the SnO_2 cassiterite and in black for the Pt fcc structure

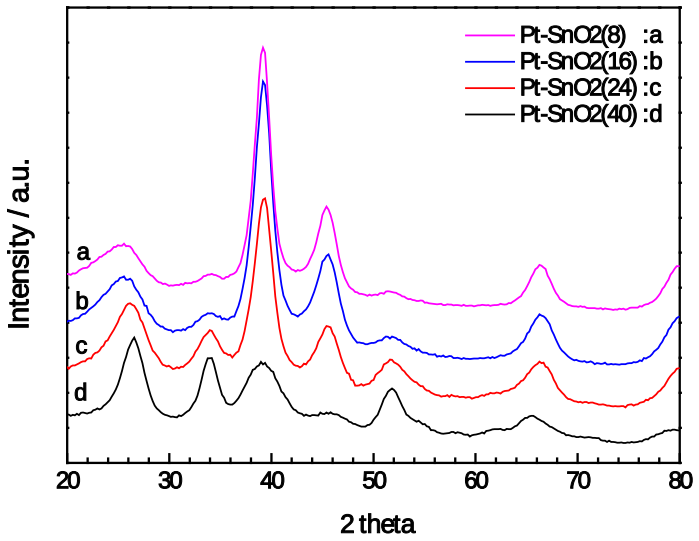

Figure 3.5. X-ray powder diffraction patterns of (a) Pt-SnO_2(8)/C, (b) Pt-SnO_2(16)/C, (c) Pt-SnO_2(24)/C and (d) Pt-SnO_2(40)/C nanocomposites

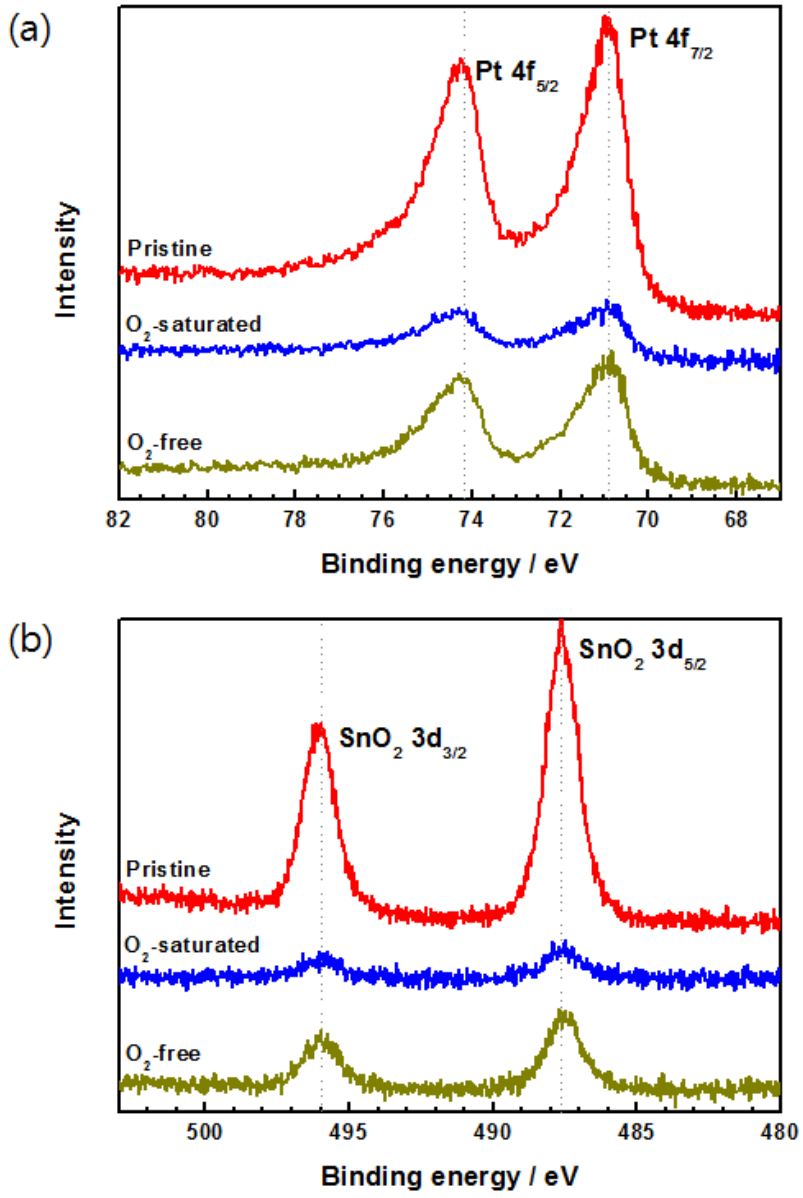

Figure 3.6. XPS results of (a) Pt 4f and (b) Sn 3d of the Pt-SnO_2(40)/C sample

3.1.2. Electrochemical characterization

The electrochemical activity of the carbon supported platinum and tin oxide nanocomposites toward the ethanol oxidation reaction was investigated by cyclic voltammetry and the results are presented in figure 3.7(a).For comparison, the voltammogram of a commercial carbon supported platinum (Johnson Matthey Co.) catalyst with 20 wt% metallic compounds is also presented. The curves show multiple oxidation peaks, similarly to results reported in the literature [7,8]. The multiple oxidation peaks are caused by intermediate species formed after the ethanol oxidation reaction, especially unstable carbon species that react rapidly on metal surfaces. Intermediate species that may be produced during ethanol oxidation include acetaldehyde, acetate or acetic acid, in addition to hydrocarbon fragments [9,10]. The presence of many unstable intermediates during the electrochemical reactions also induces current perturbations during potential cycling, which can be minimized by controlling the scan rate, but not fully eradicated.

The onset potential for the ethanol oxidation reaction is similar for all Pt-SnO_2/C nanocomposite catalysts (0.21 V), and c.a. 200 mV lower than that of the Pt/C catalyst. This means that tin oxide decreases the activation energy of the reaction, so the oxidation starts at lower potential. Moreover, the onset potential is not influenced by the quantity of tin oxide on the sample.

Additionally, the current density of the bimetallic systems at low potential (0.4 V) is in all cases higher than that of monometallic system (between 2.5

and 4.6 times higher), with the lowest increase corresponding to the material with higher amount of metal oxide nanoparticles and the maximum being observed for Pt-SnO_2(16)/C. With the exception of high loading amounts of tin oxide samples, the composites also produce higher peak currents densities than commercial catalyst as shown in figures 3.7(a). In particular, the anodic peak current density of ethanol oxidation on Pt-SnO_2(16)/C is approximately 33 % higher than that of Pt/C. Therefore, all three catalysts with lower amounts of tin oxide show better performance for the electrocatalytic oxidation of ethanol at room temperature than the commercial catalyst, with the optimal performance being achieved with 16 wt% of tin oxide in catalyst, that is, SnO_2/Pt molar ratio of 1.0.

It is worth noticing that improvement of the electrocatalytic activity of platinum by tin oxide has been reported by several other authors [11-14]. The advantage of the materials described here is the simplicity and quickness of the procedure by which they are synthesized. Moreover, the characteristics of microwave heating lead to a selective growth of the nanoparticles on the carbon surface, therefore allowing a relatively precise control over the composition of materials.

The electrochemical active surface area is an important parameter affecting the performance of the catalysts. However, the determination of active area by hydrogen desorption for materials containing metal oxides does not lead to highly exact values due to the presence of a high amount of functional groups on the metal oxide. Nevertheless, considering that (i) the size of the platinum

nanoparticles is similar in the materials with various tin oxide amounts (various molar ratio of tin oxide and platinum); (ii) the amount of platinum is the same in all the samples; and (iii) the platinum was reduced after tin dioxide deposition, the electrochemical active surface area of the samples should be similar, as also reported by other authors [14].

Chronoamperometric measurements performed at a constant potential of 0.5 V for 1000 seconds were exhibited in figure 3.7(b) and are consistent with the cyclic voltammograms reported in figure 3.7(a). The current densities of all the bimetallic nanocomposite catalysts are higher than that of commercial carbon supported platinum catalyst during the measurement time. The decay of the current density with time during ethanol oxidation on Pt-based catalysts is attributed to the poisoning of the metal active sites by reaction intermediates like CO species. The slower decrease of the current density observed for the Pt-SnO_2/C materials compared to the Pt/C catalyst reflects the promoting effect of tin oxide on CO oxidation (i.e., its anti-poisoning effect) and the consequent higher electrochemical stability and efficiency of the former catalysts.

The cyclic voltammograms and chronoamperometry results of electrocatalysts were summarized in figure 3.8. Peak current densities of forward scan and current densities under steady-state at a constant potential of 0.5 V were plotted along the weight percent of tin oxide as bars and straight lines, respectively. It indicates that the highest initial and final current densities were observed on Pt-SnO_2(16)/C sample, and similar tendencies

were shown between initial current density profiles and current density profiles at steady-state. Only the platinum was presented as an electrocatalyst, commercial Pt/C, the decay of current density during 1000 seconds was extremely large relative to the Pt-SnO_2/C nanocomposites. This result stated that the tin oxide can play an important role in alleviating the CO poisoning on Pt.

As mentioned above, the oxidation of ethanol at platinum surfaces involves a complex set of reactions and the formation of a high number of intermediate products, including CHx, CHxO or CO species, which can be further oxidized to carbon dioxide [15]. Intermediate species such as CO adsorb strongly on the surface of the Pt catalyst, poisoning it by making the active sites unavailable for further reaction. The effect of tin oxide on the electrocatalytic activity of platinum has been extensively studied and is attributed to an increase of the CO-tolerance of the metal catalyst by the metal oxide (i.e., to an anti-poisoning effect of the metal oxide), through a bi-functional mechanism [16,17] or an electronic effect [7,12], which can also occur simultaneously.

On the one hand, the increase of the CO-tolerance of Pt through the bi-functional mechanism arises from the ability of tin oxide to dissociate water molecules at lower potentials (at about 0.2 V) than platinum, forming adsorbed hydroxyl group that provide the oxygen atom required for the oxidation of CO to CO_2 at the metal surface and freeing the active sites [16,17]. Cyclic voltammetry results were attained under argon-purged 0.1 M

perchloric acid electrolyte, as seen in figure 3.9, which can offer the characteristics of material surface indirectly. According to the 6 cyclic voltammograms, similar shapes were observed on low tin oxide amounts (from 8 wt% to 24 wt%) in electrocatalysts in figure 3.9(a), (b) and (c), respectively, and figure 3.9(d) and (e) showed similar trends. Hydrogen desorption peak ranged from 0 to 0.4 V could be found in figure 3.9(a), (b) and (c), although the tin oxide also was existed. It means that the Pt-SnO_2/C nanocomposites with low tin oxide amounts act as a Pt-like behavior, that is, the surface characteristics are close to the commercial Pt/C catalyst, as displayed in figure 3.9(f). On the contrary, the cyclic voltammograms of Pt-SnO_2/C nanocomposites with high tin oxide amounts showed as an oxide-like shape as seen in figure 3.9(d) and (e).

From the quantitative and qualitative methods such as elemental analysis, ICP-AES results, TEM images and XRD results, the particle size of carbon, tin oxide and platinum were acquired roughly as a 60 nm, 4 nm and 4 nm, respectively. Thus, we can assume the number of layers for tin oxide and platinum, and the calculated results were confirmed in figure 3.10. It is assumed that the roughness, agglomeration, volume and shape changes were ignored and the particles were packed like as cubic. It is certain that the surface coverage is increased as the larger loading amounts of tin oxide in a constant weight of catalyst. Plots demonstrated that the surface coverage degree of Pt-SnO_2/C nanocomposites with low tin oxide amounts was lower than a single layer, whereas that of nanocomposites with high tin oxide

amounts exceeds 100 %. This result showed highly intimate correlations between surface coverage, electrochemical performances and shapes of cyclic voltammograms, as seen in figure 3.10.

On the other hand, it has been reported that the metal oxide in contact with metal particles can change the electronic structure of the metal catalyst. These changes in the electronic structure can lead to a more efficient oxidation of the intermediates or to weaker Pt-CO interactions with similar outcome [7,18]. This phenomenon can be confirmed by X-ray absorption near-edge structure (XANES) of Pt L_3 edge, commonly known as white line. The alteration of the d-band structure is induced from electron transfer between metal compounds. The Pt L_3 edge XANES spectra of Pt-SnO_2/C samples were shown in figure 3.11, where the white line is the lesser intense in the more Sn-rich electrocatalysts. This reduction is consistent with experimental observations that the Pt L_3 white line is decreased as increasing the tin oxide amounts, which due to the charge transfer from Sn to Pt [19,20]. Not only can the neighboring metallic atoms usually take place the shifts of white line, but also the tin oxide nanoparticles adjacent to the Pt nanoparticle induce the electron density, as observed in figure 3.11.

Furthermore, it has also been suggested that saturation of SnO_2 sites by H_2O/OH weakens the interaction of water with Pt, making the metal active sites available for ethanol oxidation [11]. The decrease of the onset potential observed for all bimetallic catalysts studied here and the peak current densities observed for some of them can be partially explained by these

effects. However, the electrocatalytic performance of the composites clearly also depends on the morphology and quantity of the metal oxide nanoparticles present on the sample. When the carbon surface is homogeneously and almost entirely coated with tin dioxide and platinum nanoparticles, like as Pt-SnO_2(40)/C, low oxidation peak current densities are observed. Tin oxide has low electrical conductivity, therefore, excess amounts of tin oxide nanoparticles dispersed on the carbon surface generates as an isolating barrier that hinders the electron transfer between platinum and carbon support.

The electrocatalytic performance is significantly improved when small clusters of Pt and SnO_2 nanoparticles are formed. This morphology facilitates the hydroxyl functional group transfer from the metal oxide to the platinum at lower potentials and also the electron transfer between carbon and platinum. The optimal performance is obtained for a SnO_2/Pt ratio of 1.0 as discussed above, suggesting that the size and amount of the clusters also play an important role on the electrocatalytic activity, with the number of three-phase boundaries being maximized in this case.

The number of interfacial regions between tin dioxide and platinum decreases for lower molar ratio of oxide and platinum, i.e., not all Pt nanoparticles are in contact with the metal oxide, which limits the adsorbed hydroxyl group transfer between metal oxide and metal, as illustrated in figure 3.12.

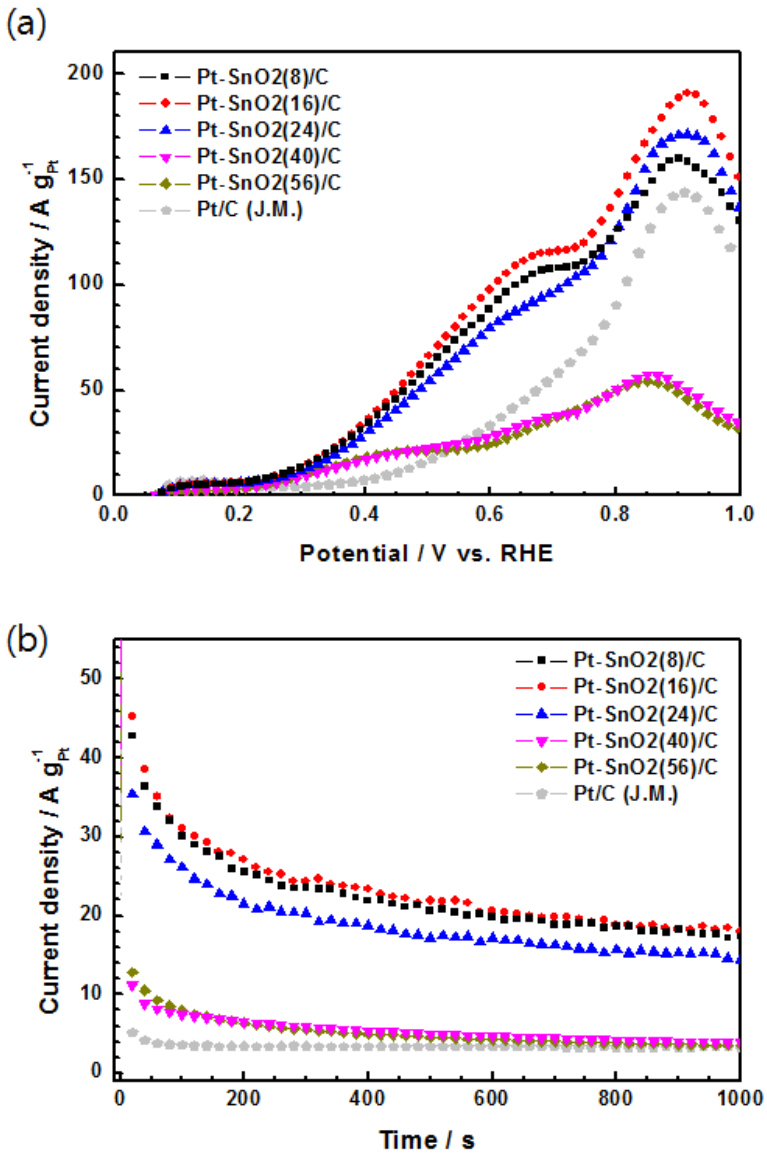

Figure 3.7. (a) Polarization curves for Pt-SnO_2/C nanocomposites and (b) their chronoamperometry data at a constant potential of 0.5 V during 1000 seconds in mixture of 0.1 M perchloric acid and 0.1 M ethanol solution under argon purging

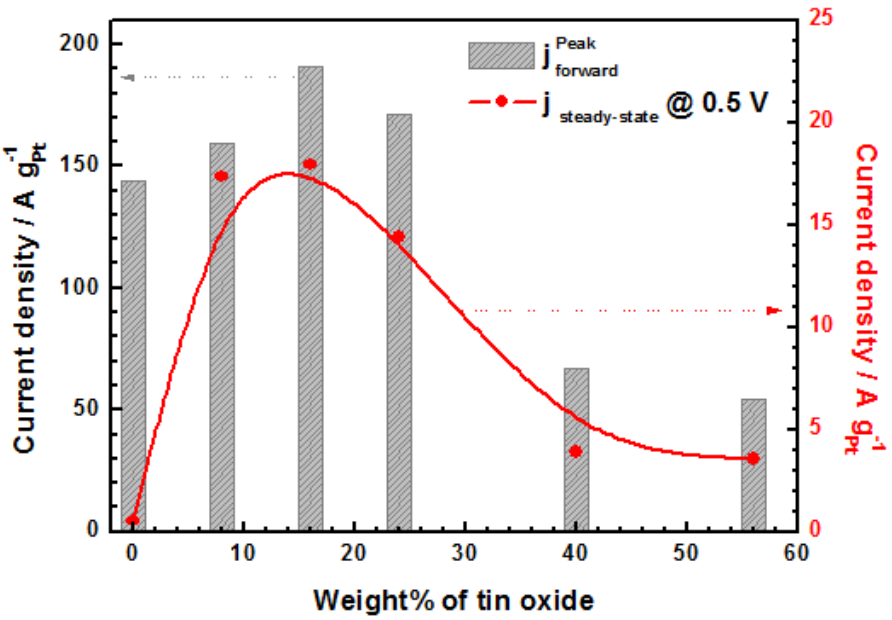

Figure 3.8. Summarized results of all electrocatalysts for peak current densities of forward scan (bar) and current densities at a constant potential of 0.5 V under the steady state (line)

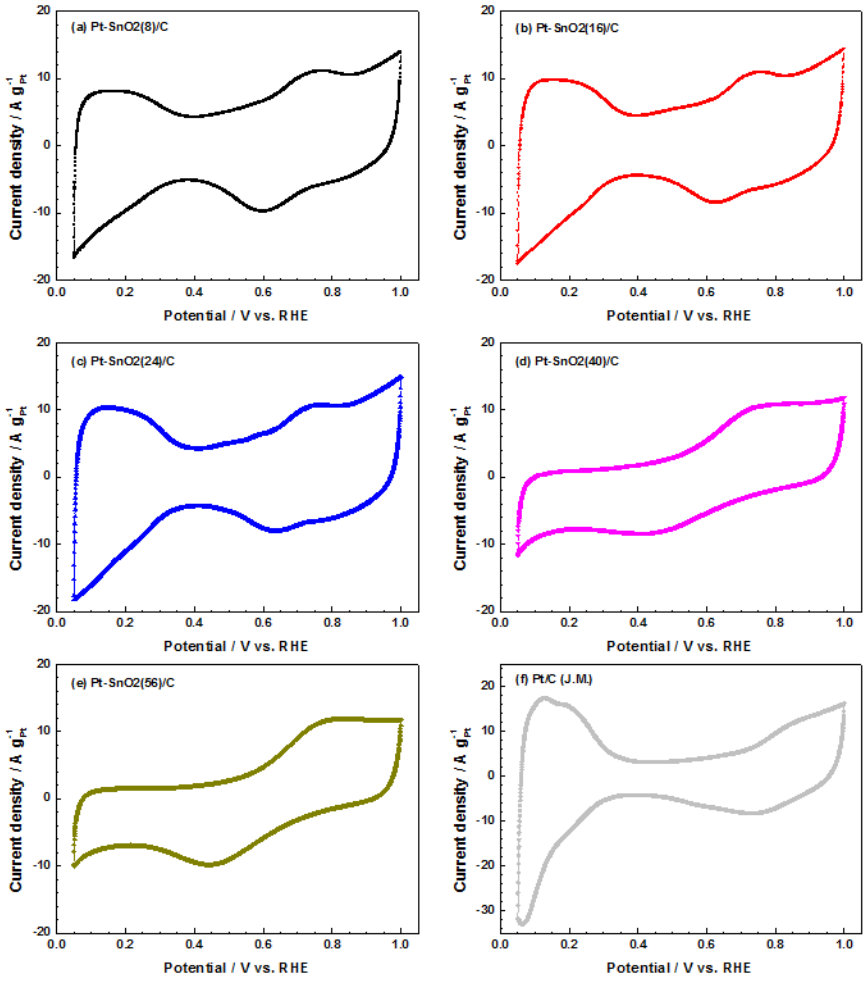

Figure 3.9. Cyclic voltammograms of (a) Pt-SnO_2(8)/C, (b) Pt-SnO_2(16)/C, (c) Pt-SnO_2(24)/C, (d) Pt-SnO_2(40)/C, (e) Pt-SnO_2(56)/C and (f) commercial Pt/C (J.M.), respectively, under oxygen-free 0.1 M perchloric acid electrolyte at a scan rate of 20 mV s^{-1}

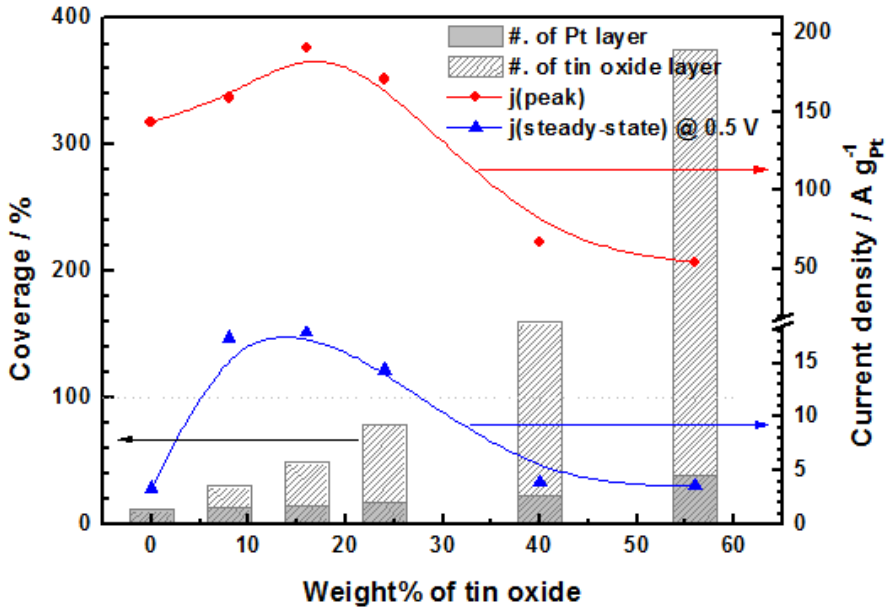

Figure 3.10. Relationship between surface coverage of carbon by platinum nanoparticles (bar with dark grey color) and tin oxide nanoparticles (bar with grey color) and activity of ethanol oxidation for peak current density (red circle) and current density at steady-state (blue triangle)

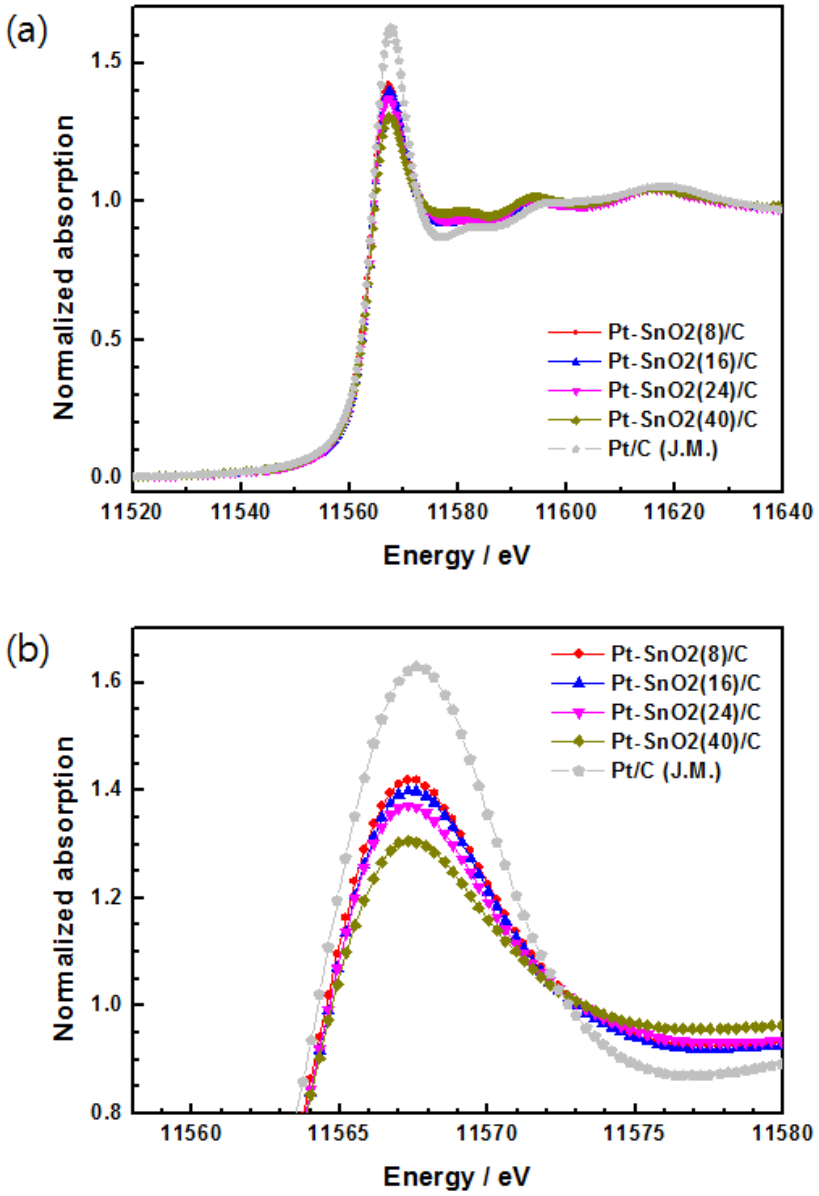

Figure 3.11. (a) XANES spectra of Pt L_3-edge in Pt-SnO_2/C electrocatalysts and commercial Pt/C and (b) their magnified spectra at the region of white line

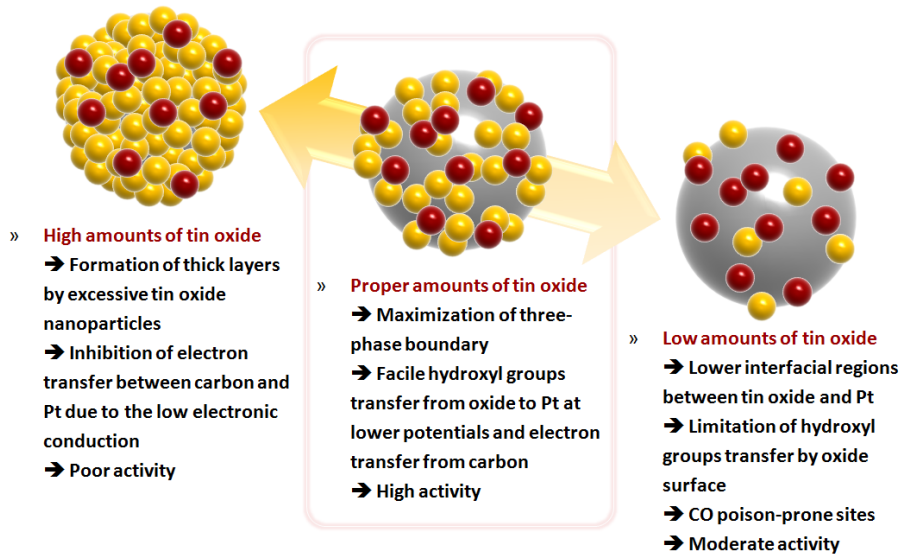

Figure 3.12. Illustrations of morphological concepts between the tin oxide amounts in Pt-SnO_2/C and the electrochemical properties

3.1.3. Electrochemical stability test

The electrochemical stability of the Pt-SnO_2(16)/C bimetallic catalyst was further investigated by performing ADT (accelerated degradation test), which consisted of 1000 potential cycling between 0.5 and 1.0 V in 0.1 M perchloric acid electrolyte at a scan rate of 100 mV/s.

TEM images of the nanocomposite before and after ADT are also shown in figure 3.13(a), (b), (c) and (d), respectively. Continuous potential cycling in acidic media can lead to the growth and agglomeration of the platinum nanoparticles, either by re-deposition of previously dissolved platinum or migration on the support surface. These processes, in turn, cause platinum loss and consequently decrease the catalyst activity. As can be seen in figure 3.13, no drastic physical changes of the material are observed from the TEM images taken after ADT.

Moreover, platinum particle size distributions before and after ADT as shown in figure 3.13(e), calculated by analysis of the TEM data, confirm this observation. A median particle size of 4.2 nm was found after ADT, against 3.9 nm obtained for the pristine material, which may cause for the loss of performance observed. It has been shown before that metal oxides can have a stabilizing effect over platinum nanoparticles, because the interactions of the metal with the metal oxide are stronger than with the carbon surface, which leads to lower rates of migration, agglomeration and growth of the metal particles during potential cycling [4,5].

The CV and chronoamperometry curves of the Pt-SnO_2(16)/C catalyst before and after 1000 potential cycles are compared in figure 3.14(a) and (b), respectively, with the initial curves of commercial catalyst. After potential cycling, a slight increase in the onset potential of ethanol oxidation (from 0.21 to 0.24 V) is observed, in addition to a decrease of the peak current density (c.a. 13 % for the anodic oxidation peak). Moreover, a faster decay of the current density with time is also seen in figure 3.14(b). Nevertheless, even after 1000 cycles, the performance of the Pt-SnO_2(16)/C catalyst on the EOR is quite superior to that of the commercial one as Pt/C, indicating a significant stability of the former, in agreement with the TEM results.

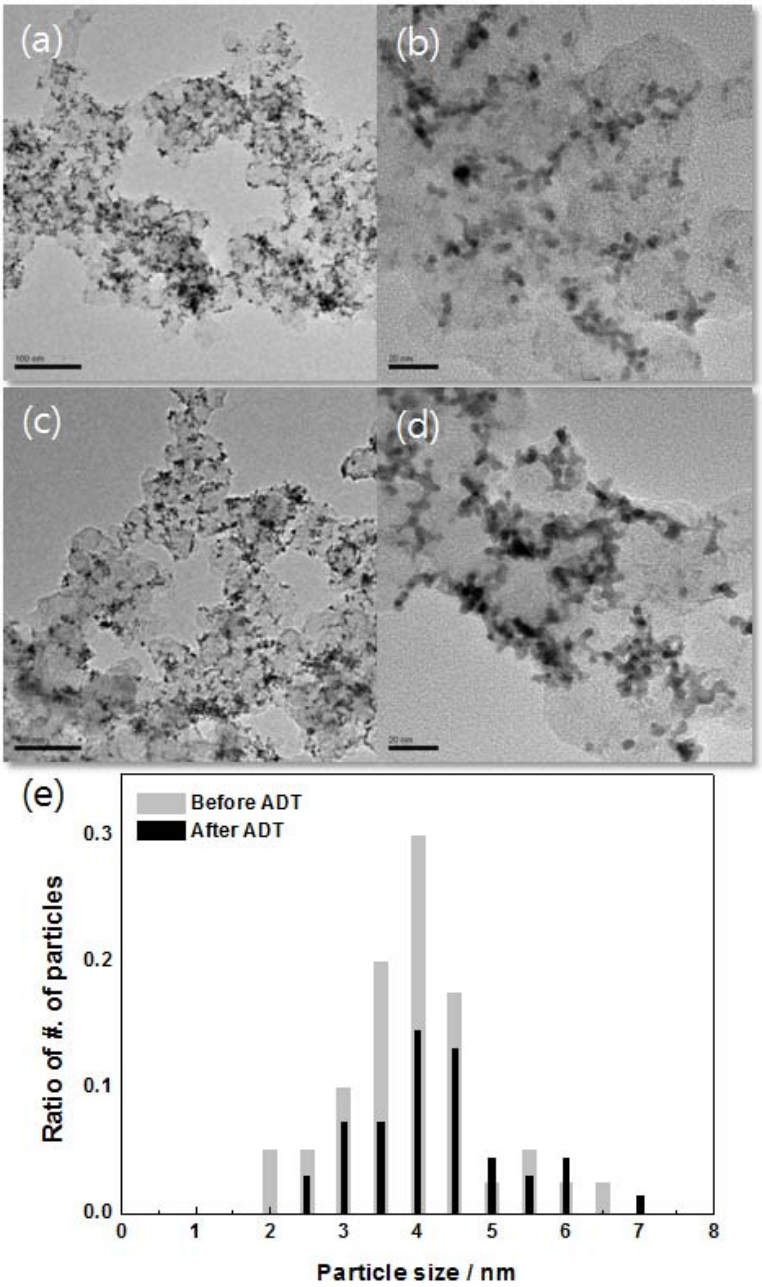

Figure 3.13. TEM images of Pt-SnO_2(16)/C sample (a, b) before ADT and (c, d) after ADT, and (e) particle size distributions

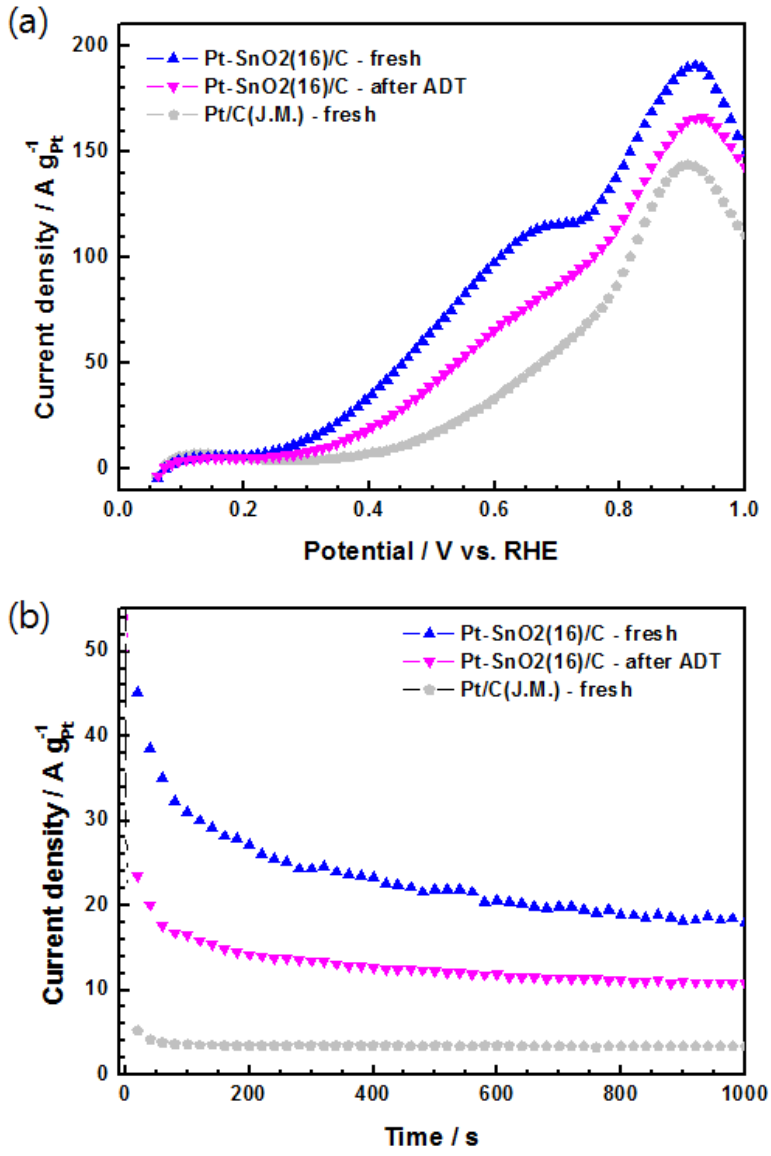

Figure 3.14. (a) Mass specific current densities before and after ADT of Pt-SnO_2/C samples and (b) chronoamperometry data at a constant potential of 0.5 V during 1000 seconds in mixture of 0.1 M perchloric acid and 0.1 M ethanol solution under argon purging

3.2. Heterogeneous rhodium – tin alloy nanoparticles

3.2.1. Physicochemical characterization

Before the structural and electrochemical characterizations, the quantitative information of metallic compounds in the carbon supported heterogeneous rhodium-tin (Rh-Sn) alloy nanoparticle should be revealed to clearly confirm the amounts of reduced metallic compounds and the precisely controlled molar ratios between two metals through the thermogravimetric analysis (TGA) and inductively coupled plasma atomic emission spectroscopy (ICP-AES), respectively.

As seen in figure 3.15, all samples showed about 20 wt% of metallic residues in each electrocatalyst from TGA results. In addition to the thermally analyzing methods, the atomic information was also investigated for all samples via atomically analyzing method and summarized in table 3.2. In order to dissolve the noble metals such as platinum and gold, aqua regia is usually used as dissolving solutions that composed of the concentrated nitric acid and hydrochloric acid optimally in a volume ratio of 1:3. Unfortunately, the rhodium and a few other metals are capable of withstanding its corrosive properties. Therefore, small amounts of concentrated sulfuric acid were added into the prepared aqua regia. According to the ICP-AES results, the molar ratio of rhodium and tin in all samples exhibited similar values compared to the expected ratios, and the electrocatalysts were denominated using the

analyzed and calculated molar ratios.

From the transmission electron microscopy (TEM) and high-resolution TEM (HR-TEM) for Rh-Sn samples, the particle size, size distribution and composition of a single nanoparticle were investigated.

TEM images and size distribution of Rh_{85}-Sn_{15}/C were shown in figure 3.16. Average particle size of Rh_{85}-Sn_{15} nanoparticle was approximately 3.3 nm with a standard deviation of 0.655, which had a smaller standard deviation than carbon supported platinum prepared by thermal reduction method, in spite of similar average particle size. The bimetallic nanoparticles were highly uniformly distributed onto the whole surface of carbon supporting material as observed in graphical images.

As the tin amounts were increased in an electrocatalyst, the alloyed nanoparticle was dimmed on the TEM images. It is likely that the tin existed in amorphous-like structure or had a higher oxidation state rather than metallic state. In order to enhance the visualizing and understanding, the HR-TEM images of Rh_{28}-Sn_{72}/C were taken with the highlighted black spots at active sites and the mapping process by EDS was achieved at a selected area as suggested in figure 3.17(a) and (b), respectively. The green squares stand for the tin, and the red squares indicate the rhodium at the EDS spectra, and these squares were uniformly dispersed on certain areas like a nanoparticle. The weight percent of tin and rhodium at a selected area were 77.7 and 22.3, respectively, corresponding to the ICP-AES results.

In figure 3.18, the HR-TEM images were also collected for the

electrocatalyst as the Rh_{62}-Sn_{38}/C, and the line scanning was submitted on a nanoparticles by EDS. Only a nanoparticle was selected for line scanning from the HR-TEM image of figure 3.18(b) and (c), the intensities of rhodium and tin exhibited along the distance at a scale of few nanometers. The ratio of intensity for rhodium and tin was accordance with ICP-AES results, and the ranges of intensity were also well-fitted with TEM data. From the EDS measurements, it is undoubtedly confirmed that the carbon supported rhodium-tin alloy nanoparticle was successfully synthesized through the microwave-assisted method.

Structural features of rhodium-tin alloy electrocatalysts were investigated by X-ray diffraction (XRD) as seen in figure 3.19. The diffraction peak at around 25^{o} is attributed to the diffraction at the (002) plane of the hexagonal structure of Vulcan as a carbon. In terms of the large amounts of rhodium in an electrocatalyst, the diffraction patterns showed the three main characteristic peaks of the face-centered cubic (fcc) crystalline rhodium, namely the planes (111), (200) and (220). As the portion of rhodium is decreased in an electrocatalyst, these three peaks were shifted in the peak positions for the lower 2θ values caused by an enlargement in the lattice parameters due to the longer lattice parameter of tin-based structures [21].

In addition to the negative peak shifts, some other peaks at around 34^{o}, 43^{o} and 52^{o} are becoming more visible, which can be related to structures of tin oxide, namely the planes (101), (210) and (211), respectively. The tin oxide peaks were grown in intensity and the rhodium peaks were diminished in

intensity with the increase of tin contents, and the similar results were also revealed from Adzic's group [22]. Silva and others reported that the positions of the diffraction peaks remained in the non-alloyed system, while the peak shifts could be observed in the alloyed system [23]. According to the XRD results and atomic mapping data by EDS, the rhodium-dominant electrocatalysts maintained a fair alloyed system, but partial segregation or alloy of tin oxide with an alloyed system was introduced as decreasing amounts of rhodium as a noble metal.

It is widely known that the rhodium is resistant to corrosion and oxidation in moisture and oxygen species, whereas tin, especially surface of tin, is easily transformed into the tin dioxide (SnO_2) under oxidative conditions. Moreover, tin does not like to form wide solid solution with other metals in general, and few elements have appreciable solid solubility in tin, for example, bismuth, lead, zinc, thallium and gallium. These intrinsic properties of metal can cause heterogeneous alloy formation of rhodium and tin with partial segregation systems by tin oxide.

In order to elucidate the compositions and chemical states of the prepared Rh-Sn/C electrocatalysts, the high resolution X-ray photoelectron spectroscopy (HR-XPS) was measured at the 8A1 beamline of Pohang Accelerator Laboratory. Using this beamline, tiny amounts of specified element can be clearly detected, and the incident photon energy can be also controlled to observe the surface and bulk properties of the samples. Seah and Dench reported that the depth of analysis can be directly derived from the

inelastic mean free paths if the information of the outermost atomic layer is required, and the inelastic mean free paths of electrons in solids obey a universal curve [24]. According to the universal curve, the inelastic mean free paths have the minimum value of approximately 0.5 nm when the kinetic energies are ranged about from 50 to 100 eV. Crystal structures usually have about 0.3 nm of distances, thus the extremely surface-sensitive information (almost monolayer) can be obtained under these kinetic energy ranges.

The Rh 3d and Sn 3d peaks of the heat-treated Rh-Sn/C electrocatalysts were measured through the XPS with 630 eV of the incident photon energy, as shown in figure 3.20(a) and (b), respectively. Furthermore, the same procedures were performed under 1000 eV of the incident photon energy in figure 3.21. From the changes of the incident photon energy, the surface-sensitive compositions of materials are evaluated from a lower incident energy measurement, whereas the core-sensitive properties are dominant in the results under a higher incident energy measurement.

Metallic rhodium appears as a spin-orbit doublet at 307.6 eV as Rh $3d_{5/2}$ and 312.4 eV as Rh $3d_{3/2}$. Peak intensities of Rh_2O_3 are set at 309.6 eV (Rh $3d_{5/2}$) and 314.4 eV (Rh $3d_{3/2}$), respectively. Peak intensities of metallic tin and tin dioxide as the most stable state of tin are 486.0 eV (Sn $3d_{5/2}$), 494.5 eV (Sn $3d_{5/2}$), 488.0 eV (SnO_2 $3d_{5/2}$) and 496.5 eV (SnO_2 $3d_{3/2}$), respectively. Curve-fitting was executed via an AVANTAGE program, and the summarized data were suggested in table 3.3.

From curve-fitting on the results received from the measurement under 630

eV of the incident photon energy, it was noticed that the rhodium existed two states such as zero-valent state (metallic Rh) and Rh(III), and the ratio of these states was changed with composition. For the all electrocatalysts, the metallic phase was intensified due to the intrinsic property of noble metal. The ratio of zero-valent state of rhodium in Rh/C, Rh_{85}-Sn_{15}/C, Rh_{62}-Sn_{38}/C, Rh_{42}-Sn_{58}/C and Rh_{28}-Sn_{72}/C was 77.6, 99.8, 98.9, 90.0 and 84.9 %, respectively. It was found that most of tin existed as a Sn(IV) state, and the ratio of oxidized tin is increased with decreasing rhodium contents in electrocatalysts. The ratio of Sn(IV) state of tin in Rh_{85}-Sn_{15}/C, Rh_{62}-Sn_{38}/C, Rh_{42}-Sn_{58}/C, Rh_{28}-Sn_{72}/C and Sn/C was 83.6, 95.3, 99.4, 99.8 and 99.9 %, respectively.

The core properties were a similar trend with surface-sensitive results through the HR-XPS measurement with 1000 eV of the incident photon energy. The ratio of zero-valent state of rhodium in Rh/C, Rh_{62}-Sn_{38}/C, and Rh_{28}-Sn_{72}/C was 99.3, 97.1 and 95.2 %, respectively. The ratio of Sn(IV) state of tin in Rh_{62}-Sn_{38}/C, Rh_{28}-Sn_{72}/C and Sn/C was 82.2, 90.8 and 92.9 %, respectively.

It can be concluded that most of rhodium and tin were existed as metallic rhodium and oxidized tin in a heterogeneous alloyed nanoparticle, and the metallic properties were maintained well at the core part of a particle compared to the surface.

The Rh 3d core-level peak of the Rh-Sn/C samples with low amounts of rhodium was slightly shifted to a higher binding energy more than the rhodium-abundant samples, which is attributed to the changes in the nearest

neighbors surrounding the Pt atom [25,26]. The variation in the d-band center for metal overlayers is also accompanied by a similar variation in the core level shift. In addition, according to the effective medium theory, the upshift of binding energy can be induced by a decreased number of neighboring Rh atoms around a single Rh atom [27].

It is interesting that the carbon supported rhodium electrocatalyst liberated from the tin element exhibited the higher ratio of oxidized part at the surface than other tin-containing samples. This result can be explained that the nonexistence of the lateral repulsion of adsorbed hydroxyl groups. A nanoparticle has significantly large surface area, that is, the surface of a nanoparticle is prone to oxidize in atmospheric conditions. For this reason, the rhodium nanoparticle has partially oxidized surface. However, if the small amounts of tin are submitted on the rhodium surface, the oxidizing species like to form a tin oxide from a tin rather than oxidation of rhodium. Oxidized tin easily adsorbs the oxygen species such as hydroxyl groups, results in the inhibition of further access of hydroxyl groups to the rhodium surfaces by its repulsion [28].

According to the above results, the surface and bulk properties of the carbon supported heterogeneous alloy Rh-Sn electrocatalysts were expressed as a scheme in figure 3.22. Atomic compositions were fixed from the ICP-AES results, and particle size was determined from the HR-TEM results. Heterogeneously alloyed system was confirmed from the HR-XRD measurement. Surface properties about from a surface to the second layer and

bulk (core) properties were observed from the HR-XPS results. The changes of lattice parameter were ignored due to the complex and irregular system. (Rhodium has a face-centered cubic structure, while tin or tin oxide has tetragonal structure.) Thus, this scheme can’t express real crystal structure exactly, however, it is certain that it can promote the understanding for the nano-scaled electrocatalyst structures approximately.

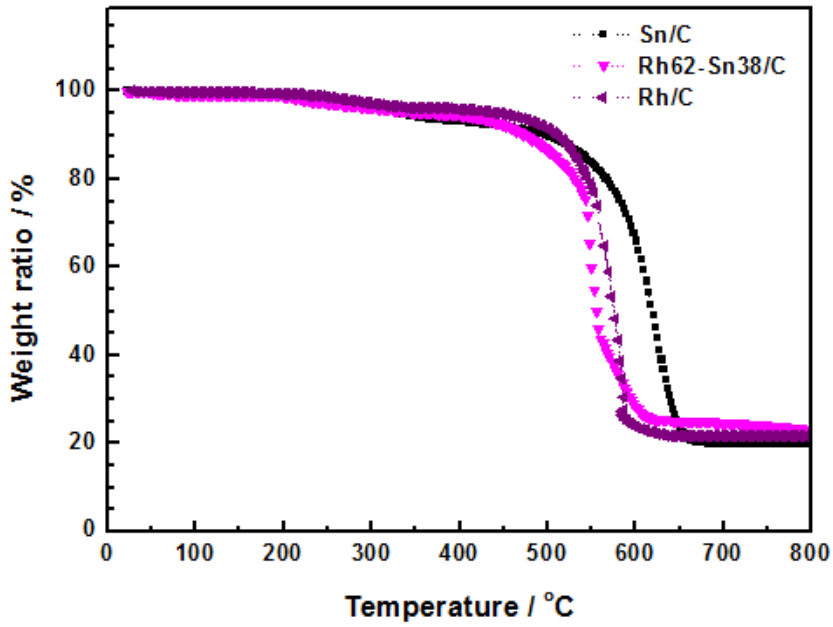

Figure 3.15. Thermogravimetric analysis data of Rh/C, Sn/C and Rh_{62}-Sn_{38}/C samples

Table 3.2. Summarized data of compositions of samples with theoretically calculated molar ratios, measured molar ratios by ICP-AES

Sample	Theoretical molar ratios	ICP-AES (molar ratios)	Denomination
Rh_0-Sn_{100}/C	0 : 100	0 : 100	Sn
Rh_{30}-Sn_{70}/C	30 : 70	28 : 72	Rh_{28}-Sn_{72}
Rh_{50}-Sn_{50}/C	50 : 50	42 : 58	Rh_{42}-Sn_{58}
Rh_{70}-Sn_{30}/C	70 : 30	62 : 38	Rh_{62}-Sn_{38}
Rh_{90}-Sn_{10}/C	90 : 10	85 : 15	Rh_{85}-Sn_{15}
Rh_{100}-Sn_0/C	100 : 0	100 : 0	Rh

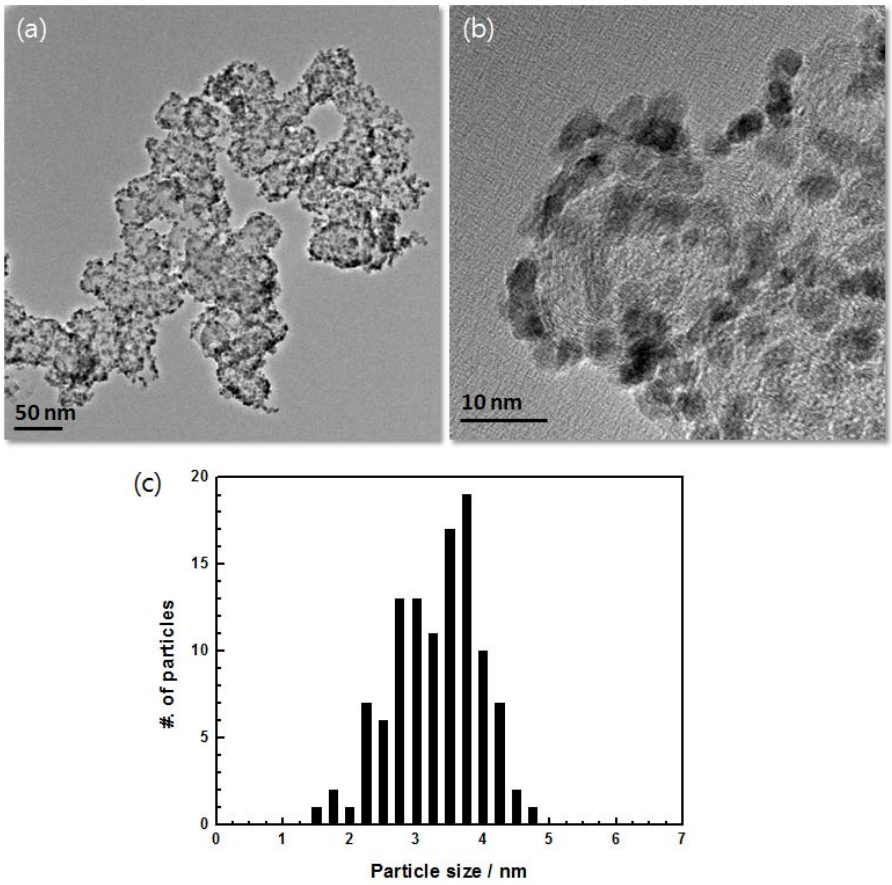

Figure 3.16. TEM images of Rh_{85}-Sn_{15}/C catalyst at (a) low magnification and (b) high magnification, and its (c) particle size distribution

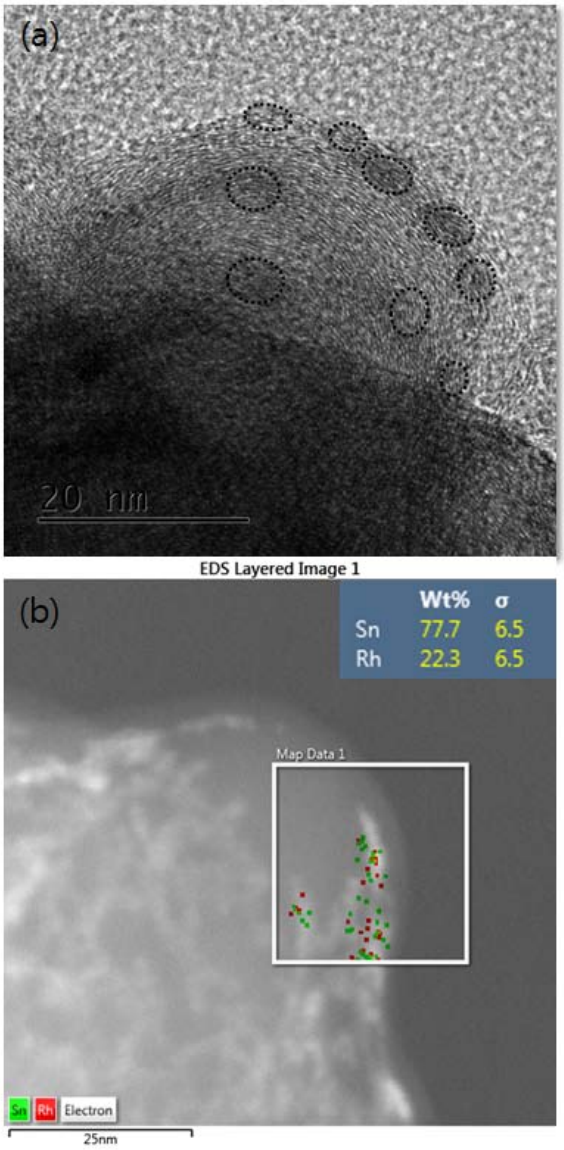

Figure 3.17. HR-TEM images of Rh_{28}-Sn_{72}/C catalyst at (a) high magnification with highlighted spots at active materials, and (b) their mapping results with red square (Rh) and green square (Sn) using EDS. Inset: weight % of each metal in selected area

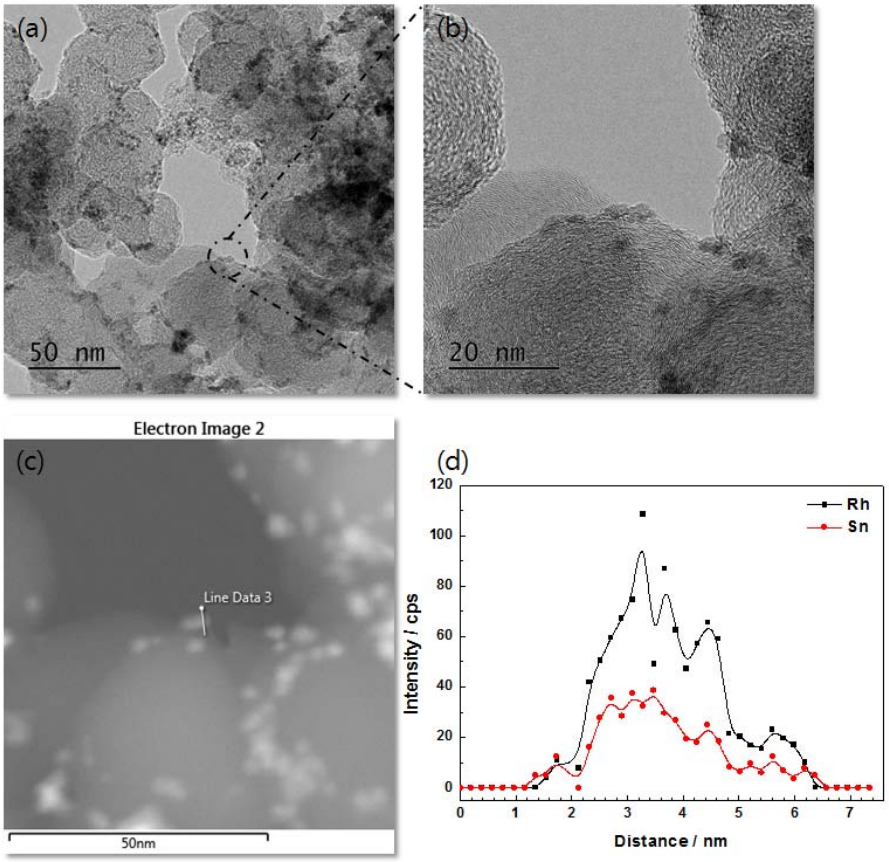

Figure. 3.18. (a) HR-TEM images of Rh_{62}-Sn_{38}/C catalyst with low magnification and (b) high magnification at selected position. (c) The line scanning position of a nanoparticle by EDS and (d) the results for intensities of two metallic components along the distance

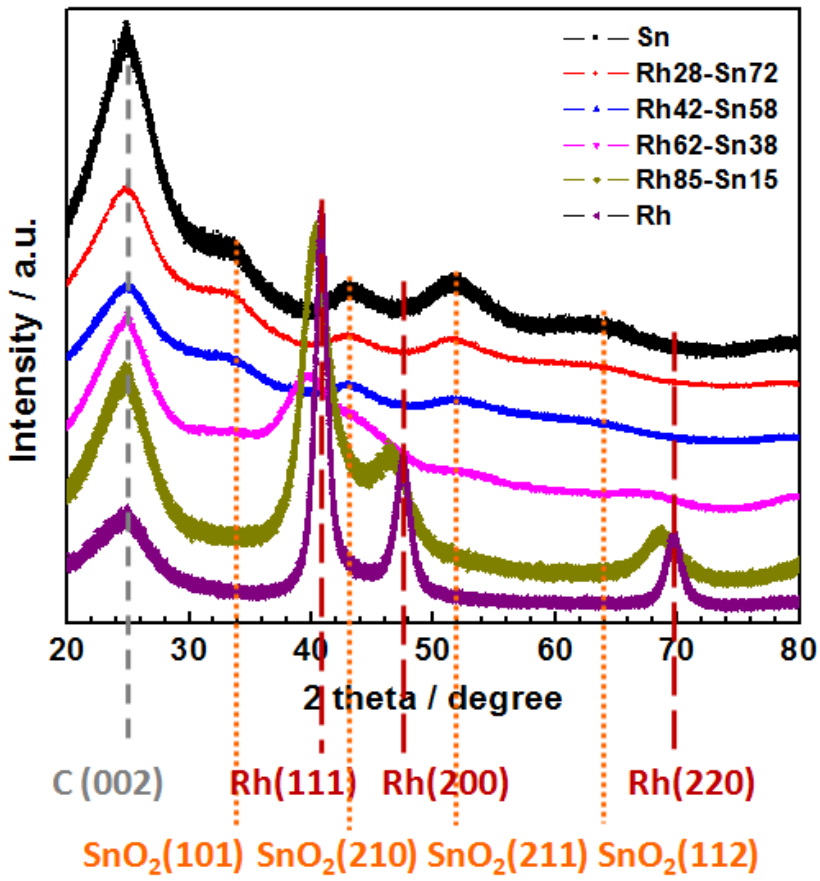

Figure 3.19. High resolution XRD patterns of carbon supported rhodium-tin alloy electrocatalysts at a scan rate of 0.1^{o} $minute^{-1}$

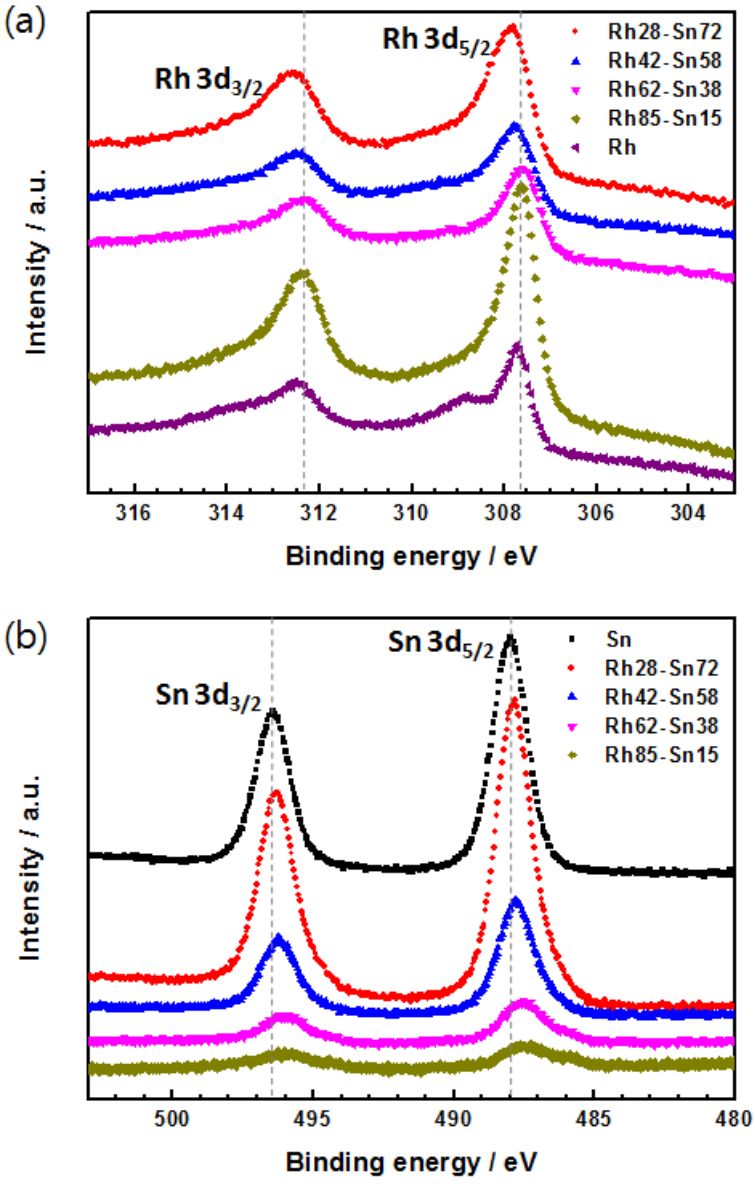

Figure 3.20. XPS spectra of (a) Rh 3d orbital and (b) Sn 3d orbital with a set energy of 630 eV

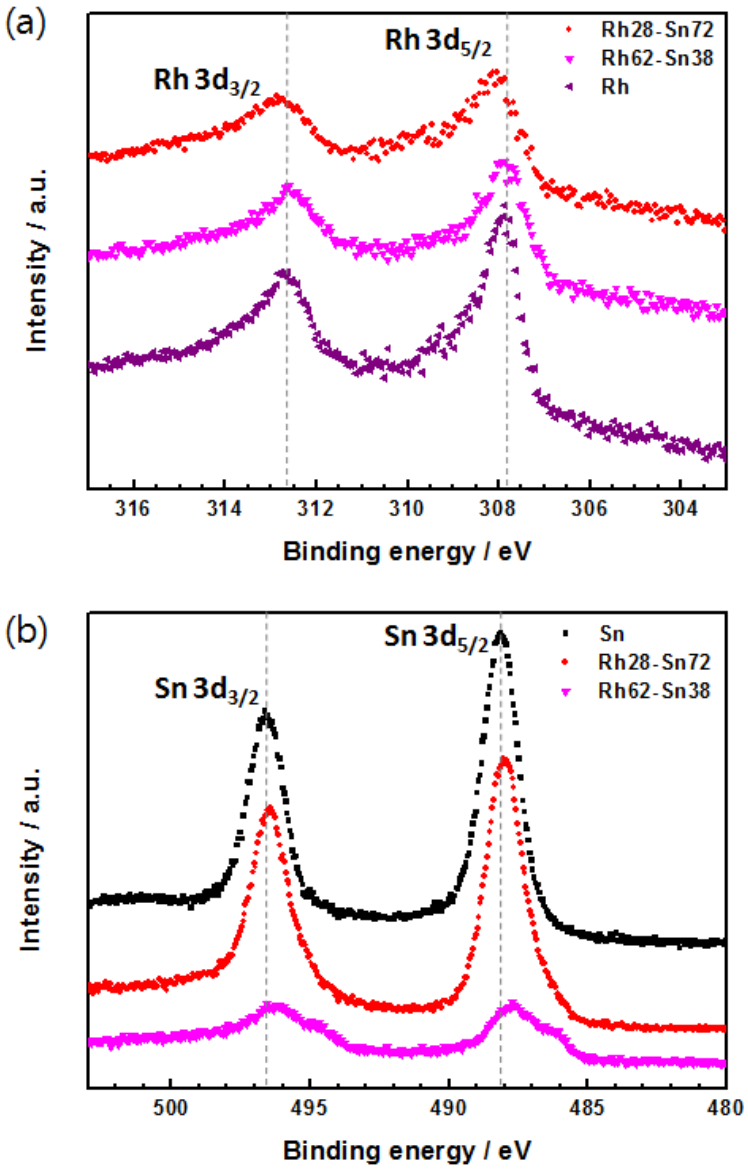

Figure 3.21. XPS spectra of (a) Rh 3d orbital and (b) Sn 3d orbital with a set energy of 1000 eV

Table 3.3. Deconvoluted and summarized data of XPS results for Rh-Sn electrocatalysts

Sample	Set energy	Rh / %		Sn / %	
		0	3+	0	4+
Sn/C	630 eV	N/A	N/A	0.02	99.98
	1000 eV	N/A	N/A	7.07	92.93
Rh_{28}-Sn_{72}/C	630 eV	84.93	15.07	0.16	99.84
	1000 eV	95.19	4.81	9.22	90.78
Rh_{42}-Sn_{58}/C	630 eV	89.98	10.02	0.64	99.36
	1000 eV	N/A	N/A	N/A	N/A
Rh_{62}-Sn_{38}/C	630 eV	98.90	1.10	4.66	95.34
	1000 eV	97.11	2.89	17.76	82.24
Rh_{85}-Sn_{15}/C	630 eV	99.76	0.24	16.42	83.58
	1000 eV	N/A	N/A	N/A	N/A
Rh/C	630 eV	77.63	22.37	N/A	N/A
	1000 eV	99.28	0.72	N/A	N/A

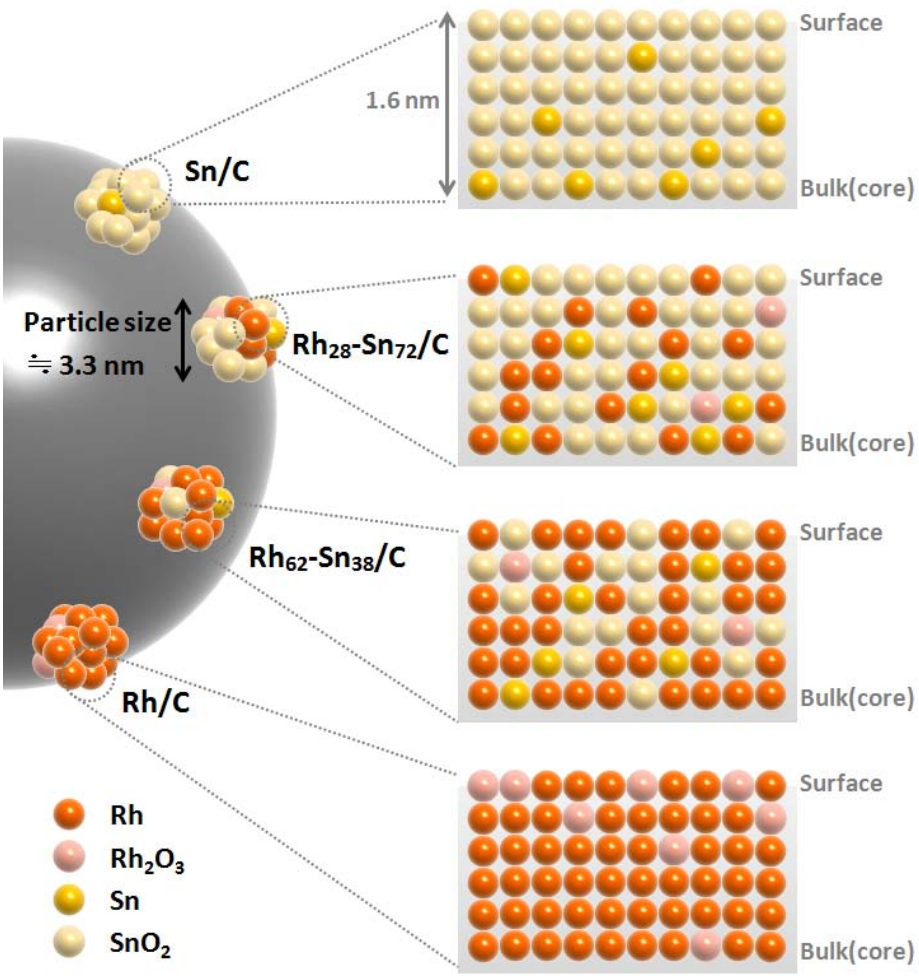

Figure 3.22. Scheme of the surface and bulk structures for the heterogeneously alloyed bimetallic nanoparticles based on the high resolution TEM, XRD and XPS results (lattice changes are ignored.)

3.2.2. Electrochemical characterization

The activity and selectivity of the Rh-Sn/C electrocatalysts for ethanol oxidation reaction was investigated by potentiodynamic and potentiostatic methods under electrochemical cell, and the electronic properties of alloyed formation were studied using x-ray absorption spectroscopy.

Polarization curves for ethanol oxidation on the rhodium-tin alloy were recorded in the mixture of 0.1 M potassium hydroxide and 0.5 M ethanol solution at room temperature with a scan rate of 20 mV s^{-1}, as shown in figure 3.23(a) and (b). The scanned potential range reaches from 0.05 V to 1.0 V at a scan rate of 20 mV s^{-1}. Carbon supported tin sample did not showed any performance, that is, only Sn can't make the activity toward ethanol oxidation. Rhodium had an activity, but too small. In terms of the Rh-Sn/C electrocatalysts, they exhibited highly active behaviors for ethanol oxidation, and some of them had superior to the commercial Pt/C electrocatalyst. The onset potential was negatively shifted as increasing Sn contents in sample, and the current density also increased. It is likely that the electrocatalyst including tin atom showed similar tendencies with this results, as a bifunctional effect [29].

Peak potential at forward scan, peak current density at forward scan and backward scan, the ratios of two peak current densities, and potential at 10 mA g^{-1} were recorded and summarized in table 3.4. Potential values at 10 mA g^{-1} can be indicated as onset potential, thus more exact potential values can be

read from these summarized data. The peak current density at forward scan was higher as the Sn contents increased with lower overpotential, but the peak potential at forward scan was also negatively moved. It indicates the Sn can easily adsorb hydroxyl species and transfer to nearby carbon monoxide (CO) species adsorbed on rhodium, results in negatively shifts of onset potentials. But the Sn has too poor to electrochemically oxidize the ethanol oxidation and bond with CO species, peak potential was appeared earlier and dropped than Rh-abundant samples.

The ratio of forward and backward peak current can be used to describe the CO tolerance of catalysts. High values imply superior CO tolerance [30,31]. This ratio of Pt/C usually showed 0.6, and that of the oxide submitted to the Pt had 0.8 ~ 0.9 in the acid medium [4]. From the results, the ratios were increased as the diminution of the Sn contents in the electrocatalyst. Especially, over the 8 was calculated as a i(f)/i(b) ratio in the case of Rh_{28}-Sn_{72}/C sample, although the highest activity was appeared. It means the Rh_{28}-Sn_{72}/C electrocatalyst had both the best activity for ethanol electro-oxidation and the tolerance for CO species.

To identify the activity duration, chronoamperometry were also performed at 0.5 V during 3600 seconds in figure 3.24. Among of them, the Rh_{62}-Sn_{38}/C sample showed the best durability. The Rh_{28}-Sn_{72}/C electrocatalyst that exhibited the best activity for ethanol electro-oxidation and the tolerance for CO species was sharply dropped for longer time. This can be explained that the chronoamperometry was recorded at 0.5 V where the maximum current

density shown in the Rh_{28}-Sn_{72}/C sample. A lot of products were intensely generated from electrochemical reaction under the obtaining chronoamperometry data, thus the products on active sites inhibits fuel adsorption to aggravate the oxidation current [32]. This tendency appeared with decreasing rhodium amounts in catalytic materials.

With the aim of evaluating the product yields of the ethanol oxidation on the different rhodium-tin alloy, *in situ* FTIR measurements were performed at several potentials. Among of a lot of products of ethanol oxidation reaction, the main purpose of this research is to confirm the complete electro-oxidation from ethanol to carbon dioxide. *in situ* FTIR spectra was received in the mixture of 0.1 M potassium hydroxide and 0.5 M ethanol solution with potentiodynamic control. Adsorbed and produced carbon dioxide at the surface of catalyst are detected at about 2343 cm^{-1}. The band intensities of carbon dioxide were plotted as a function of the potential for commercial Pt/C and Rh_{62}-Sn_{38}/C electrocatalyst as seen in figure 3.25. The band intensities were divided by the band intensity obtained at 1.0 V for each electrode. Plots showed the carbon dioxide formation was taken place even at very low potentials in Rh_{62}-Sn_{38}/C catalyst compared to the Pt/C. In terms of platinum catalyst, the ratio was too low at low potentials and reached a maximum near the 0.7 V, with lower than a half value of that of rhodium-tin alloy catalyst.

These results support the mechanism in which Rh atoms and Sn atoms play critical roles in inducing the C-C bond scission and facilitating the hydroxyl group transfer to rhodium through the bifunctional effect. It leads to the

formation of carbon dioxide and oxidation of CO species even at low potential ranges with superior activity [33].

Figure 3.26(a) and (b) proposed a linear region of the Tafel plots obtained in the mixture of 0.1 M potassium hydroxide and 0.5 M ethanol solution with a scan rate of 1 mV s^{-1} of Rh-Sn/C electrocatalysts and commercial Pt/C. The linear region was magnified for the Tafel plots from the onset potential to the near the peak potential. As the potential was further increased above about 0.5 V, the Tafel plot became curved, indicating that the ethanol oxidations were no longer the charge transfer controlled. The slopes were decreased with increase of tin loading amounts, finally the Tafel plot of Rh_{28}-Sn_{72}/C indicated the lowest value, considerably lower than that of commercial Pt/C at a slope of 0.176 V dec^{-1}.

Lower Tafel slope means that the charge transfer of the ethanol oxidation reaction on the catalyst are easier than that on other catalysts in the alkaline medium [34,35]. The lowest Tafel slope was found in the Rh_{28}-Sn_{72}/C at a slope of 0.108 V dec^{-1}, which had the largest portions of tin in the electrocatalysts. Maybe it will help the oxidation of the CO intermediates that adsorbed on the active sites because tin interacts strongly with hydroxyl groups, result in facile charge transfer.

For accounting the Tafel plot, specific current density was calculated using the electrochemical surface area (ECSA). The ECSA was commonly calculated from the hydrogen desorption area ranged from 0 V to 0.4 V in an argon-saturated electrolyte during cyclic voltammetry tests, however, in the

case of rhodium-tin catalyst, it's too difficult to discriminate the area of under-potential deposited hydrogen due to the oxidized surface of tin. Therefore, the carbon monoxide (CO) displacement method was adopted [36]. Strong adsorption of CO leads to the poisoning of the active sites as mentioned earlier, results from the electron donation and back-donation between CO orbital and metal atomic orbital. The oxidation of adsorbed CO on the active surface can be occurred. ($CO_{ad} + OH_{ad} \rightarrow CO_2 + H^+ + e^-$) The hydroxyl groups are formed by dissociative adsorption of a water molecule on the active surface, ranged from about 0.5 V to 0.8 V where the main oxidized peak of CO was observed.

X-ray absorption fine structure (XAFS) refers to the details of how x-rays are absorbed by an atom at energies near and above the core-level binding energies of that atom [37]. Specifically, it is the modulation of an atom's x-ray absorption probability due to the chemical and physical state of the atom. XAFS spectra are especially sensitive to the formal oxidation state, coordination chemistry, and the distances, coordination number and species of the atoms immediately surrounding the selected element. The x-ray absorption spectrum is typically divided into two regimes: x-ray absorption near-edge spectroscopy (XANES) and extended x-ray absorption fine-structure spectroscopy (EXAFS). Though the two have the same physical origin, this distinction is convenient for the interpretation. XANES is strongly sensitive to formal oxidation state and coordination chemistry (e.g., octahedral, tetrahedral coordination) of the absorbing atom, while the EXAFS is used to determine

the distances, coordination number, and species of the neighbors of the absorbing atom.

When discussing x-ray absorption, we are primarily concerned with the absorption coefficient, μ which gives the probability that x-rays will be absorbed according to Beer's Law ($I = I_0 e^{-\mu t}$) where I_0 signifies the x-ray intensity incident on a sample, t is the sample thickness, and I stands for the intensity transmitted through the sample. I_0 as a photon flux is measured via gas ionization chamber filled inert gases such as pure helium, nitrogen, argon or their mixtures at a certain pressure. Photon flux is digitized to a current generated from the instantaneous ionization of inert gases under the radiation of x-ray beam and electrodes to which submitted to extremely high potential. Transmittance intensity is determined at detector through the sample under same conditions with obtaining I_0.

In the study of fuel cell catalysts, the position of the absorption edge is related to the oxidation state of the absorbing atom and the detailed features can provide an identification of the neighbors and coordination geometry [38]. In figure 3.27 and 3.28, the background corrected and normalized XANES spectra of Rh K-edge and Sn K-edge of electrocatalysts were exhibited, respectively. The normalized intensity of Rh K-edge white line as the intense peak at the absorption edge was increased with diminution of the rhodium in the sample. Since the white line features in the Rh K-edge represent the transition from 1s orbital to hybridized 5p and 4d orbitals, the up-shifted white line was observed in Rh-Sn/C electrocatalysts may suggest a less filled

d band of Rh [39].

This implies that the electron transfers from rhodium to other compounds, results in binding more strongly with adsorbates. The intrinsic activity of rhodium is too low to treat as electrocatalytic material, but stronger adsorption of molecules such as ethanol on the rhodium by electronic effect can become a fair electrocatalyst toward electro-oxidation.

The reasons for up-shifts of white line can be explained these electronic effect as well as the nanosized effect and oxide effect. Nanosized effect can be ignored due to the comparison with the white line of nanosized rhodium. As shown in figure 3.27(a), the slopes of edge showed slightly positive shifts result from the increase oxidation state [40]. These shifts in XANES spectra is corresponding to the XPS results that the oxidation state of Rh was slightly increased with decreasing Rh amounts in sample. Therefore, the up-shift from oxide effect cannot be fully negligible. However, the Sn K-edge profiles were opposite with Rh-K edge profiles, as seen in figure 3.28. The down-shifted white line was found although most of tin was existed as a tin dioxide, which may indicate more filled d orbital of Sn [41]. Therefore, both electronic effect and oxide effect cause the changes of white line features in Rh-Sn/C electrocatalysts.

In the former part, the electrocatalyst of slightly down-shifted Pt L_3-edge exhibited better performance, in this part, however, the superior fuel oxidation ability was observed on the electrocatalyst of up-shifted Rh K-edge. Some papers have reported that the rhodium has the lower bonding energy with CO

species than that of platinum [42]. Therefore, this electronic modification via Rh-Sn alloy can reinforce the bonding energy with CO relative to interactions between native rhodium and CO.

To explore the coordination geometry of rhodium-tin alloy, the k^3-weighted Fourier transform (FT) of the Rh K-edge and Sn K-edge EXAFS signals were analyzed and presented in figure 3.29(a) and (b), respectively. Accordance with the XPS and XANES spectra, more Rh-O bonding from intensity of the first shell (1.45 Å) and less Rh-Rh or Rh-Sn bonding from intensity of the second shell (2.41 Å) were confirmed that contained the lowest rhodium amounts [43]. Sn-Sn and Sn-Rh bonding were also increased with lower amounts of rhodium observed from the first shell intensity. More oxidized Rh shell and little changes of oxidized Sn shell in Rh-lack electrocatalysts means that rhodium-tin alloy nanoparticle becomes rhodium-tin alloy with surface oxide as increased Sn contents in catalytic material. The peak splitting in case of bimetallic nanoparticles indicates the presence of two types of backscattering atoms in the first shell coordination [44].

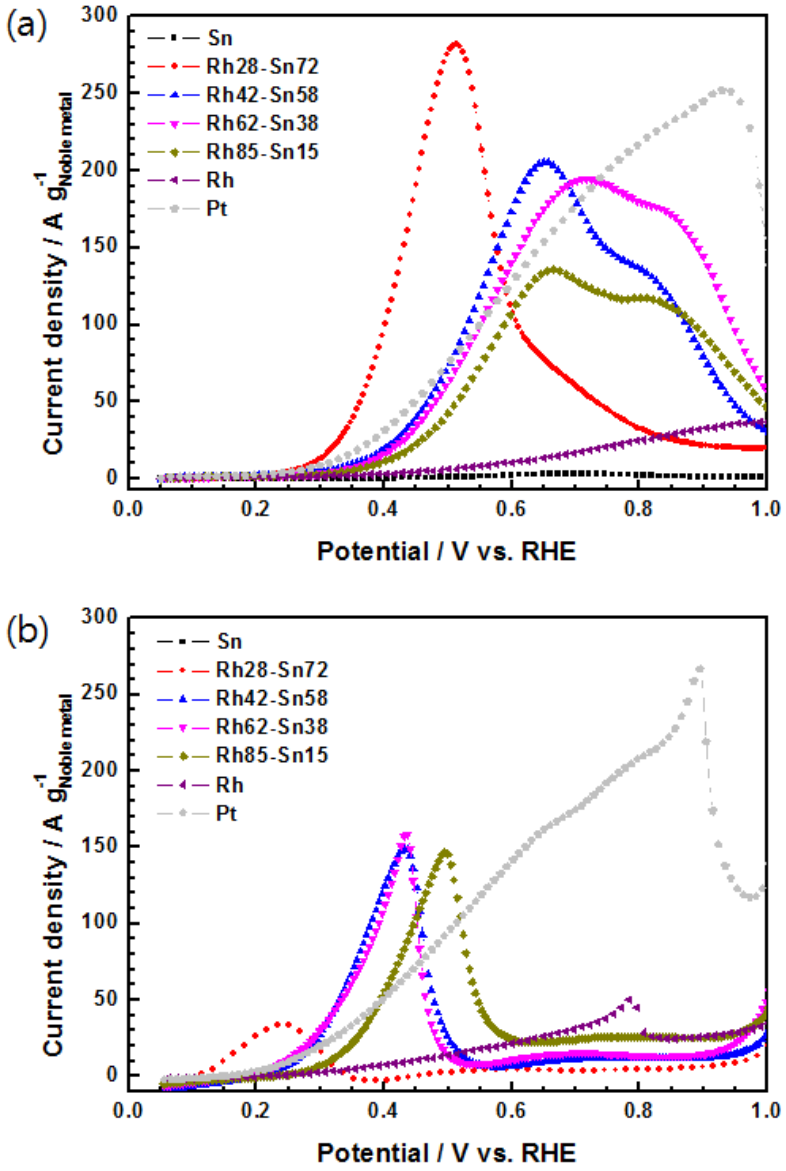

Figure 3.23. (a) Forward scans and (b) backward scans of polarization curves for Rh-Sn/C electrocatalysts in mixture of 0.1 M potassium hydroxide and 0.5 M ethanol solution under argon purging

Table 3.4 Summarized data of peak potentials, peak current densities at forward scan and backward scan and their ratios, and potentials at 0.01 A g^{-1}

	E at i(f,peak)	i (f,peak)	i (b,peak)	i(f) / i(b)	E @ 0.01 A g^{-1}_{NM}
Rh_{28}-Sn_{72}/C	0.51	281.73	33.48	8.416	0.287
Rh_{42}-Sn_{58}/C	0.65	205.61	149.33	1.377	0.355
Rh_{62}-Sn_{38}/C	0.71	194.35	159.24	1.220	0.370
Rh_{85}-Sn_{15}/C	0.67	136.04	147.08	0.925	0.392
Rh/C	0.99	36.51	51.39	0.710	0.590
Pt/C (J.M.)	0.94	252.71	267.42	0.944	0.311

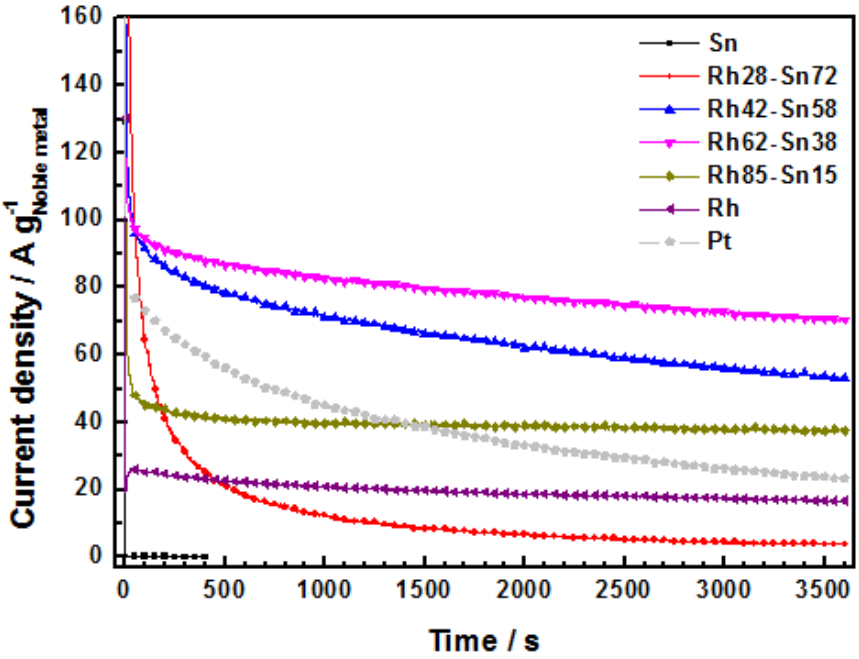

Figure 3.24. Chronoamperometry data at a constant potential of 0.5 V during 3600 seconds in mixture of 0.1 M potassium hydroxide and 0.5 M ethanol solution under argon purging

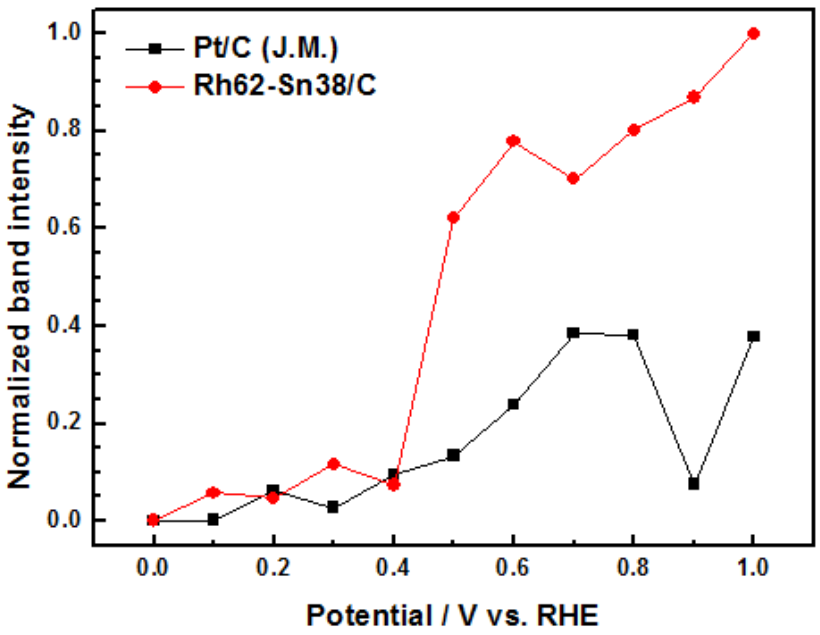

Figure 3.25. Normalized band intensity of carbon dioxide (CO_2) at a wavelength of 2343 cm^{-1} for the Rh_{62}-Sn_{38}/C electrocatalyst using *in situ* ATR-FTIR spectroscopy

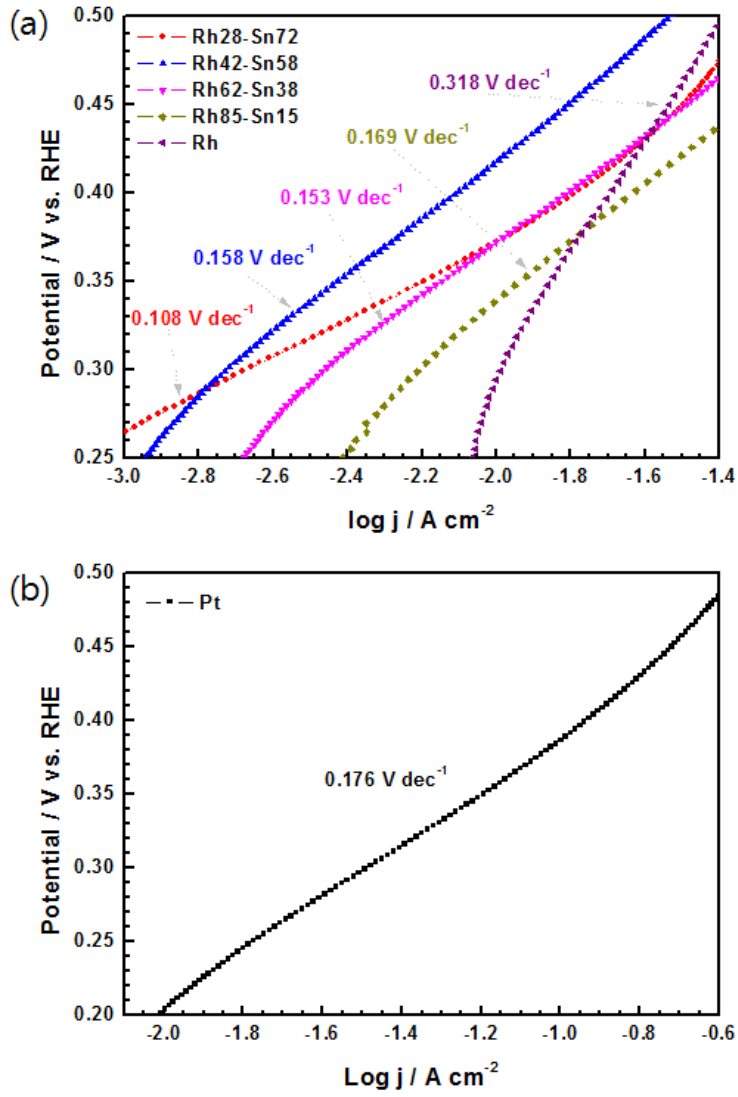

Figure 3.26. Tafel plots for ethanol oxidation on the (a) Rh-Sn/C electrocatalysts and (b) commercial Pt/C in mixture of 0.1 M potassium hydroxide and 0.5 M ethanol solution under argon purging at a scan rate of 1 mV s^{-1}

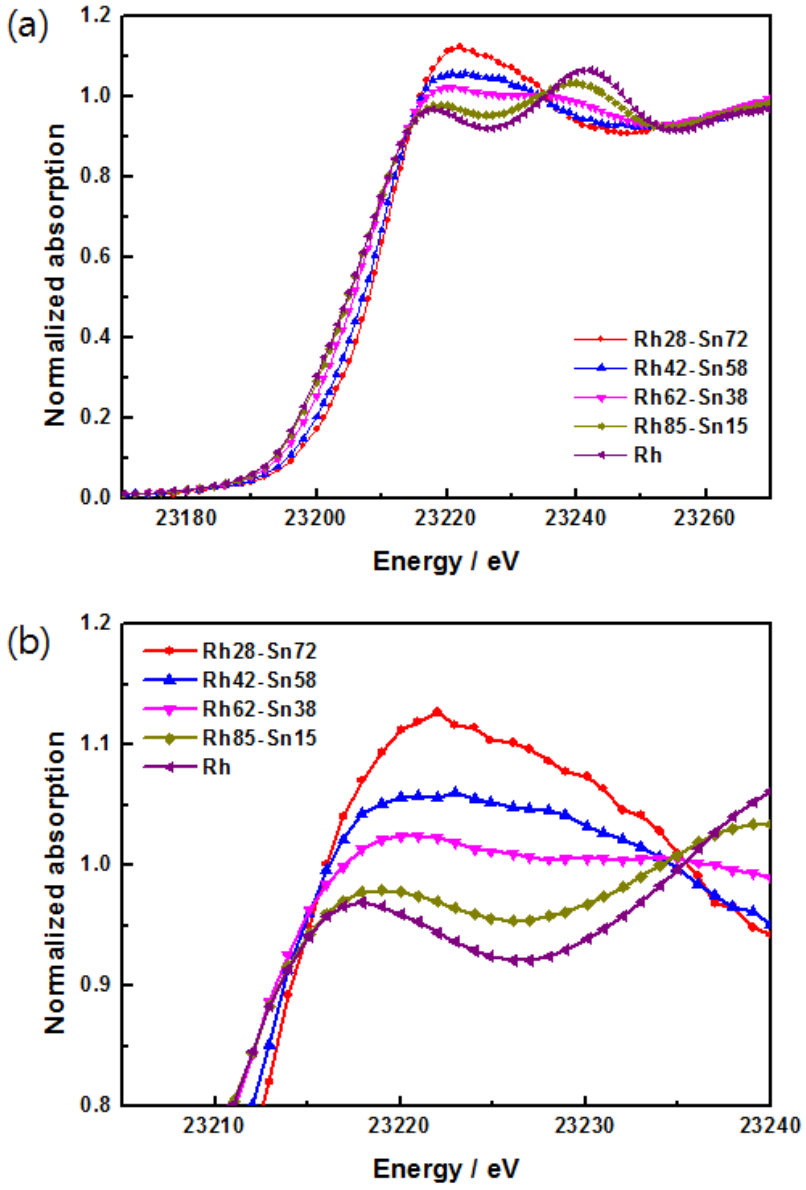

Figure 3.27. Normalized absorption intensities of (a) Rh K-edge XANES spectra and (b) white line of Rh-Sn/C electrocatalysts

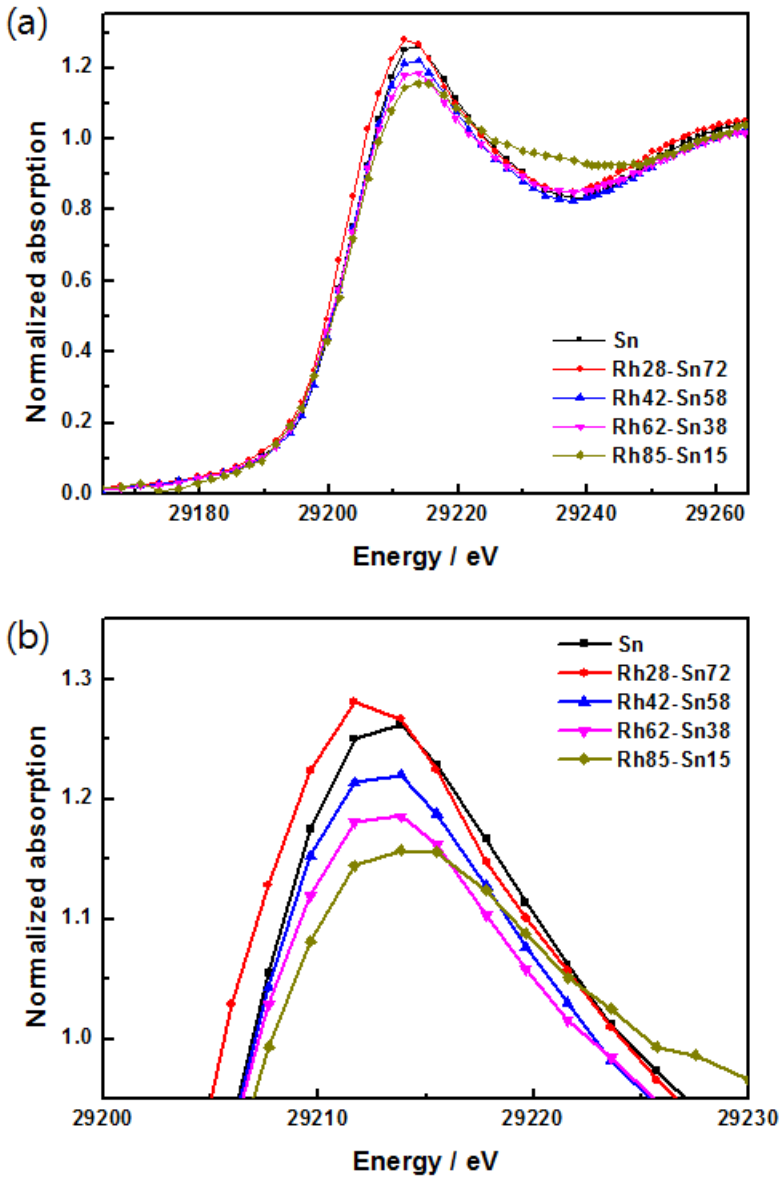

Figure 3.28. Normalized absorption intensities of (a) Sn K-edge XANES spectra and (b) white line of Rh-Sn/C electrocatalysts

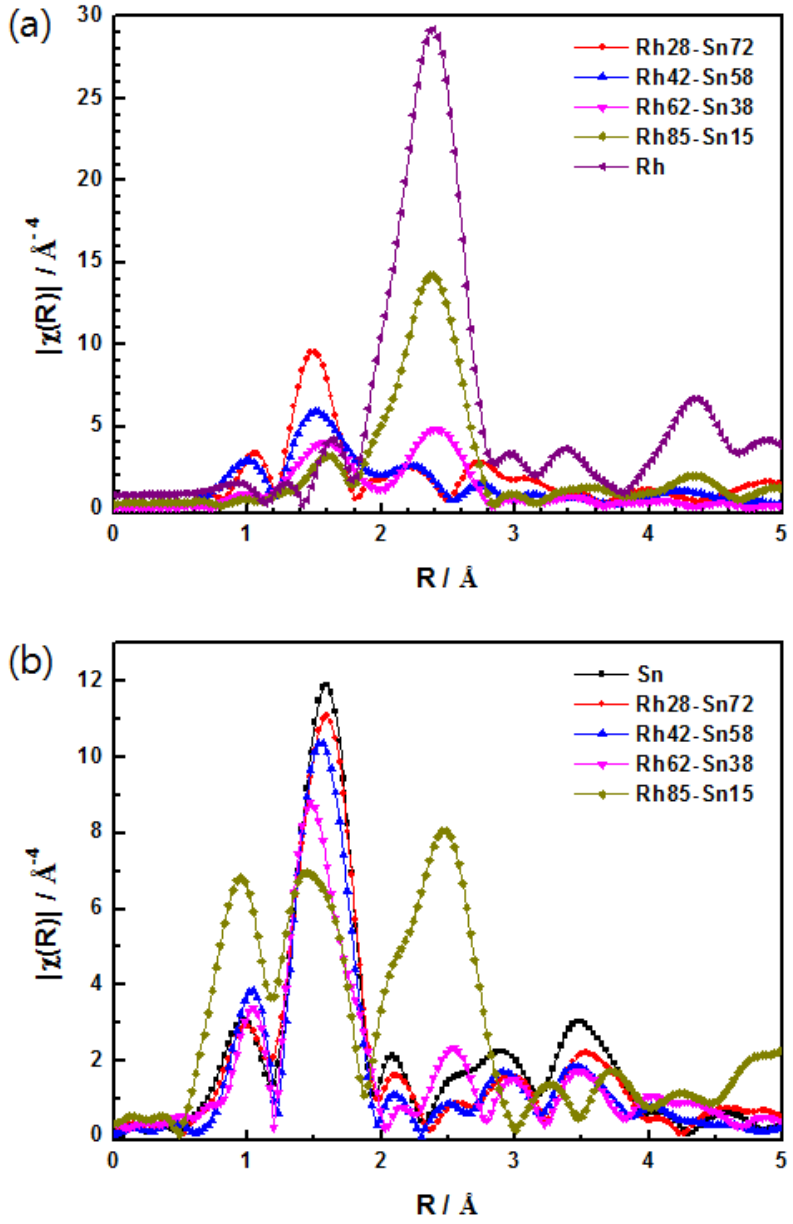

Figure 3.29. Radial distribution function of Fourier Transform (FT) of k^3-weighted (a) Rh K-edge and (b) Sn K-edge EXAFS spectra in the various Rh-Sn/C electrocatalysts

3.2.3. Electrochemical durability test

In order to confirm the electrochemical activity for ethanol oxidation under more concentrated ethanol solution and at lower potential through the intended selection of catalytic materials and their modification, the performance data were obtained in the mixture of 0.1 M potassium hydroxide and 6.0 M ethanol solution at a scan rate of 20 mV s^{-1}, as shown in figure 3.30(a) and (b). As the concentration of ethanol increased, the peak current densities were significantly improved in all Rh-Sn/C electrocatalysts, while the commercial Pt/C had less activity than at lower ethanol concentration. Among of samples, the Rh_{28}-Sn_{72}/C electrocatalyst showed the highest current density of nearly 500 A g^{-1} under the highly concentrated ethanol solution.

In the more concentrated ethanol solution, it is certain that the probability of ethanol adsorption on the active sites. At this point, the Rh-Sn/C electrocatalysts had ability to facile oxidation of ethanol and CO species through the bifunctional effect and electronic effect, thus more reactants can be further oxidized. However, the platinum has more frequent interactions with increased CO species in the concentrated ethanol solution, results from the limitation of CO species removal rate rather than further oxidation of ethanol.

In figure 3.31, chronoamperometry data were obtained in the mixture of 0.1 M potassium hydroxide and 6.0 M ethanol solution at a constant potential of 0.5 V. Substantially high current density at steady-state was observed in the

Rh_{28}-Sn_{72}/C electrocatalyst. Not only the initial current density but also current density steady-state was maintained, thus the Rh_{28}-Sn_{72}/C is a highly active and durable electrocatalyst toward ethanol oxidation in alkaline medium.

Moreover, the chronoamperometry were conducted at a constant potential of 0.3 V in 0.5 M ethanol electrolyte and 6.0 M ethanol electrolyte in figure 3.32(a) and (b), respectively. Lower current densities were appeared at lower potential due to the overpotential of ethanol oxidation, but the Rh_{28}-Sn_{72}/C also exhibited the best performance and maintained it longer.

These characteristics are attributed to the faster charge transfer kinetics [34]. In figure 3.33, the Tafel plots were taken in the mixture of 0.1 M potassium hydroxide and 6.0 M ethanol solution with a scan rate of 1 mV s^{-1} of Rh-Sn/C electrocatalysts and Pt/C catalyst. The Tafel slope of Pt/C remarkably increased as increasing ethanol concentration, whereas that of Rh-Sn/C showed obscure increments compared to the lower concentrated solution.

The effect of ethanol concentration can be explained by the competition between the coverage of ethoxy (*CH_3CO), resulting from the dehydrogenations of adsorbed ethanol on the surface of the catalysts, and hydroxyl groups (*OH). Because of its strong interaction with hydroxyl groups, Sn leads to higher hydroxyl coverage on the surface of Rh-Sn catalysts and lower surface concentration of ethanol than Rh. As ethanol concentration is increased, the CO intermediate coverage will increase, resulting in the increase of current density and facile charge transfer, that is,

the lower Tafel slopes.

In terms of Tafel plots, it can be concluded that the current is related exponentially to the overpotential. But the potential strongly affects the reaction kinetics, thus the rate constants is predictable using potential dependency using Butler-Volmer equation expressed as follow (O + ne = R) [45].

$$i = i_{cathodic} - i_{anodic} = n\ F\ A\ [k_f\ C_O(0,t) - k_b\ C_R(0,t)]$$

where $j = i / A$

$$j = n\ F\ [k_f\ C_O(0,t) - k_b\ C_R(0,t)]$$

where n means number of electron, F is faraday constant, A stands for surface area, k is rate constant, C indicates concentration. By keeping the potassium hydroxide concentration as a 0.1 M, the reaction constant is calculated by changing the concentration of ethanol.

Therefore, the current densities at a certain potential at 0.4 V were recorded in various ethanol concentration ranged from 0.02 M to 6.0 M, and plotted as log scale in figure 3.34. The slopes of Pt/C sample were not changed during varying the ethanol concentration. Rh/C also showed poor behavior along the concentration changes, however, the slopes were gradually improved as the rhodium ratios increased. This indicates the Sn-abundant electrocatalysts had

faster kinetics than Rh-abundant samples even at high concentration of ethanol. In addition to the improved slopes, the potential at maximum current density also positively shifted.

In figure 3.35, the current densities of Rh_{28}-Sn_{72}/C and Pt/C at three potentials with varied ethanol concentration were exhibited. As the potential increased, the slope of Pt/C became a negatively, while that of Rh_{28}-Sn_{72}/C maintained to positive values. Potential dependencies on this graph stated that the Rh_{28}-Sn_{72}/C electrocatalyst is a highly active material even at lower potentials and more concentrated solution, which attributed to the quick charge transfer rate relative to the other samples.

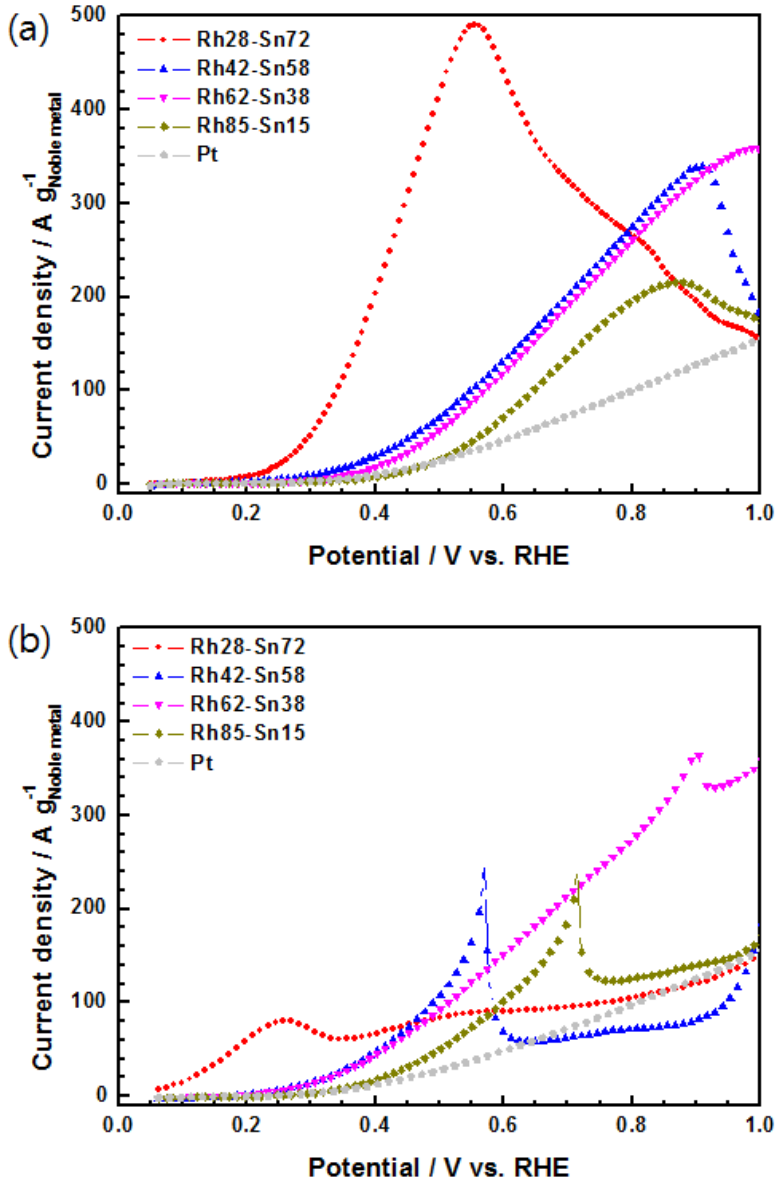

Figure 3.30. (a) Forward scans and (b) backward scans of polarization curves for Rh-Sn/C electrocatalysts in mixture of 0.1 M potassium hydroxide and 6.0 M ethanol solution under argon purging

Table 3.5 Summarized data of peak potentials, peak current densities at forward scan and backward scan and their ratios, and potentials at 0.01 A g^{-1}

	E at i(f,peak)	i (f,peak)	i (b,peak)	i(f) / i(b)	E @ 0.01 A g^{-1}_{NM}
Rh_{28}-Sn_{72}/C	0.56	490.83	80.13	6.125	0.213
Rh_{42}-Sn_{58}/C	0.91	339.74	248.01	1.370	0.306
Rh_{62}-Sn_{38}/C	0.99	358.94	372.09	0.965	0.358
Rh_{85}-Sn_{15}/C	0.88	216.58	243.59	0.889	0.421
Pt/C (J.M.)	1.00	154.85	154.85	1	0.404

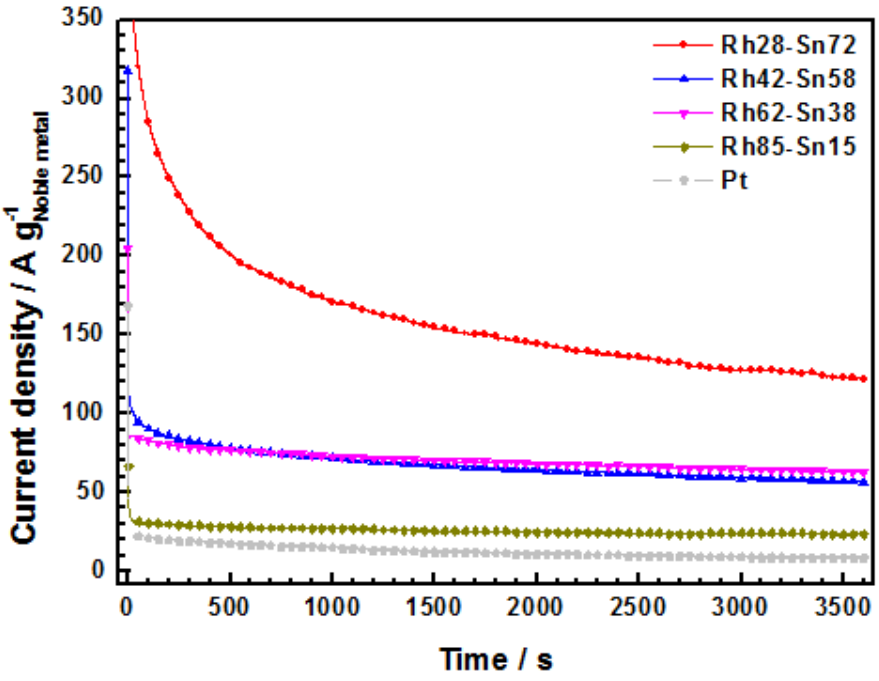

Figure 3.31. Chronoamperometry data at a constant potential of 0.5 V during 3600 seconds in mixture of 0.1 M potassium hydroxide and 6.0 M ethanol solution under argon purging

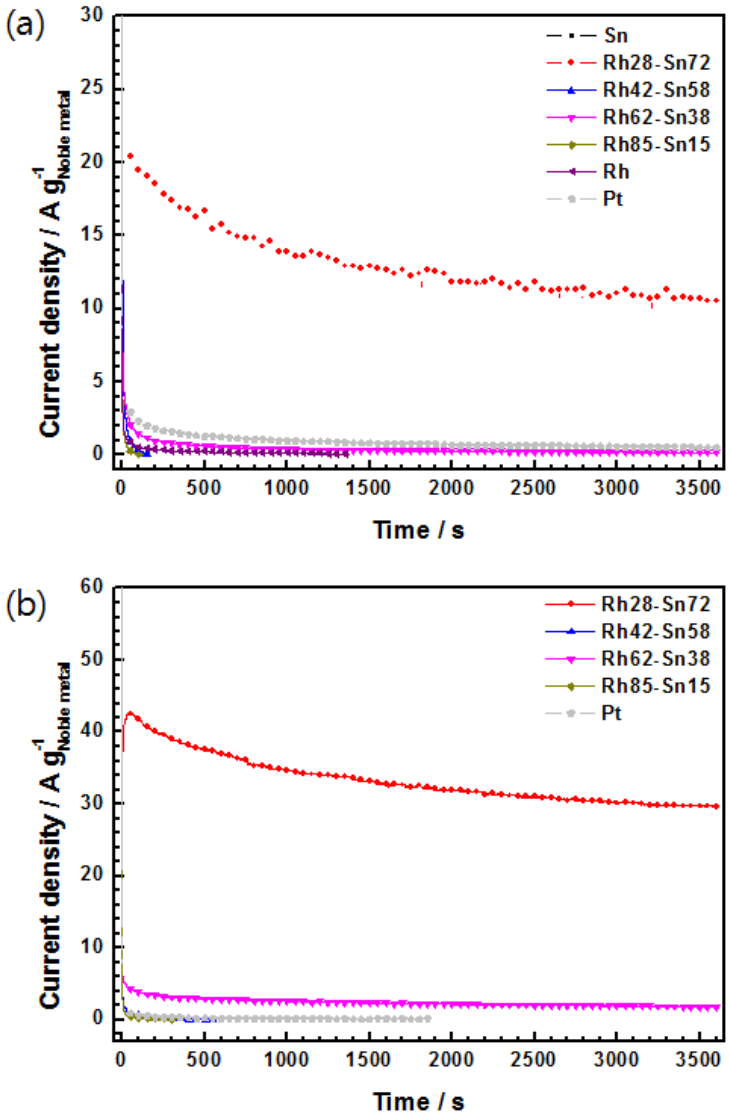

Figure 3.32. Chronoamperometry data at a constant potential of 0.3 V during 3600 seconds in mixture of 0.1 M potassium hydroxide containing (a) 0.5 M ethanol and (b) 6.0 M ethanol solution under argon purging

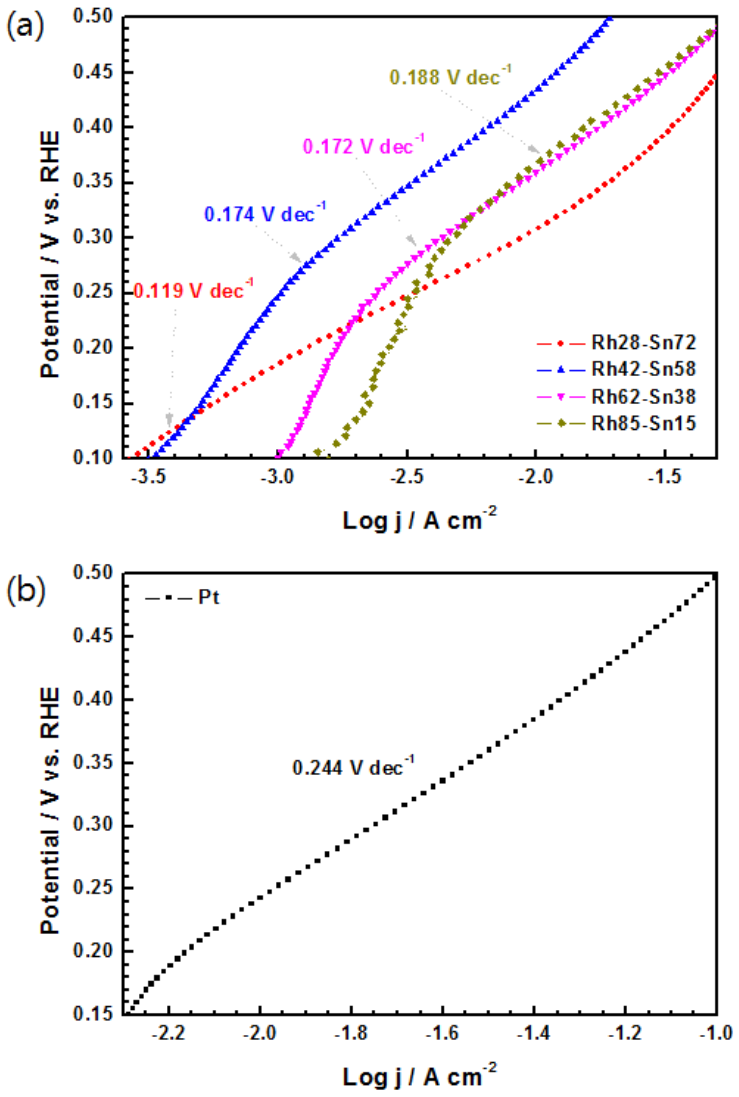

Figure 3.33. Tafel plots for ethanol oxidation on (a) Rh-Sn/C electrocatalysts and (b) commercial Pt/C in mixture of 0.1 M potassium hydroxide and 6.0 M ethanol solution under argon purging at a scan rate of 1 mV s^{-1}

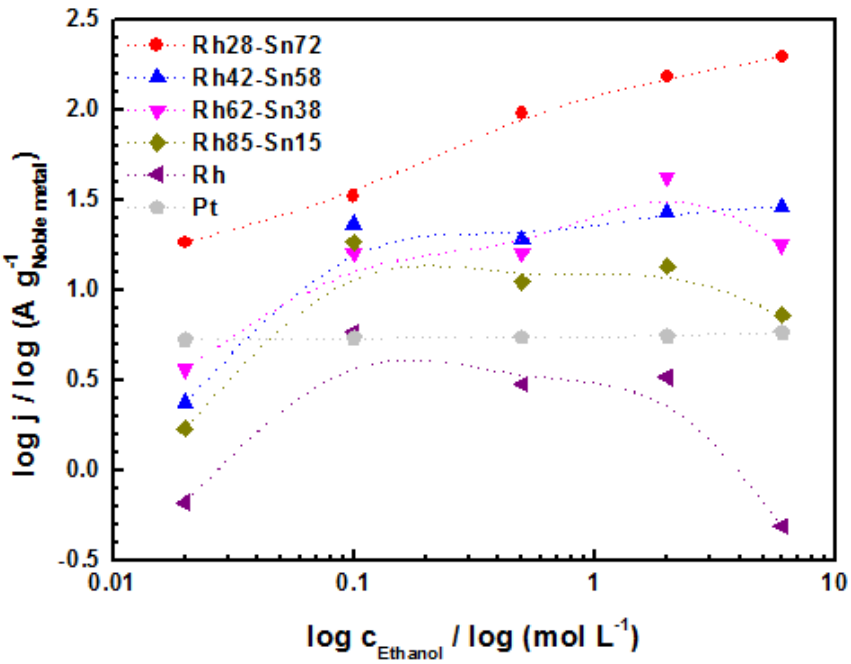

Figure 3.34. Relationship between various ethanol concentration and current densities at 0.4 V for the Rh-Sn/C and Pt/C electrocatalysts

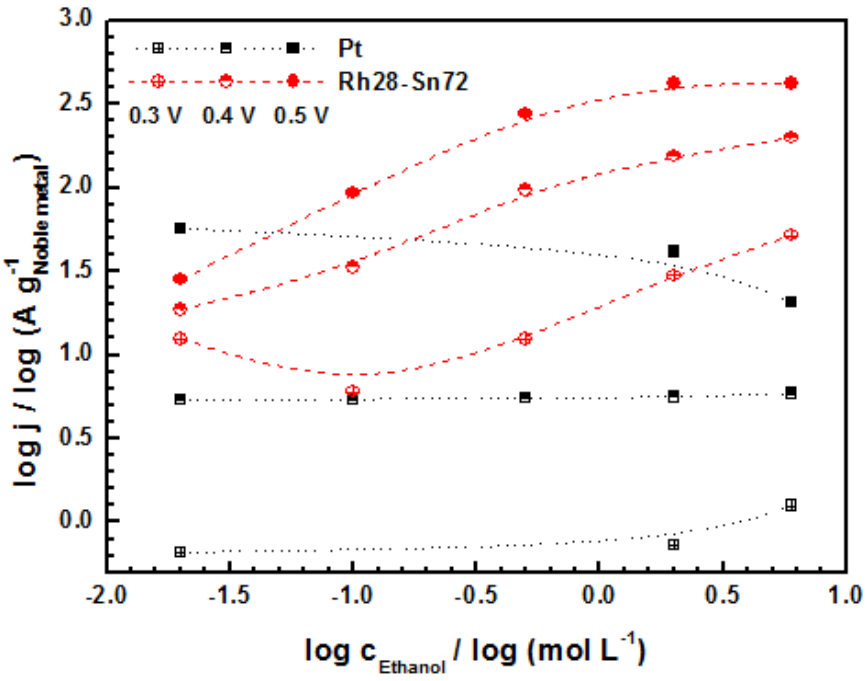

Figure 3.35. Relationship between various ethanol concentration and current densities at three potentials for the Rh_{28}-Sn_{72}/C and Pt/C electrocatalysts

3.3. References

[1] Naween Dahal, Stephany Garcia, Jiping Zhou, and Simon M. Humphrey, “Beneficial effects of microwave-assisted heating versus conventional heating in noble metal nanoparticle synthesis”, *ACS Nano*, **2012**, 6(11), 9433-9446.

[2] S. Baek, S.-H. Yu, S.-K. Park, A. Pucci, C. Marichy, D.-C. Lee, Y.-E. Sung, Y. Piao and N. Pinna, “A one-pot microwave-assisted non-aqueous sol–gel approach to metal oxide/graphene nanocomposites for Li-ion batteries”, *RSC Adv.*, **2011**, 1, 1687-1690.

[3] Stephen Brunauer, P. H. Emmett, and Edward Teller, “Adsorption of gases in multimolecular layers”, *J. Am. Chem. Soc.*, **1938**, 60 (2), 309–319.

[4] K.-S. Lee, I.-S. Park, Y.-H. Cho, D.-S. Jung, N. Jung, H.-Y. Park, and Y.-E. Sung, “Electrocatalytic activity and stability of Pt supported on Sb-doped SnO_2 nanoparticles for direct alcohol fuel cells”, *J. Catal.*, **2008**, 258, 143-152.

[5] R. Kou, Y. Shao, D. Mei, Z. Nie, D. Wang, C Wang, V. V. Viswanathan, S. Park, I. A. Aksay, Y. Lin, Y. Wang, and J. Liu, “Stabilization of electrocatalytic metal nanoparticles at metal - metal oxide - graphene triple junction points”, *J. Am. Chem. Soc.*, **2011**, 133, 2541-2547.

[6] Yung-Chiun Her, Jer-Yau Wu, Yan-Ru Lin and Song-Yeu Tsai, “Low-temperature growth and blue luminescence of SnO_2 nanoblades”, *Appl. Phys. Lett.*, **2006**, 89, 043115.

[7] J. C. M. Silva, R. F. B. De Souza, L. S. Parreira, E. T. Neto, M. L.

Calegaro and M. C. Santos, “Ethanol oxidation reactions using SnO_2@Pt/C as an electrocatalyst”, *Appl. Catal. B- Environ*., **2010**, 99, 265-271.

[8] V. D. Colle, J. Souza-Garcia, G. Tremiliosi-Filho, E. Herrero and J. M. Feliu, “Electrochemical and spectroscopic studies of ethanol oxidation on Pt stepped surfaces modified by tin adatoms”, *Phys. Chem. Chem. Phys.*, **2011**, 13, 12163-12172.

[9] A. Rabis, P. Rodriguez and T. J. Schmidt, “Electrocatalysis for polymer electrolyte fuel cells: Recent achievements and future challenges”, *ACS Catal*., **2012**, 2, 864-890.

[10] B. Braunchweig, D. Hibbitts, M. Neurock and A. Wieckowski, “Electrocatalysis: A direct alcohol fuel cell and surface science perspective”, *Catal. Today*, **2013**, 202, 197-209.

[11] A. Kowal, M. Li, M. Shao, K. Sasaki, M. B. Vukmirovic, J. Zhang, N. S. Marinkovic, P. Liu, A. I. Frenkel and R. R. Adzic, “Ternary Pt/Rh/SnO_2 electrocatalysts for oxidizing ethanol to CO_2”, *Nat. Mater*., **2009**, 8, 325-330.

[12] X. Zhang, H. Zhu, Z. Guo, Y. Wei and F. Wang, “Sulfated SnO_2 modified multi-walled carbon nanotubes – A mixed proton–electron conducting support for Pt catalysts in direct ethanol fuel cells”, *J. Power Sources*, **2011**, 196, 3048-3053.

[13] L. Jiang, G. Sun, S. Sun, J. Liu, S. Tang, H. Li, B. Zhou and Q. Xin, “Structure and chemical composition of supported Pt–Sn electrocatalysts for ethanol oxidation”, *Electrochim. Acta*, **2005**, 50, 5384-5389.

[14] R. B. Moghaddam and P. G. Pickup, “Support effects on the oxidation

of ethanol at Pt nanoparticles", *Electrochim. Acta*, **2012**, 65, 210-215.

[15] S. C. S. Lai, S. E. F. Kleyn, V. Rosca and M. T. M. Koper, "Mechanism of the dissociation and electrooxidation of ethanol and acetaldehyde on platinum as studied by SERS", *J. Phys. Chem. C*, **2008**, 112, 19080-19087.

[16] E. Higuchi, K. Miyata, T. Takase and H. Inoue, "Ethanol oxidation reaction activity of highly dispersed Pt/SnO_2 double nanoparticles on carbon black", *J. Power Sources*, **2011**, 196, 1730-1737.

[17] J. L. Margitfalvi, I. Borbáth, M. Hegedűs, Á. Szegedi, K. Lázár, S. Gőbölös and S. Kristyán, "Low temperature oxidation of CO over tin-modified Pt/SiO_2 catalysts", *Catal. Today*, **2002**, 73, 343-353.

[18] F. J. Scott, S. Mukerjee and D. E. Ramaker, "Contrast in Metal-Ligand Effects on Pt_nM Electrocatalysts with M equal Ru vs. Mo and Sn as Exhibited by in situ XANES and EXAFS Measurements in Methanol", *J. Phys. Chem. C*, **2009**, 114, 442-453.

[19] Fernando D. Vila, John J. Rehr, Shelly D. Kelly, and Simon R. Bare, "Operando effects on the structure and dynamics of $Pt_nSn_m/\gamma\text{-}Al_2O_3$ from Ab Initio molecular dynamics and X‑ray absorption spectra", *J. Phys. Chem. C*, **2013**, 117, 12446−12457.

[20] J. Singh, R.C. Nelson, B.C. Vicente, S.L. Scott, J.A. van Bokhoven, "Electronic structure of alumina-supported monometallic Pt and bimetallic PtSn catalysts under hydrogen and carbon monoxide environment", *Phys. Chem. Chem. Phys*., **2010**, 12, 5668-5677.

[21] R.F.B. De Souza, L.S. Parreira, D.C. Rascio, J.C.M. Silva, E. Teixeira-Neto, M.L. Calegaro, E.V. Spinace, A.O. Neto, M.C. Santos, “Study of ethanol electro-oxidation in acid environment on Pt_3Sn/C anode catalysts prepared by a modified polymeric precursor method under controlled synthesis conditions”, *J. Power Sources*, **2010**, 195, 1589–1593.

[22] M. Li, A. Kowal, K. Sasaki, N. Marinkovic, D. Su, E. Korach, P. Liu, and R.R. Adzic, “Ethanol oxidation on the ternary Pt–Rh–SnO_2/C electrocatalysts with varied Pt:Rh:Sn ratios”, *Eletrochim. Acta*, **2010**, 55, 4331−4338.

[23] J.C.M. Silva, L.S. Parreira, R.F.B. De Souza, M.L. Calegaro, E.V. Spinacé, A.O. Neto, and M.C. Santos, “PtSn/C alloyed and non-alloyed materials: Differences in the ethanol electro-oxidation reaction pathways”, *Appl. Catalysis B: Environmental*, **2011**, 110, 141− 147.

[24] M.P. Seah, and W.A. Dench, "Quantitative electron spectroscopy of surfaces: A standard data base for electron inelastic mean free paths in solids", *Surf. Interf. Anal.*, **1979**, 1(1), 2-11.

[25] B. Hammer, and J. K. Norskov, "Theoretical surface science and catalysis - Calculations and concepts", *Adv. Catal*. **2000**, 45, 71-129.

[26] M. V. GandugliaPirovano, V. Natoli, M. H. Cohen, J. Kudrnovsky, I. Turek, "Potential, core-level, and d band shifts at transition-metal surfaces", *Phys. Rev. B* **1996**, 54, 8892-8898.

[27] J. K. Norskov, K. W. Jacobsen, P. Stoltze, and L. B. Hansen, "Many-Atom Interactions in Metals", *Surf. Sci.* **1993**, 283, 277-282.

[28] Junliang Zhang, Miomir B. Vukmirovic, Kotaro Sasaki, Anand Udaykumar Nilekar, Manos Mavrikakis, and Radoslav R. Adzic, "Mixed-metal Pt monolayer electrocatalysts for enhanced oxygen reduction kinetics", *J. Am. Chem. Soc*., **2005**, 127, 12480-12481.

[29] E. Antolini and E.R. Gonzalez, “Effect of synthesis method and structural characteristics of Pt–Sn fuel cell catalysts on the electro-oxidation of CH_3OH and CH_3CH_2OH in acid medium”, *Catal. Today*, **2011**, 160, 28–38.

[30] Z. Liu, X. Y. Ling, X. Su and J. Y. Lee, “Carbon-supported Pt and PtRu nanoparticles as catalysts for a direct methanol fuel cell”, *J. Phys. Chem. B*, **2004**, 108, 8234-8240.

[31] M. Arenz, V. Stamenkovic, B. B. Blizanac, K. J. Mayrhofer, N. M. Markovic and P. N. Ross, “Carbon-supported Pt–Sn electrocatalysts for the anodic oxidation of H_2, CO, and H_2/CO mixtures.: Part II: The structure–activity relationship”, *J. Catal*., **2005**, 232, 402-410.

[32] A. Hamnett, “Mechanism and electrocatalysis in the direct methanol fuel cell”, *Catal. Today*, **1997**, 38(4), 445-457.

[33] F.H.B. Lima and E.R. Gonzalez, “Ethanol electro-oxidation on carbon-supported Pt–Ru, Pt–Rh and Pt–Ru–Rh nanoparticles”, *Electrochim. Acta*, **2008**, 53, 2963–2971.

[34] Wenxin Du, Kayla E. Mackenzie, Daniel F. Milano, N. Aaron Deskins, Dong Su, and Xiaowei Teng, “Palladium−tin alloyed catalysts for the ethanol oxidation reaction in an alkaline medium”, *ACS Catal*., **2012**, 2, 287−297.

[35] S.Y. Shen, T.S. Zhao, and J.B. Xu, “Carbon supported PtRh catalysts

for ethanol oxidation in alkaline direct ethanol fuel cell", *Int. J. Hydrogen energy*, **2010**, 35, 12911-12917.

[36] J.M. Orts, R. Gomez, J.M. Feliu, A. Aldaz, J. Clavilier, "Potentiostatic charge displacement by exchanging adsorbed species on Pt(111) electrodes - Acidic electrolytes with specific anion adsorption", *Electrochim. Acta*, **1994**, 39, 1519-1524.

[37] D.C. Koningsberger, B.L. Mojet, G.E. van Dorssen and D.E. Ramaker, "XAFS spectroscopy; fundamental principles and data analysis", *Top. Catal*., **2000**, 10, 143-155.

[38] Andrea E. Russell and Abigail Rose, "X-ray absorption spectroscopy of low temperature fuel cell catalysts", *Chem. Rev*., **2004**, 104, 4613-4635.

[39] F. Colmati, E. Antolini and E. R. Gonzalez, "Effect of thermal treatment on phase composition and ethanol oxidation activity of a carbon supported $Pt_{50}Sn_{50}$ alloy catalyst", *J. Solid State Electrochem*., **2008**, 12(5), 591–599.

[40] Wenxin Du, Qi Wang, David Saxner, N. Aaron Deskins, Dong Su, James E. Krzanowski, Anatoly I. Frenkel, and Xiaowei Teng, "Highly active iridium/iridium-tin/tin oxide heterogeneous nanoparticles as alternative electrocatalysts for the ethanol oxidation reaction", *J. Am. Chem. Soc*., **2011**, 133, 15172–15183.

[41] Wenxin Du, Qi Wang, Carlo A. LaScala, Lihua Zhang, Dong Su, Anatoly I. Frenkel, Virendra K. Mathura and Xiaowei Teng, "Ternary PtSnRh–SnO_2 nanoclusters: synthesis and electroactivity for ethanol oxidation

fuel cell reaction", *J. Mater. Chem.*, **2011**, 21, 8887–8892.

[42] Constantinos D. Zeinalipour-Yazdi, Andrew L. Cooksy, and Angelos M. Efstathiou, "CO adsorption on transition metal clusters: Trends from density functional theory", *Surf. Sci.*, **2008**, 602, 1858-1862.

[43] P. Lagarde, T. Murata, G. Vlaic, E. Freund, H. Dexpert, and J.P. Bournonville, "EXAFS studies of Pt-Al_2O_3 catalysts", *J. Catal.*, **1983**, 84, 333-343.

[44] Feng-Ju Lai, Loka Subramanyam Sarma, Hung-Lung Chou, Din-Goa Liu, Cheng-An Hsieh, Jyh-Fu Lee, and Bing-Joe Hwang, "Architecture of bimetallic Pt_xCo_{1-x} electrocatalysts for oxygen reduction reaction as investigated by x-ray absorption spectroscopy", *J. Phys. Chem. C*, **2009**, 113, 12674–12681.

[45] Allen J. Bard and Larry R. Faulkner, Electrochemical methods: Fundamentals and applications, John Wiley & Sons, Inc., 2001.

Chapter 4. Conclusions

This study purposes the synthesis of nano-sized electrocatalysts toward fuel oxidation with lower price and enhanced the activity with lower overpotentials than the existing catalysts. In addition, facile and rapid synthesis is introduced via microwave-assisted synthesis compared to the conventional methods, and total oxidation reaction of fuel can be further achieved to improve the efficiency. The electrochemical properties and morphological properties were evaluated carbon supported platinum and tin oxide nanoparticles in the first part, and the rhodium-tin alloyed nanoparticle deposited on carbon as an electrocatalyst for the fuel oxidation was prepared to further reach to fully oxidation reaction into the carbon dioxide.

The electrocatalyst of carbon supported platinum and tin oxide nanoparticle was prepared through the microwave-assisted synthesis. It is clearly confirmed that the platinum nanoparticles and tin dioxide nanoparticles were uniformly dispersed onto the surface of carbon supporting material. The electrocatalyst containing 16 wt% of tin oxide was exhibited both the highest activity for ethanol oxidation and chronoamperometry result at 0.5 V. The onset potentials of prepared electrocatalysts were negatively shifted compared to that of commercial catalyst, result from the adsorbed CO species on platinum are easily oxidized at lower potential by hydroxyl groups adsorbed onto the surface of nearby

tin oxide. In addition to the bifunctional effect, it is elucidated that the electronic effect also was also acted in the platinum-tin oxide nanocomposites from the investigations using x-ray absorption spectra. As the amounts of tin oxide increased, the white line of Pt L_3-edge decreased. According to the cyclic voltammetry results of changed shape along the amounts of tin oxide and theoretical calculations, the excess amounts of tin oxide nanoparticles dispersed on the carbon surface generates as an isolating barrier that hinders the electron transfer between platinum and carbon support, while too low amounts of tin oxide nanoparticles limits the adsorbed hydroxyl group transfer. The best electrocatalytic performance exhibited in the Pt-SnO_2(16)/C electrocatalyst that facilitates not only the hydroxyl functional group transfer from the oxide to platinum at lower potentials but also the electron transfer between carbon and platinum.

Without platinum as one of the most valuable metal, the rhodium-tin alloy nanoparticle as an electrocatalyst was formed onto the carbon. Alloyed nanoparticles with surface oxide were observed, and the tin oxide amounts were increased as increasing tin contents. Electrocatalytic activity and the ratios of peak current density at forward scan and backward scan were increased at higher tin contents in the sample. And rhodium-tin electrocatalysts produced much carbon dioxide compared to the conventional catalyst, result from the accomplishment of additional total oxidation of ethanol including C-C bond splitting. As the tin ratio was increased, the intensity at white line was increased that the interactions

between rhodium and adsorbed species become stronger than pure metal, which is corresponding with the electrochemical results. The overpotential and reaction rate were also improved even at lower operating potential and in concentrated ethanol solution calculated from Tafel plots and Butler-Volmer equations.

Consequently, the electrocatalysts with improved electrocatalytic activity and superior durability toward fuel oxidation were synthesized through the facile and swift method, and achieved further oxidation to carbon dioxide via total oxidation reaction of ethanol even in highly concentrated fuel solutions and at lower potentials.

국 문 초 록

연료전지는 전기화학적 산화 및 환원 반응에서 발생한 전자를 외부 회로를 통해 이용하는 형태로, 연료의 화학적인 에너지를 열에너지와 운동에너지로 변환 없이 직접 전기에너지로 변환시킨다는 점에서 고효율의 에너지 발생 장치라고 할 수 있다. 또한 생성된 오염 물질이 매우 적고, 소음에서 자유로우며, 기후, 날씨, 지역에 따른 제약이 없기 때문에 수송용, 휴대용, 발전용 등 다양하게 이용될 수 있다. 전해질 종류에 따라 분류되는 연료전지 중에서 연료의 수송, 보관 등이 용이하고, 독성과 점도 특성이 낮아 사람이 다루기 쉬우면서 높은 에너지 밀도를 가지는 에탄올을 연료로 하는 직접 에탄올 연료전지에 많은 관심이 집중되고 있다. 게다가 기존 화석 연료 자원이 고갈되는 상황에서 사탕수수, 옥수수 등의 섬유질 작물이나 식용 불가능한 나무 뿌리, 식물 등으로도 에탄올을 생산해 낼 수 있기 때문에 자원 유한성 문제 또한 적다는 특징이 있다. 하지만 직접 에탄올 연료전지 분야에서 개선되어야 하는 부분은 피독 현상에 의한 백금 촉매의 전기화학적 활성 유지 능력의 급속한 하락과 상대적으로 높은 가격, 그리고 산소 환원 반응보다도 높은 에탄올 산화 반응의 과전압으로 알려져 있다.

본 연구에서는 두 가지 형태의 연료 산화용 나노 입자 촉매를 합성하였으며, 그 목표는 백금 사용량을 낮추면서도 연료 산화 반응의 활성 유지 능력과 과전압을 동시에 개선할 수 있는 촉매를 디자인하고자 한다. 그리고 위 두 가지 요소에 더하여, 기존 방법보다 신속하고 간편하게 촉매를 합성 및 준비할 수

있는 합성법과 에탄올의 완전 산화 반응을 통하여 효율을 더 높일 수 있는 방법 또한 동시에 이루고자 하는 것에 있다. 첫 부분에서는 백금 나노 입자와 주석 산화물 나노 입자가 탄소 입자에 고르게 담지된 형태를 제조하여 촉매의 전기화학적 성질과 구조적 성질을 평가하였다. 두 번째 부분에서는 가장 널리 사용되는 백금 촉매 대신 로듐을 사용하여 연료의 완전 산화 반응의 유도를 목표로 하였다. 탄소에 담지된 로듐-주석 합금 나노 입자를 합성하여 물리 화학적인 성질을 파악하고 산화 반응에서의 전기 촉매의 활성도와 내구력을 평가하였다.

일반적으로 수 시간에서 수 일에 걸쳐 합성되는 기존 방법에서 탈피하여, 불과 수 분 내로 합성 가능한 마이크로파를 이용한 합성법으로 촉매를 제조하였다. 표면 활성제가 첨가되지 않는 용액에서의 마이크로파 합성법과 기존 합성법을 통해 탄소에 담지된 백금 나노 입자 촉매를 각각 제조하였다. 기존 합성 방법과 비슷한 입자 크기를 보이는 것을 확인할 수 있었으며, 입자 크기 표준 편차는 절반 수준으로 낮아진 것으로 확인되었다. 이는 마이크로파 합성법이 매우 짧은 시간 내에 전구체가 핵 형성을 이루는데 충분한 에너지를 공급하여, 용액 내에서 고르게 형성된 핵을 중심으로 성장이 일어난 것으로 생각될 수 있다.

백금과 주석 산화물 나노 입자들이 각각 탄소 표면에 고르게 담지되어 있는 것을 투과 전자 현미경과 엑스레이 회절 분석으로 확인하였고, 엑스레이 광전자 방출 분석법을 통해 백금은 금속 상태로 존재하고 주석은 산화수가 4인 산화물 형태로 존재함을 알 수 있었다. 전체 무게 대비 16 %의 주석 산화물이 담지되었을 때 가장 우수한 산화 반응 능력을 보여주었고, 일정 전압에서 장시간 운전되는 경우에도 같은 경향을 보여주었다. 또한 연료

산화 반응이 시작되는 시점이 백금만 존재하는 촉매의 경우보다 빠르게 시작되는 것으로 미루어 보아, 백금 표면에 흡착된 탄소종들이 주석 산화물 표면에 흡착된 수산화기들에 의해 빠르게 산화되면서 성능 또한 증가되는 것으로 이해할 수 있었다. 엑스레이 흡수 스펙트럼 측정을 통해 주석 산화물 입자의 양이 증가할수록 백금의 d 궤도 전자 준위가 낮아져 흡착물과의 결합력이 감소하는 것을 확인하였다. 순환 전압법을 통해 그래프 모양이 변화하는 시점과 이론적 계산 값들의 연관성을 통해 주석 산화물 나노 입자가 탄소 표면을 모두 덮을 정도로 다량 존재하는 경우에는 전기 전도도가 상대적으로 낮은 주석 산화물의 층이 백금과 탄소 사이의 전기적 연결을 방해하여 성능에 불리한 작용을 하고, 너무 적은 양이 존재하는 경우에는 백금 표면에 강하게 흡착된 탄소종이 수산화기에 의해 산화되지 못하면서 활성 표면적이 감소하게 되는 결과를 초래하는 것으로 설명할 수 있다. 따라서 위 형태와 같은 촉매에서는 백금과 주석 산화물의 분자 비율이 비슷한 경우에 탄소종과의 흡착 세기를 감소시키면서, 탄소종과 수산화기들의 반응을 최대한 이끌어낼 수 있는 것으로 확인되었다.

마이크로파를 이용해 로듐과 주석을 동시에 합성한 합금 금속 나노 입자를 탄소에 담지시켜 연료 산화 반응에 대한 활성을 평가하였다. 투과 전자 현미경과 엑스레이 회절 분석을 통해 로듐과 주석이 약간의 표면 산화물과 함께 합금 형태로 존재함을 확인하였고, 주석의 함량이 증가할수록 주석 산화물의 양이 증가하는 것을 엑스레이 광전자 방출 분석으로 확인하였다. 로듐의 함량이 감소할수록 연료 산화 활성도가 증가하였고, 또한 정방향과 역방향의 최대 전류 밀도 비율을 보여주어 탄소종

흡착에 의한 성능 감소가 최소화되는 것을 알 수 있었다. 적외선 분광계를 통해 인가 전압에 따른 이산화탄소의 발생량을 분석한 결과, 더 낮은 전압에서도 기존 촉매보다 많은 양의 이산화탄소가 발생하고 전압이 높아질수록 더욱 많은 양이 측정됨으로 보아, 합성된 촉매가 에탄올의 탄소-탄소 분자를 깨뜨리면서 완전 산화 반응으로 추가 진행함을 나타내었다. 촉매 내의 주석 비율이 증가함에 따라, 로듐과 흡착종 사이의 결합력이 증가하는 것을 엑스레이 흡수 스펙트럼을 통해 확인되어 활성 결과를 뒷받침하는 것으로 알 수 있었다. 또한 로듐-주석 합금 촉매가 고농도의 연료와 저전압 영역대에서 더욱 우수한 활성이 나타나고, 활성의 내구력 또한 장기간 유지됨을 확인하였다. 타펠 플롯을 통해 특정 전압에서의 과전압이 기존 촉매보다 로듐-주석 합금 촉매들에서 우수함을 확인하였고, 연료 농도가 더욱 농축된 상황에서도 악화되지 않는 경향을 보여주었다. 다양한 농도의 연료를 사용하여 연료 산화 반응의 반응 속도를 관찰한 결과, 고농도 연료 및 저전압 영역에서도 모두 높은 반응 속도를 유지하는 것으로 보아 우수한 활성과 안정된 활성 내구력을 나타내는 것을 확인하였다.

본 연구를 통해 신속하고 간편한 합성법을 통하여 연료 산화 반응에 대한 향상된 활성을 가지면서 경제성이 개선된 형태의 촉매를 소개하였고, 또한 완전 산화 반응으로 추가 진행되고 고농도 연료 및 저전압 작동이 가능한 촉매를 디자인하였다.

주요어: 연료전지, 전기화학 촉매, 연료 산화 반응, 복합 기능 효과, 전자 효과

학 번: 2010-31326

감사의 글

학부 과정을 마치고 대학원 진학을 결심하게 된 결정적인 동기는 깊이 있는 학문적 실력을 기반으로 하여 그 분야의 발전에 기여하고 싶다는 작은 소망이 있었기 때문이었습니다. 대학원에서의 짧지 않은 기간 동안 학문의 끝없는 심오함을 실감하며 절망과 좌절을 맛보기도 했지만 주위에 항상 도움의 손길을 내밀어준 분들이 있었기에 학위 과정을 무사히 마칠 수 있게 되었습니다. 아직도 많이 부족한 저에게 무한한 배려와 아낌 없는 도움을 주신 그 분들께 감사의 글을 드리려 합니다.

항상 폭넓은 시야와 함께 도전적으로 임할 수 있도록 격려해 주시고, 변함없는 믿음으로 지켜봐 주신 성영은 교수님께 진심 어린 존경의 마음을 담아 감사 드립니다. 그리고 논리적이고 열정적인 연구자로 성장할 수 있도록 조언해 주신 오승모 교수님, 탁용석 교수님, 김민수 교수님, 유성종 박사님께도 진심으로 감사 드립니다. 교수님들께서 조언해 주신 내용들을 항상 되새기며 앞으로 더욱 발전하는 모습을 보여드리겠습니다.

연구를 진행하면서 많은 난관에 봉착할 때마다 큰 힘이 되어준 광 전기화학 에너지 연구실의 선배님들, 동기들, 후배님들에게 가슴 깊이 고마움을 느낍니다. 좁은 연구실에서 매일 함께 했던 여러분들이 있었기에 신뢰하며 의지할 수 있었고 그 과정에서 모두가 소중하고 고귀한 존재라는 사실을 새삼 느낄 수 있었습니다. 학문적으로 그리고 인격적으로 성숙할 수 있는 시간을 같이 만들어 준 여러분과의 인연이 앞으로도 진하게 지속되도록 노력하겠습니다.

오랜 시간 동안 함께 하며 서로에게 동기 부여가 될 수 있는 존재가 되어 주는 광문 친구들에게도 고맙다는 말을 전합니다. 항상 먼저 챙겨주고 따뜻하게 맞아주며 가족과 같은 유대감을 느끼게 해주는 동문회 선배님들과 후배님들에게도 늘 감사함을 느끼고 있습니다. 그리고 서로 너무나 다른 환경에서도 신기할 만큼 마음이 잘 통하는 유니트 친구들에게도 고마움을 전합니다.

언제나 긍정적인 마음과 따스한 배려로 기운을 북돋아 주시며 헌신적으로 지원해 주시는 아버지와 어머니께 진심으로 가슴 깊이 감사 드립니다. 그 동안 노심초사하며 보내셨던 시간을 뒤로 하고 항상 행복하고 즐거운 시간만 가득하시도록 노력하겠습니다. 앞으로도 자만하지 말고 꾸준히 정진하여 모범이 될 수 있는 사람이 될 것을 할아버지, 할머니께도 맹세하며 감사함 또한 전합니다. 함께 하는 즐거움을 유년 시절부터 깨닫게 해준 사촌들에게도 고마움을 표합니다. 그리고 학위 기간 동안 모든 희로애락을 함께 했던 인영이에게 무척 고맙고 감사합니다.

매 순간을 감사하는 마음으로 자만과 오만을 경계하고 항상 열정적으로 노력하며 소중한 인연을 지켜나가는 사람이 되도록 하겠습니다. 모든 분들에게 행복과 안녕이 함께하길 기원합니다. 진심으로 감사 드립니다.

2014년 1월

안 민 제 드림